8-1-2022

Using Quantum Fluctuations to Regularize an Analytic Continuation Problem from Many-Body Physics

Lucretius Coleman

USING QUANTUM FLUCTUATIONS TO REGULARIZE AN ANALYTIC CONTINUATION PROBLEM FROM MANY-BODY PHYSICS

A Dissertation

presented in partial fulfillment of requirements

for the degree of Doctor of Philosophy

in the Department of Physics and Astronomy

The University of Mississippi

by

LUCRETIUS COLEMAN

August 2022

ABSTRACT

Extracting spectral information via inversion from Quantum Monte Carlo sampled data is a difficult task. There is a need to analytically continue noisy and often incomplete imaginary-time data into the full complex domain. A new approach is proposed that uses the quantum fluctuations of spin momenta to regularize the inversion. A one-dimensional Heisenberg chain in the presence of a transverse field is first encoded with synthetic data representing several classes of spectral functions and then run through a Density Matrix Renormalization Group algorithm to find its ground state. This solution corresponds to a probable, high quality solution to the inversion. Using optimization constraints and sampling techniques, forward model spectra are replicated by inversion that capture distinguishing characteristics that are often washed out in methods that favor smoothed out solutions.

DEDICATION

For my wife, Rachel, who has been ever-patient through the years during my academic pursuits.

For my mother, Mae, who has believed in me every day of my life.

For my children, Sariyah, Alex, and Amari, each one an inspiration for me to be a better version of myself every day.

ACKNOWLEDGEMENTS

A very gracious thank you is owed to Dr. Kevin Beach for his generosity of knowledge, advice, and patience for the duration of this work.

Thank you to Dr. Lucien Cremaldi, a long-time advisor and friend who's encouragement during my undergraduate days helped spur my academics accomplishments today.

Thank you to Dr. Rick Gordon and Dr. Jake Bennett for honoring me by being a part of my committee.

Thank you to the University of Mississippi Physics Department for providing not only financial, but intangible, support the duration of my studies and research.

Thank you to Mr. Thomas Jamerson for his guidance and support as not only a laboratory physicist, but as a friend.

Thank you to Dr. Don Summers, who sage advice will be forever missed.

Contents

List of Figures

List of Tables

1 MOTIVATION

A well-established field of condensed matter physics is the study of quantum many-body systems. Exact analytical solutions are extremely difficult in systems of more than a few strongly interacting particles, leaving the bulk of analysis to numerical methods and brute force approximations. Of the interesting quantities one might want to measure, time-shifted correlation functions, which probe dynamical processes such as transport, are some the most challenging to tackle.

Of the approximation methods available to the quantum many body physicist, we focus on Quantum Monte Carlo (QMC) simulations, which are carried out using stochastic sampling. While QMC methods produce asymptotically exact results for correlation functions, the data produced is in the domain of imaginary time, τ. Recovery of the real-time properties requires a Wick rotation $\tau \rightarrow it$. The final product we are interested in is generally the spectral function appearing in the Lehman representation of the real-time function's Fourier transform. This is the object that contains many of the key physical properties of the system as a whole.

Accordingly, having a reliable method by which to extract real-valued data from imaginary-time output is important. Unfortunately, this process is known to be an ill-posed inversion, and it is highly unstable with regard to an incomplete and noisy data set.

The relationship between the imaginary time correlation function $G(\tau)$ and its real-valued spectral representation $A(\omega)$ takes the form of the Fredholm equation,

$$G(\tau) = \int d\omega \, K(\tau, \omega) A(\omega). \tag{1.1}$$

This linear integral equation can be discretized and inverted in the obvious way ($A = K^{-1}G$), but the results are generally unsatisfactory; in particular, we note the breakdown of the positivity condition ($A \geq 0$).

Many tools have been developed to effect the transformation from the imaginary- to real-time

domain. In one form or another, each one of these tools require a means to regularize the unstable inversion. Most are ad hoc and work situationally with varying degrees of effectiveness, and the quality of their extracted spectral functions is difficult to assess [31, 47]. Methods used to improve the spectral extraction include various forms of least squares fitting to functions, analytic summation over Matsubara frequencies, and Padé approximants [29]. Several algorithms that involve averaging over all spectra consistent with the given data have also been developed [60]. The most popular approach, however, is the Maximum Entropy Method (MEM), a Baysian statistics-based method which finds the single most probable solution amongst a continuous family of solutions [31].

Each method has its drawbacks. The methods that regularize the inversion most aggressively tend to produce overly smoothed results, in which sharp features in the spectral transform are obscured. Since we are often looking for sharp peaks or gap edges, it's important to maximize our ability to distinguish such features and not to smear them out. Other approaches are slow to achieve convergence or are overly sensitive to the accuracy of input data.

The stochastic analytic method, introduced by Sandvik and refined by Beach, formalizes a promising averaging approach, deriving a connection to the rigorous statistical considerations of the MEM [5, 55]. The result is a technique that solves the analytic continuation problem by means of a classical, constant-temperature thermodynamic ensemble whose mean field limits reduce to that of the MEM, with some dependence on the details of the sampling [5].

This methodological branch has shown results that rival that of the MEM, with the progression of techniques to resolve spectral features through the optimization of adjustable constraints [26].

My area of research takes inspiration from this approach but applies *quantum* rather than thermal fluctuations. The idea is to map the analytic continuation solution to a 1D Heisenberg spin chain with long-range interactions and solve for its spin profile in the ground state. This approach takes advantage of the fact that the ground state can be determined efficiently within the framework of Matrix Product States (MPS) by way of the Density Matrix Renormalization Group (DMRG) algorithm. A mapping then connects the measured spin profile to the desired spectrum.

2 QUANTUM MANY-BODY SYSTEM

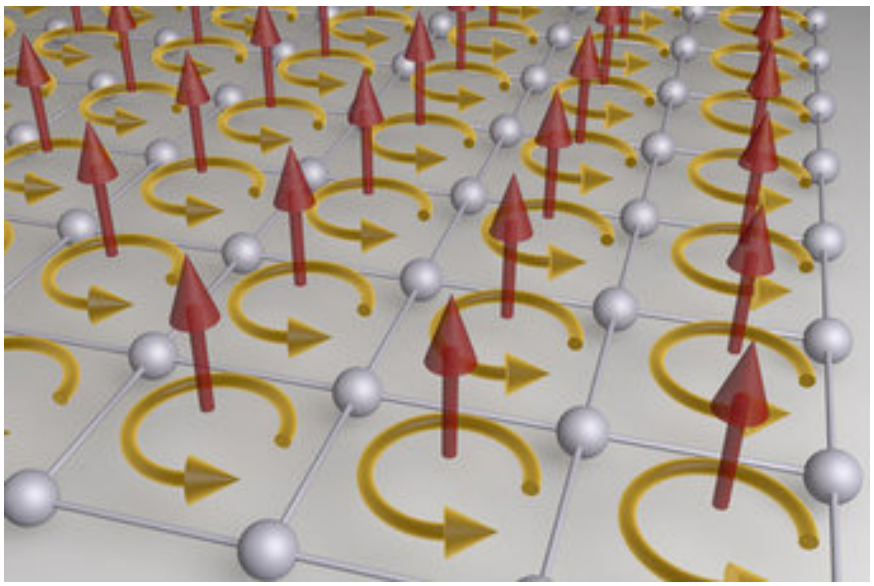

Figure 1: Quantum many-body system.

The goal of this branch of physics is to investigate the properties of a system of many interacting particles. This can be by means of thermodynamic, quantum, spectroscopic, or numerical functional means, expanding the breadth of knowledge of microscopic physics which, in principle, govern all materials small and large.

These systems can be described by the many-body wave equation

$$\Psi(x_1, x_2, ...x_N, t), \tag{2.1}$$

which is a solution of the well-known Schrodinger equation [1]

$$\left[-\frac{\hbar^2}{2m}\sum_j^N \nabla_j^2 + \sum_{i<j} V(x_i - x_j) + \sum_j U(x_j)\right]\Psi = i\hbar\frac{\partial\Psi}{\partial t}, \tag{2.2}$$

with V being the potential, m the individual particle mass, x_i the location in a lattice, and $\hbar$ Planck's constant with the value $1.05457 \times 10^{-34}\,\mathrm{m}^2\,\mathrm{kg/s}$.

Qubit system dimensionality

n	$d = 2^n$
1	2
2	4
3	8
4	16
⋮	⋮
10	1024

Table 1: Qubit dimensionality of a qubit system with n degrees of freedom.

Any pertinent information about the system is expected to be present within its wavefunction, only a step away from being obtained by solving the Schrodinger equation. However, the complexity of the problem due to its dimensionality rapidly makes this an intractable problem in even the simplest of cases.

Take the case of a two-state system of objects. In its classical form, the dimensional scaling of such a system would obey the direct sum rule, where if d_1 is the dimension of the space representing 1, d_2 that of system 2, and so on, the total dimensionality of the whole system is

$$d_1 \bigoplus d_2 \bigoplus \cdots \bigoplus d_n. \tag{2.3}$$

On the other hand, for a quantum system such as one with levels defined by a simple spin up (↑) and a spin down (↓), the dimensionality of the composite system obeys the product rule

$$d_1 \bigotimes d_2 \bigotimes \cdots \bigotimes d_n. \tag{2.4}$$

The system as a whole is a superposition of the individual n systems. The Hilbert space that spans the system has a total dimensionality $D = d^n$, where d is the dimension of individual system. So for the two state quantum case, the Hilbert space $D = 2^n$.

In the case of what would be considered a reasonably small n of 10, the dimensionality of such a Hilbert space is 1024.

The exponentially scaled complexity of many body problems is readily apparent even in such a simple example. Approaching dimensionally more complicated Schrodinger equations

by exact means is nearly impossible. There are simply too many variables and even the most powerful computers have only so much processing power.

For many-body systems, the number of particles is not simply in the thousands, but approaches scales of 10^{23}. Similarly, time (s) and length (m) scales are in the 10^{15} and 10^{-8}, respectively. The gulf between classical and quantum is a chasm measurable not only through instrumentation, but by sheer computational complexity.

It's obvious that additional approaches are necessary through bold approximations and other numerical means. Much of computational condensed matter study is dedicated to the development and refinement of such algorithms, ranging from the various flavors of Quantum Monte Carlo (QMC) sampling to that of Density Matrix Renomalization Group (DMRG) approximation.

3 QUANTUM FIELDS

From the need for the development of a language necessary to approach the complex many-body problem lies the concept of the quantum field operator.

A quantum field is the quantum analogue to the classical field ϕ, but instead of being an operator that distinctly describes matter, we can picture a quantum field to be a generalization of matter itself at different frequencies, ie at certain special eigenstates they add or subtract particles in a system [23]. As such, quantum fields can be thought of as undergoing continuous quantum fluctuations. Quantum fluctuations consist of quantized packets of $E = \hbar\omega$, a result of the uncertainty principle

$$\Delta E \Delta t \geq \frac{\hbar}{2}, \tag{3.1}$$

which expresses the uncertainty of the energy and time of a particle.

Quantum fluctuations are random changes in the energy of a point in space. They're energetic bursts in space-time responsible for such effects such as the Casimir effect and phase transitions in exotic quantum material [22].

The concept of the quantum field is related to that of the second quantization representation of a quantum system. While first quantization allows for the transition from the classical world to the quantum by means of replacing the classical momentum and position operators

$$E \rightarrow i\hbar \frac{\partial}{\partial t}, \tag{3.2}$$

$$p \rightarrow -i\hbar \frac{\partial}{\partial x}, \tag{3.3}$$

and the Poisson brackets which relate canonical conjugate values with the commutator

$$[x, p] = i\hbar, \tag{3.4}$$

of which non-commutative relations lead to uncertainty.

Second quantization extends this to the realm of many body systems with large numbers of degrees of freedom. It does so by representing the wavefunction as a field operator itself.

An example is the classical string, described by a displacement field ρ and a transverse momentum field π. Its classical Hamiltonian is

$$H = \int dx \left[\frac{T}{2}(\nabla\phi(x))^2 + \frac{1}{2\rho}(\pi(x))^2\right], \tag{3.5}$$

where T is the tension of the string and ρ the mass density. Imposing the canonical commutative relation

$$[\rho(x), \pi(y)] = i\hbar\delta(x - y) \tag{3.6}$$

defines the degrees of freedom of the system continuously through space.

For bosons and fermions, respectively, second quantization describes quantum fields through non-zero commutation relation between particle fields and their complex conjugates.

$$\text{fermions: } \{\psi(x), \psi^\dagger(y)\} = \delta(x - y), \tag{3.7}$$

$$\text{bosons: } [\psi(x), \psi^\dagger(y)] = \delta(x - y). \tag{3.8}$$

Consequently, bosonic physics derive from the algebra of commutation operations, and fermionic physics from that of anti-commutation operations. This wavefunction-to-operator transformation can further be extended to describe the creation and destruction of particles in a many body system.

Consider a state devoid of particles, in a state $|0\rangle$ deemed vacuum. An annihilation operation by an annihilator $\psi(x)$ would yield nothing:

$$\psi|0\rangle = |0\rangle. \tag{3.9}$$

However, the creation operator $\psi^\dagger(x)$ increments the number of particles by one,

$$\psi^\dagger(x_1)|0\rangle = |x_1\rangle. \tag{3.10}$$

Extending this to a N-particle system leads to the simplified representation

$$|x_1 x_2 ....x_N\rangle = \psi^\dagger(x_N)...\psi^\dagger(x_2)\psi^\dagger(x_1)|0\rangle, \tag{3.11}$$

where x^i denotes the site index for the i^{th} particle, a simple trick of bookkeeping. Similarly, its conjugate takes the form

$$\langle x_N ....x_2 x_1| = \langle 0|\psi(x_1)\psi(x_2)...\psi(x_N). \tag{3.12}$$

The wavefunction $|\psi_N\rangle$ of a N-particle system is then $\langle x_N ....x_2 x_1|N\rangle$ which simplifies to

$$\psi(x_1 x_2 ...x_N) = \langle 0|\psi(x_1)\psi(x_2)...\psi(x_N)|N\rangle. \tag{3.13}$$

Therefore, the operators $\psi(x_i)$ represent matrix elements which contain all of the information of the quantum field, preserving exchange symmetry and total N.

4 CORRELATION FUNCTION

The two-point correlation function, often referred to as a propagator, is the expectation value of the time-ordered product of two field operators,

$$G(t) = -\langle T[\hat{O}(t)\hat{O}^{\dagger}(0)]_{\mp}\rangle. \tag{4.1}$$

These operators are made up of wave functions in the second quantization representation, as described in the previous chapter. In the interaction picture, their time dependence is given by

$$\hat{O}_I(t) = e^{iH_0 t}\hat{O}e^{-iH_0 t}, \tag{4.2}$$

where H_0 is the non-perturbation portion of the Hamiltonian,

$$H = H_0 + H_I, \tag{4.3}$$

and H_I is the portion of the Hamiltonian from particle interactions [6]. The time ordering is described formally by Dyson's formula, i.e., the operators are arranged sequentially from right to left.

Numerically, the correlation function represents expectation values of a time ordered product of a string of fields. These expectation values are coefficients of the Taylor expansion of the vacuum-to-vacuum transition amplitude in the presence of an external field [61].

By Wick rotation, which involves the substitution $t \rightarrow -i\tau$, one obtains the imaginary-time correlation function, which is the central quantity of interest in this dissertation. In general, Quantum Monte Carlo simulations provide accurate estimates of G for a finite set of imaginary time points $\tau_1, \tau_2, \ldots, \tau_m$.

The imaginary time correlator $G(\tau)$ satisfies the (anti-)periodicity relation $\mp G(\tau+\beta)$, where the upper sign holds for fermionic systems and the lower for bosonic. Since $G(\tau)$ is completely

defined in the time interval β, an equivalent representation of the correlation function is given by the Fourier transform

$$G(\tau) = \frac{1}{\beta} \sum_{\omega_n} e^{-i\omega_n \tau} G(\omega_n), \tag{4.4}$$

$$G(\omega_n) = \int_0^\beta d\tau \, e^{i\omega_n \tau} G(\tau), \tag{4.5}$$

at Matsubara frequencies

$$\omega_n = \frac{(2n+1)\pi}{\beta} \tag{4.6}$$

for fermion operators and

$$\omega_n = \frac{2n\pi}{\beta} \tag{4.7}$$

for bosonic operators.

Assuming $G(\omega_n)$ is well-behaved—which is to say that $\langle \hat{O}\hat{O}^\dagger \pm \hat{O}^\dagger \hat{O} \rangle < \infty$ is bounded–the Fourier components can be written in the functional form

$$\mathsf{G}(z) = \int_{-\infty}^{\infty} \frac{d\omega}{2\pi} \frac{\rho(\omega)}{z - \omega}, \tag{4.8}$$

where the function $\rho(\omega)$ is positive definite and real. $\mathsf{G}(z)$ is analytic everywhere in the complex plane, with the possible exception being along the real axis; the definition is chosen to establish the correspondence $\mathsf{G}(i\omega_n) = G(\omega_n)$. The formal evaluation of the expression amounts to an imaginary path integral in the presence of branch cut discontinuities at $z = \omega$, corresponding to a jump in $\mathsf{G}(z)$ and a non-zero value of $\rho(\omega)$; specifically,

$$\mathsf{G}(\omega + i0^+) - \mathsf{G}(\omega + i0^-) = \pm\rho(\omega). \tag{4.9}$$

If there exists a countably infinite number of points along the imaginary axis, $\mathsf{G}(z)$ can be uniquely extended to the entire complex plane by the principle of analytic continuation [5]. Identifying $G(\omega_n) = \mathsf{G}i\omega_n)$, the Matsubara-defined propagator becomes

$$G(\omega_n) = \mp \int \frac{d\omega}{2\pi} \frac{\rho(\omega)}{i\omega_n - \omega}. \tag{4.10}$$

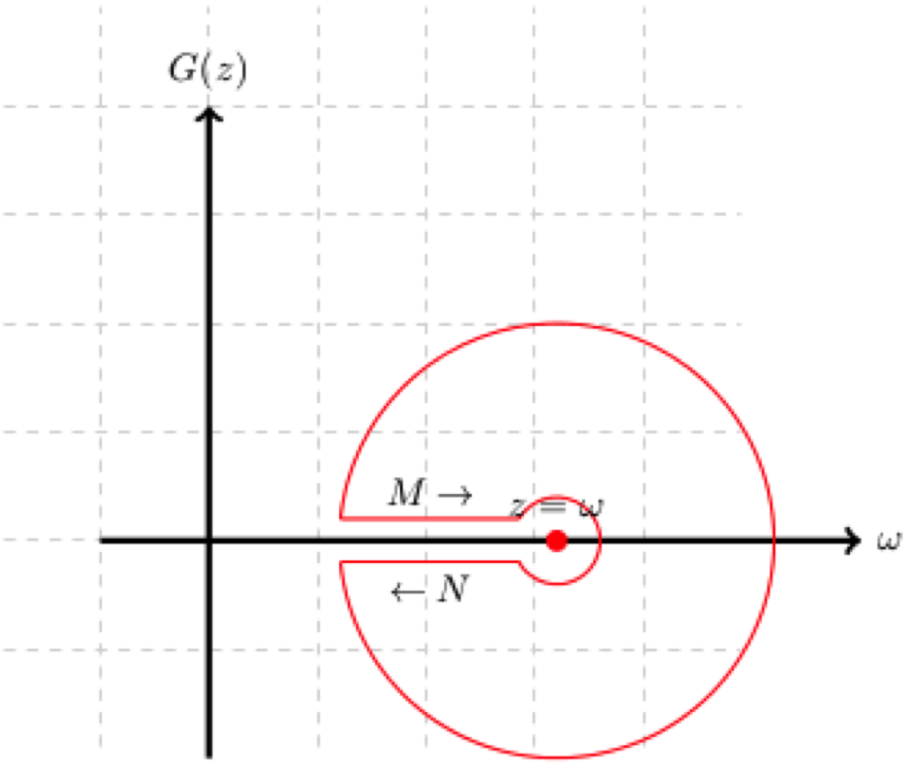

Figure 2: Branch-cut discontinuity at $z = \omega$, resulting in a jump in $\mathsf{G}(z)$ over the real axis. $\mathsf{G}(z)$ is analytic everywhere except at similar real-valued points.

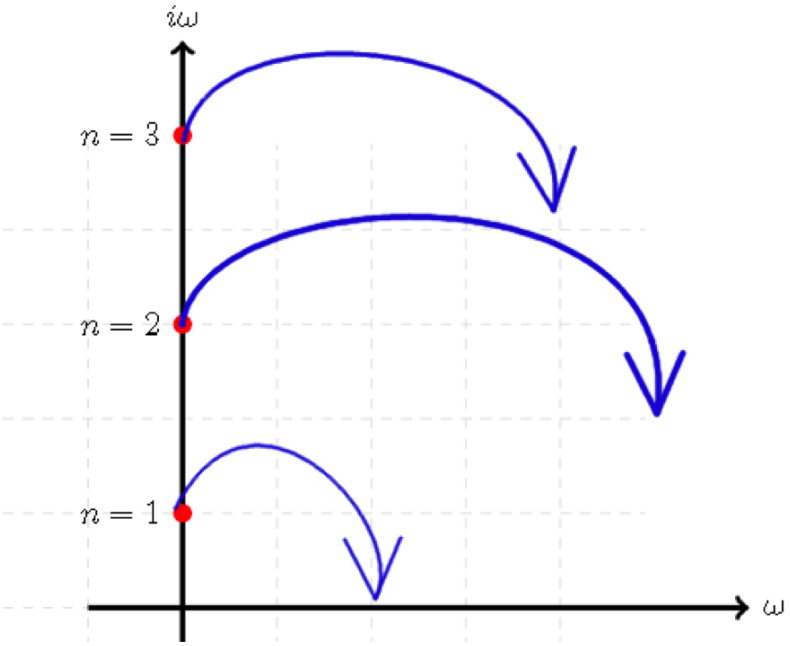

Figure 3: Analytic continuation onto the complex plane for n_i points coinciding with Matsubara frequencies. As i approaches a countably infinite number, it's possible to extend $G(i\omega)$ to all points in the real plane.

Fourier transforming back to the imaginary time representation and summing over the Matsubara frequencies yields [55]

$$\begin{aligned} G(\tau) &= \mp \int \frac{d\omega}{2\pi} \frac{e^{-\omega\tau}\rho(\omega)}{e^{-\beta\omega} \pm 1} \\ &= \int d\omega\, K(\tau,\omega) A(\omega), \end{aligned} \tag{4.11}$$

where the kernel $K(\tau,\omega)$ is defined as

$$K(\tau,\omega) = \frac{e^{-\omega\tau}}{e^{-\beta\omega}+1} \quad \text{(fermions)}, \tag{4.12}$$

$$K(\tau,\omega) = \frac{\omega e^{-\omega\tau}}{e^{-\beta\omega}-1} \quad \text{(bosons)}. \tag{4.13}$$

The real-valued spectral function $A(\omega)$ takes the form $\rho(\omega)/2\pi$ for fermions and $\rho(\omega)/2\pi\omega$ for bosons. $A(\omega)$ is positive definite and the main quantity of interest. It obeys the property $\int_{-\infty}^{\infty} d\omega\, A(\omega) = \text{constant} < \infty$. $A(\omega)$ provides information about the excitations of the system and can be considered a generalized density of states [61].

The problem thus becomes inverting the Fredholm equation $\int d\omega\, K(\tau,\omega)A(\omega)$ in order to

obtain A. In matrix notation:

$$A = K^{-1}G. \tag{4.14}$$

.

This type of inversion problem is a ubiquitous one, appearing in areas far from those strictly associated with analytical continuation. Examples include the recovery of variety of impurity traps from ESR data, to practical applications such as medical X-ray and impedance tomography [60]. In each case, the mission is to recover relevant data given related information that might be noisy or incomplete.

However, the inversion is a notoriously difficult one for a number of reasons, primary of which is that the problem itself is ill-posed.

While the forward model $G = KA$ is well-behaved such that a given A results in an specific G, the inverse is not. There is often no unique A given a set of G data. In the event noisy or incomplete correlation data, there can be an infinite number of solutions for A given a single G. Furthermore, the inversion typically overfits noise in the high-frequency range.

In addition, the kernel matrix K's condition number is extremely large. Exponentially large and small eigenvalues with respect to β exist, making it difficult to obtain an accurate spectra of solutions that fit any predetermined criteria.

Because of these issues, tackling the inversion of the analytic continuation problem has historically centered around finding the best way to regularize the inversion, especially in the extreme frequency modes. There is no shortage of methods.

The simplest, most intuitive revolves around regularization of the form

$$A_j = \sum_k (K_{kj} + \lambda\delta_{kj})^{-1} G_k, \tag{4.15}$$

which has the effect of suppressing high frequency modes with eigenvalues of the order of β or smaller. The drawback is a loss of fine structure information of the spectral function, spurious or not. Such attempts at this type of regularization also fail to preserve the condition of $A(\omega) > 0$.

Other methods of solving include least-squares and Pade approximation. Each of these methods offer promising results, but in very specific systems that can not be applied in any way

generally. Some run into sign problems which make numerical calculations intractable [50].

For these numerous reasons, one cannot strictly search for a unique A given a set of data in G, but must often instead attempt to find a *best fit* solution, or set of solutions from which an optimal solution can be distinguished.

5 METHODS OF ANALYTIC CONTINUATION

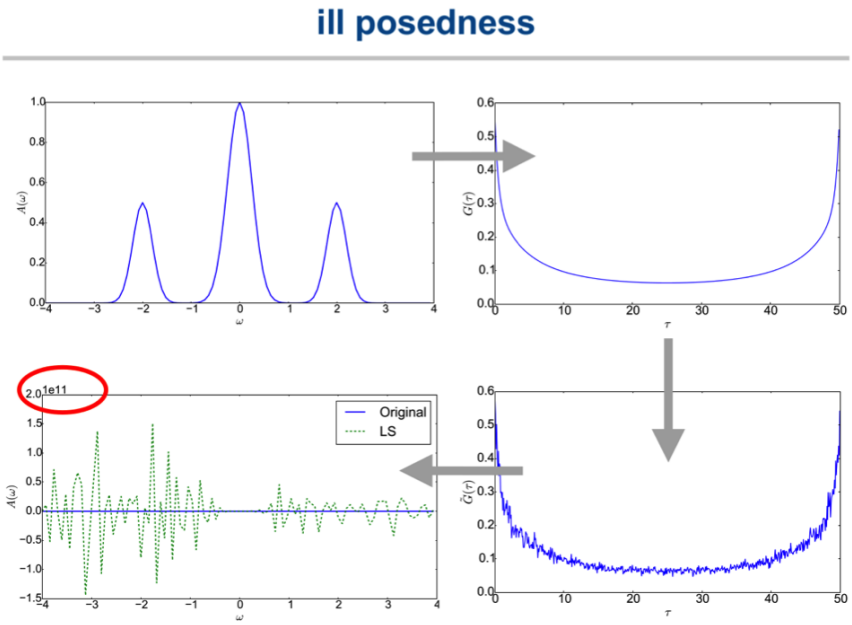

Figure 4: Ill-posedness of the analytic continuation problem. The forward model $G = KA$ yields a single solution in the top figures. The inversion is distorted by noise in G, which is amplified during the inversion, as seen in the figures on the bottom [58].

5.1 Bayesian Inference

The statistical foundation for the most prevalent methods of analytic continuation, including the Maximum Entropy Method, is Bayesian inference [30, 59].

Bayes theorem states that, given two events a and b, the joint probability is

$$\Pr[a, b] = \Pr[a|b] \Pr[b] = \Pr[b|a] \Pr[a], \tag{5.1}$$

where $\Pr[a]$ is the probability of a, $\Pr[a|b]$ is the conditional probability of a given b, and $\Pr[b|a]$ is the conditional probability of b given a.

From this starting point and integrating over all of b,

$$\Pr[a] = \int db\ \Pr[a|b]. \tag{5.2}$$

Since it is assumed that a must definitively occur at some point in this situation, normalization conditions are

$$1 = \int da\ \Pr[a], \tag{5.3}$$

$$1 = \int da\ \Pr[a|b]. \tag{5.4}$$

Making the connection to analytic continuation, the two events a and b are the functions $\overline{G}$ and A, where $\overline{G}$ is the calculated value of the correlation function and A is its true spectral representation. What is sought is the $\overline{G}$ that maximizes the joint probability of $\overline{G}$ and A.

We define $\Pr[\overline{G}|A]$ to be the likelihood function, or the joint probability of $\overline{G}$ being the correct correlator given the true spectrum A. $\Pr[A|\overline{G}]$ is the posterior probability, which is the revised probability of finding the correct spectrum given new information about $\overline{G}$. $\Pr[\overline{G}]$ is the evidence, or probability of any solution $\overline{G}$, independent of A, while $\Pr[A]$ the prior probability of obtaining the correct spectrum, based on any previously known information. Taking

$$\Pr[\overline{G}|A] = \Pr[A|\overline{G}]\ \Pr[A]/\Pr[\overline{G}], \tag{5.5}$$

integrating over A, and applying normalization conditions leads to

$$\Pr[\overline{G}] = \int dA\ \Pr[A|\overline{G}]\ \Pr[A], \tag{5.6}$$

where the evidence is treated as a normalization constant.

The initial criteria for a solution $\overline{A}$ is one that maximizes the posterior probability, which becomes a problem of specifying the likelihood function and prior probability.

The advantageous part of this approach is that the latter two quantities can be made by reasonable assumptions or by prior knowledge. What's left is choosing an appropriate optimization technique to find the best out of these possible solutions.

5.2 Maximum Entropy Method

The most widely used method at solving the analytic continuation problem is the Maximum Entropy Method (MEM). MEM is a Bayesian inference based optimization technique in which a solution is selected that extremizes a linear combination of goodness-of-fit and entropy terms.

In the case of the analytic continuation problem of QMC data, suppose that the result of sampling is a correlation function G with statistical error defined as

$$\overline{G}(\tau) = G(\tau) + \text{noise}. \tag{5.7}$$

The goodness-of-fit function is

$$\chi^2 = \int_0^\beta \frac{d\tau}{\sigma^2(\tau)} \left| \int_{-\infty}^{\infty} d\omega\, K(\tau,\omega)\, A(\omega) - \overline{G}(\tau) \right|^2. \tag{5.8}$$

χ^2 measures how closely the sampled correlation function matches that of the forward model G generated from A, and $\sigma^2(\tau)$ is the variance of each measurement in τ.

The associated entropy (Shannon) is

$$S[A] = -\int d\omega\, A(\omega) \ln \frac{A(\omega)}{D(\omega)}, \tag{5.9}$$

which quantifies the information gained due to spectral deviations from the default model $D(\omega)$. The default model is a smooth function that serves as the reference entropy configuration of the spectral function. Any prior information about the spectral function can be encoded in $D(\omega)$.

Instead of strictly minimizing χ^2 as in other numerical schemes, MEM attempts to minimize the quantity $Q = \chi^2 - \alpha^{-1} S$, where α is a parameter that controls the degree of regularization, and the entropy terms serves to reduce the probability of solutions that offer little in the way of new information. The minimization of Q is an optimization problem performed using a variation of gradient descent. The Bayesian likelihood of any spectral function being the true solution is equal to $P(A|\overline{G}) \propto e^{-Q}$ [59].

Exact solutions are found in the two limits of α. For $\alpha \to \infty$, $Q = \chi^2$, and the solution which minimizes χ^2 turns out to be that of the noisy, unregularized spectrum ($A(\omega) = \overline{A}(\omega)$).

For $\alpha \to 0$, the entropy term dominates ($Q = -S$), and the spectrum is that of the default model, minimizing the amount of new information.

For intermediate values of α, there exists a family of solutions between these two extremes, and an additional condition must be imposed to obtain a single spectrum. Between the over-fitting of $\alpha = \infty$ and the over-smoothing of $\alpha = 0$ lies some optimal range of α [55].

5.3 Stochastic Analytical Method

While classic MEM is firmly based in statistical considerations, a fatal weakness of the approach is its tendency to either overfit data or be biased towards smooth solutions, thereby washing out features of interest.

The Stochastic Analytical Continuation (SAC) approach attempts to avoid these pitfalls by taking a weighted average over all likely spectra. It has been argued that the SAC mean field configuration corresponds to the MEM approach.

Introduced by Sandvik [5], then refined by Beach [55] and others, the SAC averages across all spectra in an unbiased manner by way of thermal fluctuations. The result is spectra that preserves distinguishing characteristics that are often averaged out by MEM and other methods.

Rather than maximizing $P(A|\overline{G})$ via Q, all possible spectra are weighted by an analog fixed-temperature partition function $Z = \sum_n e^{-\beta H_n}$, where β serves as an inverse temperature parameter, and then taking a mean field approach to n to find a final solution.

In anticipation of its default model connection, an arbitrary kernel is labeled D and defines a classical field $n(x)$ by a mapping onto a unit interval [0,1]:

$$\phi = \frac{1}{m} \int_{-\infty}^{\omega} dv\, D(v), \tag{5.10}$$

where, like A, D obeys the normalization condition $m = \int_{-\infty}^{\infty} d\omega\, D(\omega)$ and is positive definite. Taking $D = m(d\phi/d\omega)$, $n(x)$ is defined

$$1 = \frac{1}{m} \int d\omega\, A(\omega) = \int d\phi\, \frac{A(\omega)}{D(\omega)} = \int_0^1 dx\, n(x) \tag{5.11}$$

under the change of variables $d\phi = dx \cdot n(x) = A(\omega)/D(\omega)$, and is dimensionless and

wholly defined in the unit interval.

Letting $mK(\tau, \omega) = K(\tau, x)$, the goodness-of-fit χ^2 is thus treated as a Hamiltonian

$$H[n] = \int_0^\beta \frac{d\tau}{\sigma^2} \left| \int_0^1 K(\tau, x) n(x) dx - \overline{G}(\tau) \right|^2 . \tag{5.12}$$

If the system is held at a constant fictitious temperature, the thermally averaged field is

$$\langle n(x) \rangle = \frac{1}{Z} \int dn \, n(x) e^{-\beta H_n}. \tag{5.13}$$

This results in a spectrum of the form

$$\langle A(\omega) \rangle = \langle n(x) \rangle D(\omega) \tag{5.14}$$

$\langle n(x) \rangle$ represents a single-parameter family of solutions which has limits that match those of the MEM. At zero temperature, or $\alpha \to \infty$, the solution is the lowest lying field configuration, analogous to the noisy, unregulated MEM limit. Conversely, in the high temperature limit $\alpha \to 0$ the solution is that of unweighted average over all possible configurations. This represents the no-information MEM default model limit, where $A = D$.

6 QUANTUM FLUCTUATION (QF) METHOD

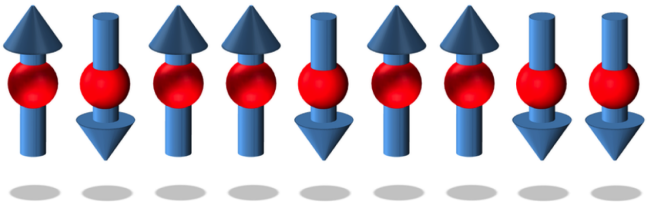

Figure 5: Linear spin-1/2 Heisenberg chain.

My area of research involves taking the SAC approach, but instead of using thermal fluctuations with mean-valued classical fields, mapping the analytic continuation problem to a finite-dimensional quantum system. Specifically, I apply the problem to a one-dimensional lattice model, where the tools of quantum mechanics and quantum information can be used to extract real-valued results from imaginary-time data.

The are several advantages to such an approach. The second quantization approach transforms the wavefunction of a complicated, high-dimensional quantum system to one of operator fields that are easy to track, all the while preserving the underlying properties of Hilbert space through the (anti-)commutative algebra of creation and annihilation operators [34].

Instead of taking a classical averaging approach in the manner of the SAC, the tools of quantum mechanics provide a readily available analogue through the concept of the expectation value,

$$\langle \phi \rangle = \text{Trace}(\rho\phi) = \sum_i p_i \langle \psi_i | \phi | \psi_i \rangle, \tag{6.1}$$

where $\rho = \sum_i p_i |\psi_i\rangle\langle\psi_i|$ is the density matrix and p_i the eigenvalues of the state $|\psi\rangle$.

What is left is to build the proper quantum mechanical model that will provide the fluctuations necessary to regularize the analytic continuation inversion.

6.1 Heisenberg Model

The ideal quantum model to represent this system of quantum fluctuations is a version of the Heisenberg model that incorporates Ising interactions and an external field [18, 21].

The spin-1/2 Heisenberg model is a statistical mechanical one in which each lattice site is occupied by a single spin degree of freedom, a magnetic moment that either points up or down $\{\uparrow, \downarrow\}$.

It is a model adept at describing the exchange interactions between spins and therefore convenient for ferromagnetism, the strongest type of magnetism in which all magnetic dipoles orient in the same direction along a particular degree of freedom [14].

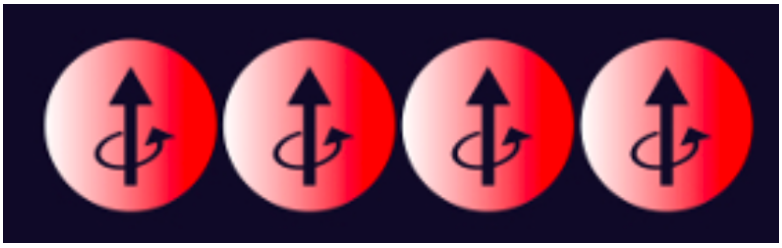

Figure 6: Ferromagnetic alignment in one of two degenerate states. In its ground state configuration, all spins align to minimize the energy of the system due to the sign of J.

In particular, a ferromagnetic system has a non-zero magnetization $M \neq 0$ in the presence of a vanishing external magnetic field $B \to 0$.

The Hamiltonian of the Heisenberg system is

$$H = -\sum_{ij} J_{ij} \hat{S}_i^z \hat{S}_j^z - \sum_i B_i^x \hat{S}_i^x, \tag{6.2}$$

where the indices i and j refer to sites on a lattice, $\hat{S}_i$ denotes the spin-1/2 operators at each site, B_i is the field strength at site i, and the exchange coupling term J_{ij} favors spin alignment for $J > 0$ and anti-alignment for $J < 0$.

Note that quantities such as the magnetic moment μ, the Lande g-factor, and the Bohr magnetron μ_B have been absorbed, resulting in B-fields with units of energy.

The model can be defined on any lattice, but for the purposes of this paper will be limited to a one-dimensional lattice where $x_1 \neq x_N$, defining a spin chain with free endpoints [7].

Spin components on the same lattice sites obey the standard angular momentum commutation rules

$$[S_i^a, S_i^b] = i\hbar\epsilon_{abc}S_i^c. \tag{6.3}$$

The projection of S_i in the z-direction take values of $m_s \in \{\frac{1}{2}, -\frac{1}{2}\}$.

For two interacting spin operators, the maximum eigenvalue for $\langle S_i \cdot S_j \rangle$ is S^2, where

$$S_{\text{tot}} = S_i + S_j, \tag{6.4}$$

leading to

$$S^2 = S_i^2 + S_j^2 + 2S_i \cdot S_j, \tag{6.5}$$

with $S_{\text{tot,max}} = S_{i,\text{max}} = S_{j,\text{max}} = 2S$ and $S_i^2 = S_j^2 = S(S = 1)$ resulting in the equality

$$\frac{1}{2}[2S(2S+1) - S(S+1) - S(S+1)] = S^2. \tag{6.6}$$

The number of spins on the chain is defined $N = L/a$, where L is the total length of the chain and a the spacing between spins.

The Hamiltonian is invariant under Z_2 symmetry when $B = 0$. In the presence of a field in the x-direction, spin exchange symmetry is broken and ground state degeneracy lifted due to Zeeman effects [11].

For this particular one dimensional model, we assume the absence of interactions in the x- and y- directions ($J_{ij}^z \neq J_{ij}^x = J_{ij}^y = 0$), and a B-field presence in only the x- and z- directions.

Consequently, the non-commuting transverse term in the x-direction introduces quantum fluctuations in the model, responsible for a quantum phase transition from an ordered ground state to a disordered paramagnetic phase at a critical value B_c^x [9, 20, 56].

Below this critical field value, there exists two degenerate ground states with ferromagnetic ordering with all spins pointing up or all spins pointing down [3, 8].

Above B_c^x, fluctuations are responsible for an exponentially small energy gap Δ between the

two lowest lying energy states.

Extending the model further, we can assume that at each site there is small free energy associated with the field operator in the order $\gamma \approx \hbar k$, where k denotes the angular wavenumber. Inserting this dispersion term into the Hamiltonian, and absorbing $\hbar$ and k so B^z will have units of energy, leads to a generalized Hamiltonian of the form

$$H = -\sum_{ij} J_{ij} \hat{S}_i^z \hat{S}_j^z - \sum_i B_i^z \hat{S}_j^z - \sum_i B_i \hat{S}_i^x. \tag{6.7}$$

6.2 Quantum Fluctuation Hamiltonian

With the Heisenberg chain defined in terms of its Hamiltonian, we return to the classical field Hamiltonian of the stochastic analytic approach

$$H[n] = \int_0^\beta \frac{d\tau}{\sigma^2} \left| \int_0^1 K(\tau, x) n(x) dx - \overline{G}(\tau) \right|^2 \tag{6.8}$$

and expand it into tensor notation

$$H = K_{ij} K_{ik} n_j n_k + 2 K_{ij} G_i n_j + G_i^2, \tag{6.9}$$

where all values are taken to be real, and the last term is recognized to be constant.

There appears to be natural connection between the Hamiltonians of the quantum Heisenberg chain and classical thermodynamical system of the SAC if one considers the following mappings

$$-J_{ij} \leftrightarrow K_{ij} K_{ik} = V_{jk}, \tag{6.10}$$

$$-B_i^z \leftrightarrow 2 K_{ij} G_i = \gamma_j, \tag{6.11}$$

$$S_i^z \leftrightarrow n_i. \tag{6.12}$$

The interaction term V_{jk} of the SAC Hamiltonian shows up as a coupling term between neighboring spin sites and the free dispersion coefficient γ_j takes the role of a single particle field coefficient.

An additional chemical potential term is added to maintain normalization throughout the convergence to a final solution, later discussed in section 10.3, resulting in a general form of the QF Hamiltonian

$$H = -\sum_{ij} V_{ij}\hat{n}_i^z\hat{n}_j^z - \sum_i \gamma_i^z\hat{n}_j^z - \sum_i B_i\hat{S}_i^x - \sum_i \mu_i\hat{n}_i^z. \tag{6.13}$$

6.3 Zeta Mapping

All of the necessary components appear to be in place. From the classically modeled goodness-of-fit χ^2 we have connected to a quantum physical model for which we have available tools to solve. What's left is to make explicit a mapping between the two-state qubit Hilbert space to the space of classical fields $n(x)$.

$n(x)$, as defined by the SAC approach, is positive definite and resides in the unit interval. Its quantum field equivalent should meet the same criteria, and any additional ones with respect to the quantum framework in which it is to be expressed.

To connect the generalized Heisenberg Hamiltonian with the one derived from the SAC, we use a $S^z \rightarrow n$ mapping that meets the following criteria:

1. the positivity and normalization of n are preserved
2. n spans the space of all real numbers
3. $n \rightarrow 1$ as $m_s \rightarrow 0$

The mapping chosen for the models of this work is

$$n_i = \frac{1 + 2\langle\hat{S}_i^z\rangle}{1 - 2\langle\hat{S}_i^z\rangle}, \tag{6.14}$$

which takes the physical space of the spin onto the unit interval $[-\frac{1}{2}, \frac{1}{2}]$, enforcing the positive definite nature of $n(x)$ and conveniently making a $\hat{S}_i^z$ expectation value of zero correspond to the desired $n = 1$ point. With a strong enough transverse field, all three requirements are easily met.

Several different mappings were also tested, using sinusoidal superposition and arctan approximations [36]. The zeta mapping used for the models in this research showed by far the best results. It is possible, however, that depending on the physical parameters of the underlying model in question, alternate models may prove to be a better fit.

For the qubit Heisenberg model, it is expected that most fluctuations will occur around an interval of $m_s = 0$, or $n = 1$. The zeta mapping proves to be robust around the $m_s = 0$ point, its overall noise at a minima this very point as seen in the figure.

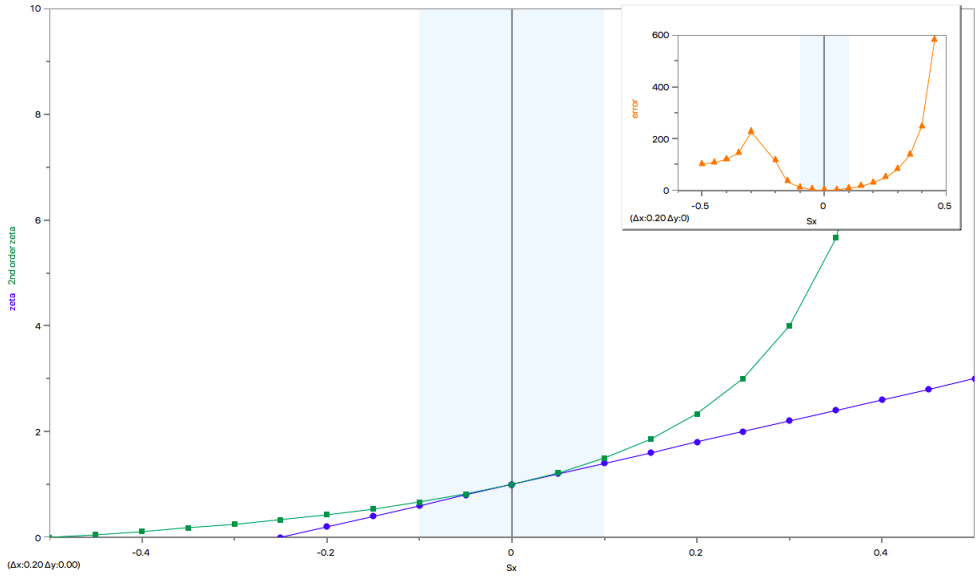

Figure 7: Mapping of n in a unit interval. Insert shows the noise associated with each point. The accuracy of the mapping is at its peak near $n = 1$.

The associated eigenstates become

$$|n = 0; m_s = -1/2\rangle, \tag{6.15}$$

$$|n = \infty; m_s = 1/2\rangle. \tag{6.16}$$

Using the power series expansion

$$\frac{1+x}{1-x} = 1 + \sum_{n=1} 2x^n \tag{6.17}$$

we can adopt a linearized mapping,

$$n_i = \frac{1 + 2\langle \hat{S}_i^z \rangle}{1 - 2\langle \hat{S}_i^z \rangle} \approx 1 + 4\langle \hat{S}_i^z \rangle, \tag{6.18}$$

which achieves a good approximation for the narrow band of $\langle \hat{S}_i^z \rangle$ under consideration, as seen in figure 7.

Ignoring the constant term, the *generalized* Heisenberg model takes the form

$$H = V_{jk}(1 + 4\hat{S}_j^z)(1 + 4\hat{S}_k^z) + \gamma_i(1 + 4\hat{S}_i^z), \tag{6.19}$$

where information about G and K are encoded within V and γ, and n is encoded within the spins. Thus, if one is able to minimize the Hamiltonian to find the ground state configuration, the expectation values of the spins will carry information about the spectral function that can be extracted through n.

H in this form, however, points to a semi-classical model. For most values of γ and system size N, one expects ground states with large numbers of spin expectation values near the $m_s = 1/2$ or $m_s = -1/2$ limits. Consequently, the proposed QF-Heisenberg model breaks down due to the $n = 1 + 4\langle \hat{S}_i^z \rangle$ approximation. The information encoded within the spins will be noisy and the ground state degenerate.

Taking advantage of the properties of quantum systems, a regularization term is reintroduced in the form of the transverse field in the x-direction,

$$H = V_{jk}(1 + 4\hat{S}_j^z)(1 + 4\hat{S}_k^z) + 2\gamma_i(1 + 4\hat{S}_i^z) - B_i^x \hat{S}_i^x. \tag{6.20}$$

The transverse field serves as a regularization parameter to allow tunneling between solutions. The non-commuting S_x term leads to quantum fluctuations throughout the system and breaks ground state degeneracy. As seen in the relation $S^2 = S_x^2 + S_z^2$ and by conservation of S^2, for extremely large transverse terms the expectation values for the S_z terms approach zero ($n \to 1$), resulting in the extracted spectral function smoothing into the default model.

Somewhere between a very large transverse field and one in which $B_i^x = 0$ (the standard

Heisenberg model) lies an ideal range which regularizes the noise of $\overline{A}$, yet preserves sharp, distinguishing characteristics of the underlying spectra.

The Hilbert space of the model has a dimension 2^N. In the presence of the transverse field, such techniques such as the Bethe Ansatz method and diagonalization are infeasible for large N [4]. However, matrix product states (MPS) are ideally suited to treat 1D systems which have gapped energy profiles.

The Density Matrix Renormalization Group (DMRG) is an algorithm that utilizes MPS to obtain ground states accurately and efficiently.

7 COMPUTATIONAL ANALYSIS

7.1 MPS/DMRG

An obstacle to the study of many body systems is the number of parameters necessary to describe such a system in full. The dimension of the Hilbert space needed to accommodate such a description increases exponentially in the size of the lattice, rendering any attempt to solve such a system exactly through diagonalization or other numerical means impossible.

DMRG tackles such a problem in a way that scales polynomially rather than exponentially. The basic idea of the DMRG is to divide the physical system, or lattice of sites, into "blocks". Then the Hamiltonian of a superblock consisting of several of these blocks is diagonalized to form a density matrix. Only the most significant eigenstates from this block density matrix are kept, as they most accurately represent the state of the system as a whole, ie the block plus the rest of the lattice [19].

The success of DMRG in finding the ground state of gapped 1D systems is tied to its MPS structure and the area law, which places an upper bound on the correlation length in a system that is proportional to its surface size [57]. In the case of a 1D lattice this upper bound is a constant, meaning information in strongly correlated systems can be effectively encoded in lower dimensional spaces [16].

Any N-body, one-dimensional quantum system can be expressed as a wave function

$$|\psi\rangle = \sum_{i_1 i_2 \ldots i_N} \Psi_{i_1 i_2 \ldots i_N} |i_1 i_2 \ldots i_N\rangle \tag{7.1}$$

in Fock space, where $\Psi_{i_1 i_2 \ldots i_N}$ is a rank-N tensor [57]. Using this representation, however, is arduous since it suffers from an exponential scaling as the total Hilbert space is d^N, where d is the local dimension at each lattice site ($d = 2$ for a qubit system).

The tensor train/MPS representation, however, avoids such dimensionality issues by decomposing the tensor into a set of N lower ranked tensors,

$$|\psi\rangle = \sum_{i_1 i_2 \ldots i_N} M_{i_1} M_{i_2} \ldots M_{i_N} |i_1 i_2 \ldots i_N\rangle. \tag{7.2}$$

Each M is a matrix of dimension $D \times D$, where D represents the hyper-parameter virtual "bond" dimension. Each A has a dimension d which is that of the physical Hilbert space.

The process of finding the most significant eigenstates is done by way of singular value decomposition (SVD) of each MPS as the algorithm sweeps back and forth,

$$M_i = U_{\alpha_1} S_i^{\alpha_1, \alpha_2} V_{\alpha_2}. \tag{7.3}$$

Both U and V are unitary matrices whose columns (rows) are eigenstates of M. S is a block matrix whose diagonal elements are the singular values of M.

As the DMRG algorithm sweeps through each MPS, only the D most significant singular values are kept. The rest are discarded, and the associated columns (rows) for U and V are eliminated.

The decomposition is then contracted to form an adjusted M, and the algorithm continues its sweep to the next site. The representation therefore scales polynomially with N instead of exponentially, while the most significant correlation information remains intact.

The resulting MPS/reduced tensor representation can then be treated as a wavefunction and used to extract properties of the system, such the expectation values of an operator and the ground state energy.

7.2 ITensor

Intelligent Tensor (Itensor) is a C++ library for implementing tensor network calculations. Its DMRG routine conveniently outputs ground state calculations in MPS form, and its implementation is adaptive and efficient [39].

Going back to the SAC-Hamiltonian, the tensor representation is

$$H = V_{jk}(1 + 4\hat{S}_j^z)(1 + 4\hat{S}_k^z) + 2\gamma_i(1 + 4\hat{S}_i^z) - B_i^x\hat{S}_i^x - \mu_i^z\hat{S}_i^z. \tag{7.4}$$

An additional z-field term μ_z is added for normalization of n. Since $\sum_i n_i\Delta x_i = 1$, then for an average site separation $\overline{\Delta x}$ is in the unit interval

$$\sum_i n_i = \frac{1}{\overline{\Delta x}} = N. \tag{7.5}$$

So

$$N = \sum_i n_i \approx \sum_i (1 + 4\langle\hat{S}_i^z\rangle) = N + 4\sum_i \langle\hat{S}_i^z, \rangle \tag{7.6}$$

and the total magnetization $M = \sum(\hat{S}_i^z)$ for the site set is approximately zero. The μ_i parameter serves as a chemical potential term that allows the energy per site be tuned up or down until the normalization requirement is met, and can be adjusted dynamically as needed through each iteration of the algorithm.

Itensor allows each Hamiltonian term to be added individually, or summed by iteration, using the top-level AMPO (automatic matrix product object) system, which is extremely convenient for many-body systems with a large number of degrees of freedom.

The Hamiltonian is then converted from a top-level AMPO to a final matrix product object (MPO), so block diagonalization of the density matrix can be performed. The number of sweeps, bond dimensions per sweep, and error cutoff are parameters that can be decided prior to implementation. From this, the ground state energy and wavefunction can be found in terms of its tensor representation.

SAMPLE CODE

```
auto M = K * prime(K,m); //interaction coefficients J(ij)
    auto N = 2 * G * K; //free dispersion coefficients
    auto O = G * G;     //scalar term


    //ampo takes a running sum of all Hamiltonian terms
    //Nz is custom operator 1+4*Sz
    for (int j = 1; j <= freqpoints; ++j){
       for(int k = 1; ( k <= freqpoints); ++k){
          ampo += -(M.real(m(j), prime(m)(k))), "Nz",j, "Nz", k;
       }
       ampo += (N.real(m(j))), "Nz",j;
       ampo += 0.5*xfield[j-1], "S+",j;
       ampo += 0.5*xfield[j-1], "S-",j;
       ampo += zfield[j-1],"Sz",j;

    //creates Hamiltonian as matrix product operator
    auto H = toMPO(ampo,{"Exact=",false}); //converts ampo to MPO
       that can be used in DMRG algo

    auto sweeps = Sweeps(5); //number of sweeps is 5
    sweeps.maxdim() = 10,20,100,100,600;
    sweeps.mindim() = 10;
    sweeps.cutoff() = 1E-18;
    //sweeps.noise() = 1E-8;


    //DMRG algorithm that returns energy and final MPS
    auto [energy,psi] = dmrg(H,psi0,sweeps,{"Quiet",true});
```

8 PARAMETERS AND CONSTRAINTS

8.1 Transverse Field

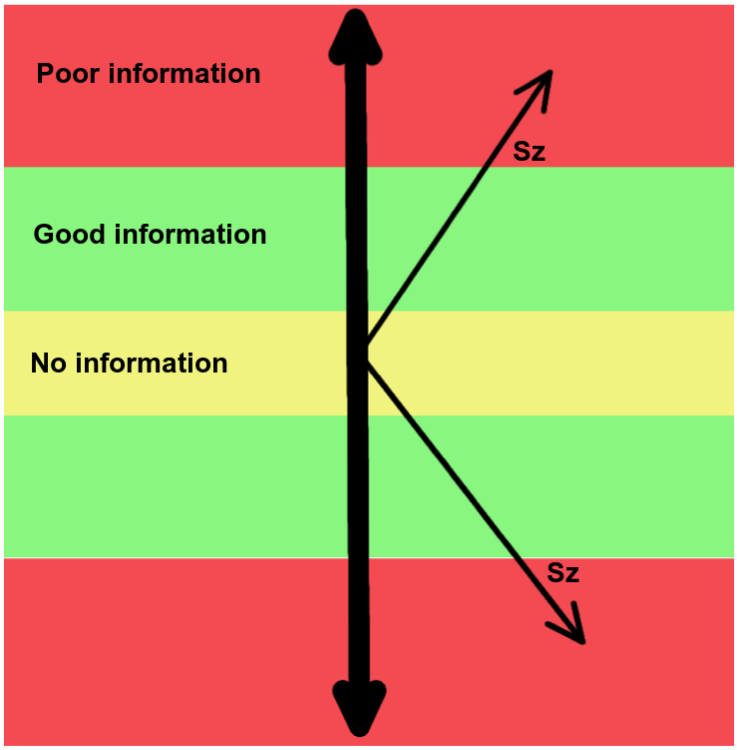

Figure 8: Poorly regularized spin regime, corresponding to momenta existing outside of the limits of the zeta mapping from spin space to that of the quantum field operator.

The main parameter used in the code is the transverse x-field, which narrows the width of the expectation value band of the spin, reducing noise and regularizing the spectrum.

Similar to the MEM and SAC approaches, the QF approach requires regularization of the analytic continuation inversion in order to find a best fit spectra. For the MEM, this parameter is the α value associated with an entropy prior that pulls χ^2 away from its absolute minimum value, which often does not coincide to a best solution regardless. For the SAC, regularization is by a statistically weighted average from the partition function at a fixed temperature.

With the QF, the primary regularization parameter is the transverse field B^x, which when

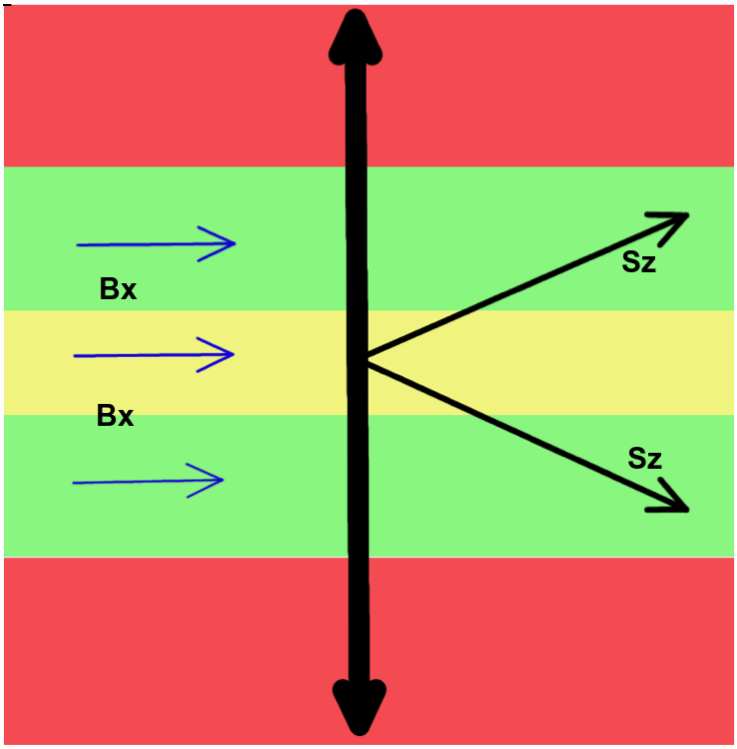

Figure 9: Regularized spin regime, corresponding to momenta existing inside of the limits of the zeta mapping from spin space to that of the quantum field operator. Information residing within this zone is considered either good or non-existent.

applied to the Heisenberg chain of spin $-1/2$ particles, couples with the spin momentum to influence its projection upon the z-axis.

The magnitude of B^x necessary to regularize an inversion depends on a number of factors, including the complexity of the spectrum, its integral size, and the amount of noise at each imaginary time point describing the correlator.

Figure 10 shows the effect of an inversion on a circular spectra with B^x values of 4.0×10^{11}, 6.0×10^{11}, and 8.0×10^{11}. Note that the spectra are not optimized in B^x or β, yet the effect of the field in the regularization of the spectrum $\overline{A}$ is apparent.

For this spectrum, the lowest field value that could be achieved was approximately 3.0×10^{11} before negative n values became unavoidable. The field value that corresponded to the lowest internal energy of the Heisenberg chain was 6.0×10^{11}.

At $B^x = 4.0 \times 10^{11}$, the information encoded by the zeta mapping introduces a high level of noise, with n field values for some sites being outside of the $.88 < n < 1.17$ range. At $B^x = 8.0 \times 10^{11}$, there is still a good fit, but the remnants of the default model are visible on the

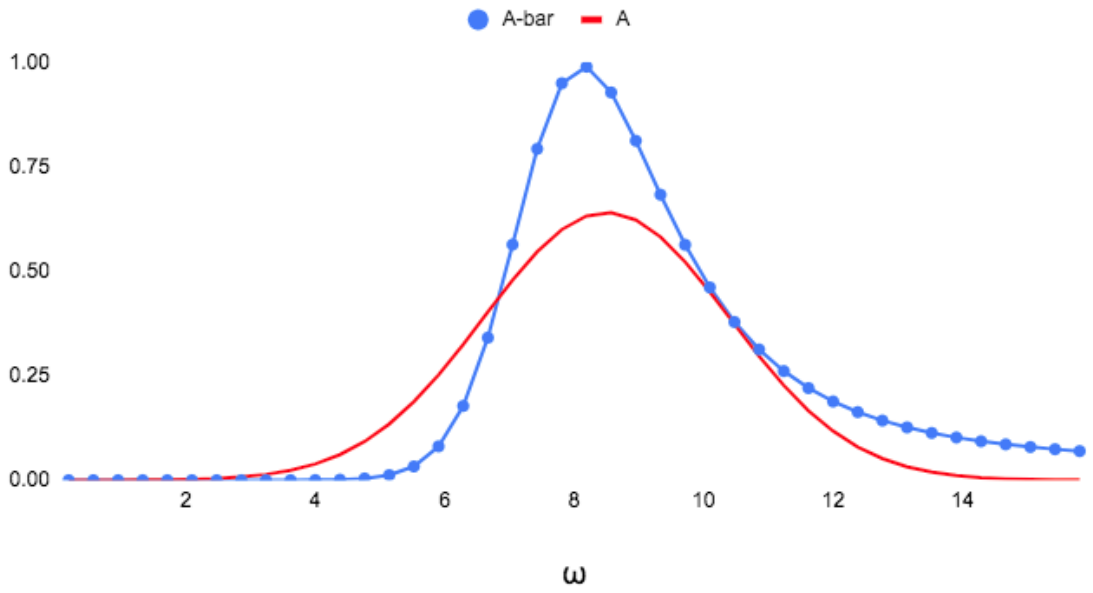

Figure 10: Gaussian spectrum with a coupled $B^x = 4.0 \times 10^{11}$ field to the spins.

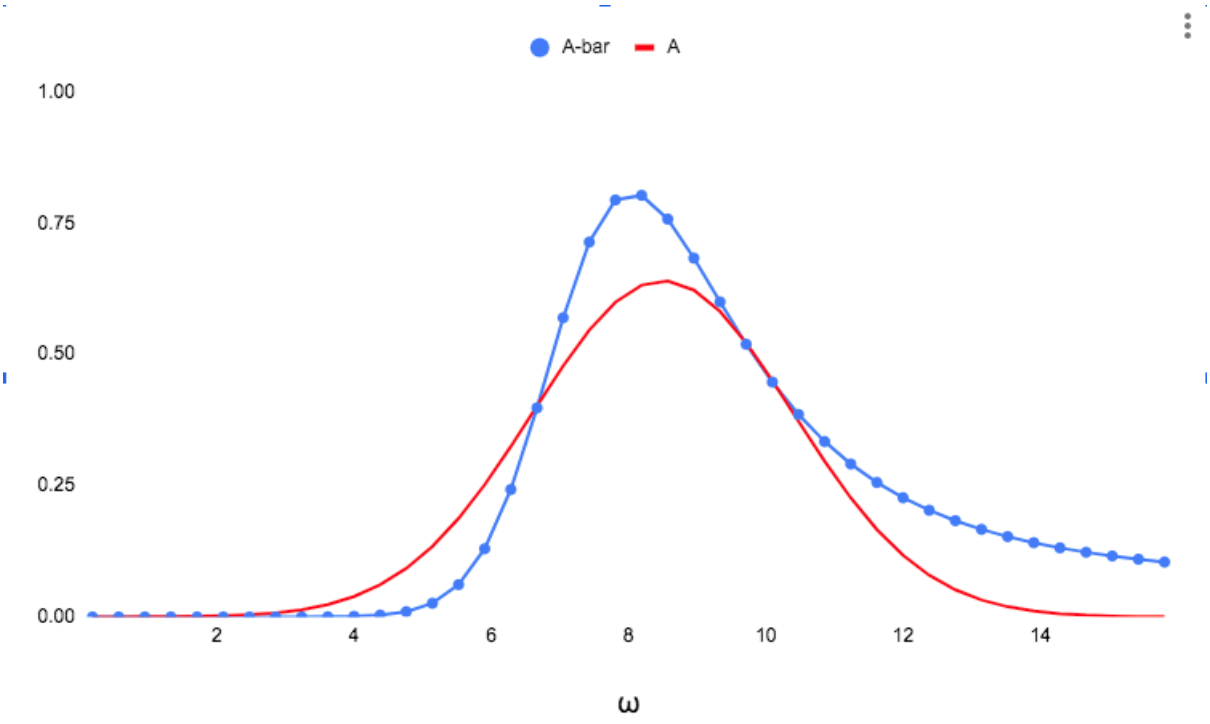

Figure 11: Gaussian spectrum with a coupled $B^x = 6.0 \times 10^{11}$ field to the spins.

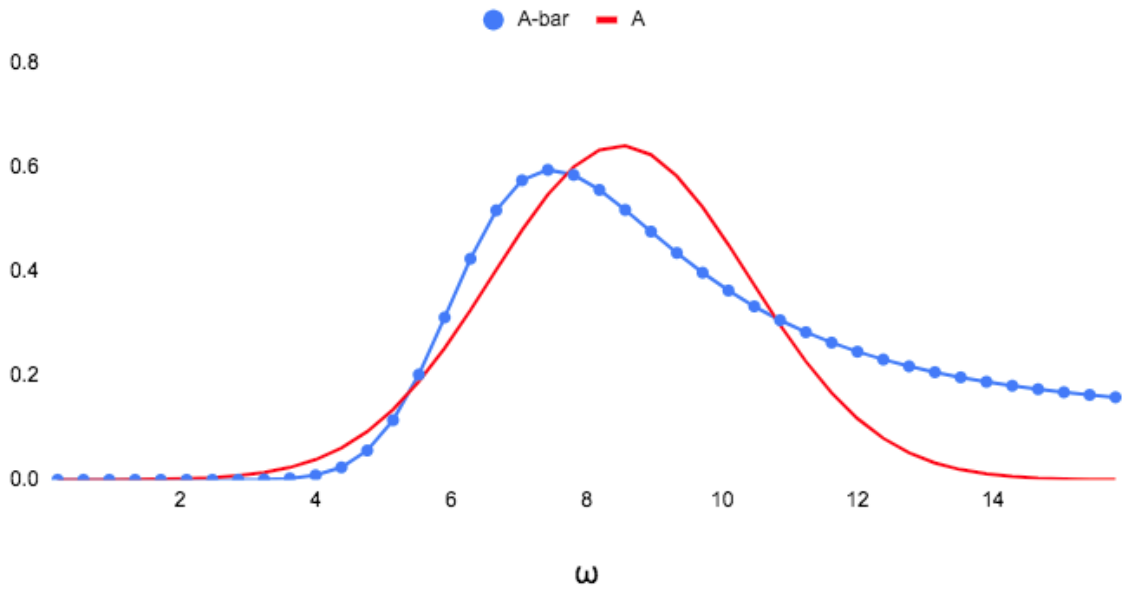

Figure 12: Gaussian spectrum with a coupled $B^x = 8.0 \times 10^{11}$ field to the spins.

right endpoint range of $\overline{A}$.

In terms of the Heisenberg model, one can think of the behavior as representing the approach of different quantum phases.

For $B^x \gg J, \gamma$, the transverse term dominates the QF Hamiltonian. In this range, quantum fluctuations are small and the information learned is minimized as seen by the Shannon entropy term $(A(\omega)/D(\omega)) \approx 1$.

At low B^x values approaching 0, the other terms of the Hamiltonian are dominant. In most cases, $\sum_j J_{ij} > \gamma_i$, resulting in a state that favors a ferromagnetic or antiferromagnetic ordering depending on the sign of J. In this range, fluctuations are large, veering into the previously established high-error zone of n-values.

At intermediate B^x, the transverse field suppresses the FM or AFM ordering, resulting in fluctuations that are encoded with good information.

For most samples, the optimized B^x value lies close to a critical value that separates the system from its ordered and order-suppressed phase.

In this optimal range for $T > 0$ and $B^x > B^x_c$, the system in in the lower range of its quantum critical phase, where both quantum and thermal fluctuations are present.

Although the quantum critical points of the system are not formally that of the limits of

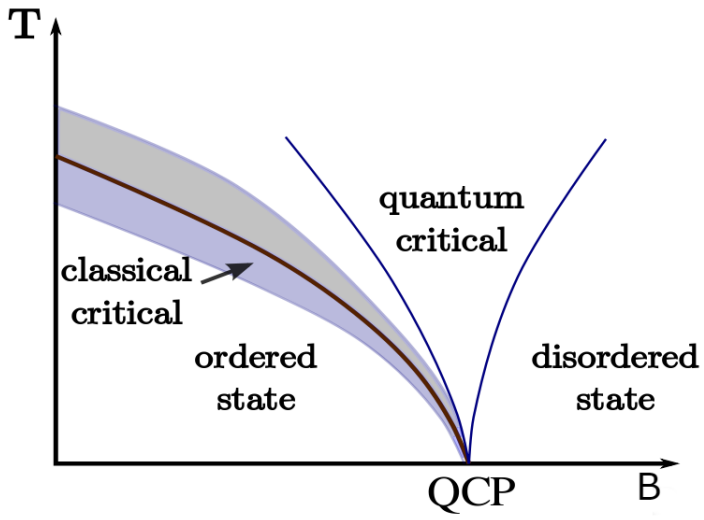

Figure 13: Quantum phase diagram. For $T > 0$ there exists a quantum critical region. On the lower B edge of this region, spins are encoded with the best information. Information in the ordered region is noisy and the Heisenberg model favors a FM state. Information in the disordered region is suppressed by the strong transverse field.

the MEM and SAC, the behavior is similar. At the high transverse field limit, the state can be considered to be in a disordered phase, and $\overline{A}$ settles to that of the encoded default model $D(\omega)$.

At the low transverse field limit, the system exhibits long range order. The resultant inversion solution is noisy and poorly regularized, any information gained washed out in the "bad information" regions of the zeta approximation.

In between these two phases lies a critical region, the lower end of which is effected by both quantum and thermal fluctuations, and gives the best data encoded within each spin.

In the examples presented in this dissertation, the ideal field strength can range anywhere between 5000 and 10^{19}. Lower values result in increased noise, as the S^z terms of the Hamiltonian dominates, pushing the model into a noise-fitting region. Higher values erroneously smooth out distinguishing features of the spectrum, leading to a zero-information default model solution.

8.2 Beta

The variable β serves as an fixed inverse temperature parameter for the quantum system in thermal equilibrium.

As seen previously, this parameter served as the primary regularization parameter for the SAC, influencing the magnitude of thermal fluctuations as the system moves through phase space.

Although the QF deals with quantum systems instead of classical ones at a fixed-temperature, the optimization of the β parameter still serves as a secondary means by which to control fluctuations.

At low temperatures near $T = 0$ ($\beta \to \infty$), the system reduces to that of one with two possible phases, the noisy, ordered (anti-)ferromagnetic state or the polarized, disordered state where spin alignment strongly favors the x-direction [14].

At higher temperatures ($\beta \to 0$), a quantum critical region widens, the lower transverse field limit of which is generally where information about the spectrum $A(\omega)$ is maximized.

Viewing in terms of the interaction tensor $V = K^{-1}K$, we see that as $\beta \to 0$ (fermionic case), K is suppressed as $\tau_{\max} = \beta$ and the denominator approaches a maximum of 2. As $\beta \to \infty$, the behavior of $K \approx e^{-\omega\tau}$ means that any change in A results in an enhanced effect in $G(\tau)$, especially in the high ω range, in the absence of a high measure of regularization of the kernel itself.

8.3 Chemical Potential

Since the Heisenberg lattice is a thermodynamic system, there exists a free energy variance of the system with respect to the change in particle number N, the chemical potential μ.

In the QF Hamiltonian, it is encoded as a parallel field parameter μ_i. Raising or lowering it acts to preserve the normalization of the wavefunction throughout each amplitude update.

Consider the number operator N in the second quantization representation, defined as

$$N = \sum_i \psi_i^\dagger \psi_i = \psi_\uparrow^\dagger \psi_\uparrow + \psi_\downarrow^\dagger \psi_\downarrow, \tag{8.1}$$

where $i \in \{\uparrow, \downarrow\}$, and the ψ's represent creation and annihilation operators as defined in Chapter 1.

The spin operator in terms of quantum operators is defined

$$S = \sum_{ij} \psi_i^\dagger S^{ij} \psi_j, \tag{8.2}$$

where the spin matrices in the standard basis are

$$S^x = \begin{pmatrix} 0 & 1 \\ 1 & 0 \end{pmatrix}, \quad S^y = \begin{pmatrix} 0 & -i \\ i & 0 \end{pmatrix}, \quad S^z = \begin{pmatrix} 1 & 0 \\ 0 & -1 \end{pmatrix}. \tag{8.3}$$

So $S^x = \psi_\uparrow^\dagger \psi_\downarrow + \psi_\downarrow^\dagger \psi_\uparrow$. Then commutation with the number operator $N = \sum_i \psi_i^\dagger \psi_i$ leads to

$$\begin{gathered} \psi_\uparrow^\dagger \psi_\downarrow \psi_\uparrow^\dagger \psi_\uparrow + \psi_\downarrow^\dagger \psi_\uparrow \psi_\uparrow^\dagger \psi_\uparrow + \psi_\uparrow^\dagger \psi_\downarrow \psi_\downarrow^\dagger \psi_\downarrow + \psi_\downarrow^\dagger \psi_\uparrow \psi_\downarrow^\dagger \psi_\downarrow \\ -\psi_\uparrow^\dagger \psi_\uparrow \psi_\uparrow^\dagger \psi_\downarrow - \psi_\downarrow^\dagger \psi_\downarrow \psi_\uparrow^\dagger \psi_\downarrow - \psi_\uparrow^\dagger \psi_\uparrow \psi_\downarrow^\dagger \psi_\uparrow - \psi_\downarrow^\dagger \psi_\downarrow \psi_\downarrow^\dagger \psi_\uparrow \end{gathered}. \tag{8.4}$$

Since the creator and annihilator act on $|n\rangle$ by way of the operations

$$\psi^\dagger |n\rangle = \sqrt{n+1}|n+1\rangle, \tag{8.5}$$

$$\psi |n\rangle = n|n-1\rangle, \tag{8.6}$$

then the quantum number N is not conserved, and consequently the normalization condition for A is not met.

Instead, we can pump energy into the system throughout the run of the program by way of the designated chemical potential parameter. The result is to add enough potential energy with each update to keep the total magnetization M close to 0 and preserve the normalization of the underlying Heisenberg wave function after each pass through the DMRG algorithm.

The variable CONVERGERATE acts as sort of a rate controller for the chemical potential. The higher the rate, the more chemical potential is input the system with each iteration, increasing or decreasing the speed at which the system returns to the proper condition to perform another update of $\overline{A}$.

A convergence rate of 50x is adequate for most models, but this can be adjusted accordingly before implementation of the run or dynamically.

It is often advantageous to find a best initial chemical potential level in a preprocessing

stage, although not necessary because the converge rate variable is designed to systematically lower (or raise) the system to the proper level after an adequate number of loops.

8.4 ITensor Parameters

The iTensor library has a set of user-specified parameters that can be set prior to implementation of the DMRG algorithm.

The main ones are the maximum bond dimension for each sweep and the error cutoff. The maximum bond dimension specifies the number of virtual bonds between tensors during truncation in the SVD process. The error cutoff specifies the number of significant figures for the truncation error.

Each parameter's purpose is to aid in not only accuracy, but efficiency. A maximum bond dimension of $5000 - 10000$ on a final sweep was found to be more than adequate, as anything more resulted in no better convergence of spectra.

Despite the amount of numerical accuracy required for the QF method, an error cutoff of 10^{-6} was found sufficient in all cases. Tests were performed with truncation errors all the way to 10^{-15}, with no discernible increase in accuracy but an exponential increase in time to convergence.

8.5 Constraints

In the progression of the study of the stochastic analytic approach to the inversion problem, several methods of spectral constraints have been identified and utilized to further optimize parameters [26, 28]. Several of these are in turn used for QF sampling.

The primary constraints utilized in my research were the discretization of τ and ω and endpoint optimization.

For the spectra analyzed in the results, all amplitudes were sampled onto fixed ω grids with homogeneous spacing between sites.

Grid spacing is shown to have a pronounced effect on spectra, especially those with asymptotic behavior that can skew the computed normalization $\sum_i A_i \Delta\omega_i$. Optimized grid spacing

also reduces the effects of over-fitting to the correlative noise in G, and prevents the under-fitting of data.

In addition, choosing the proper grid can reduce the effects of spectral leakage into regions of low information or high noise, or allow the release of weight from areas prone to overfitting. Both situation can result in spurious compensatory fitting in other parts of the spectrum.

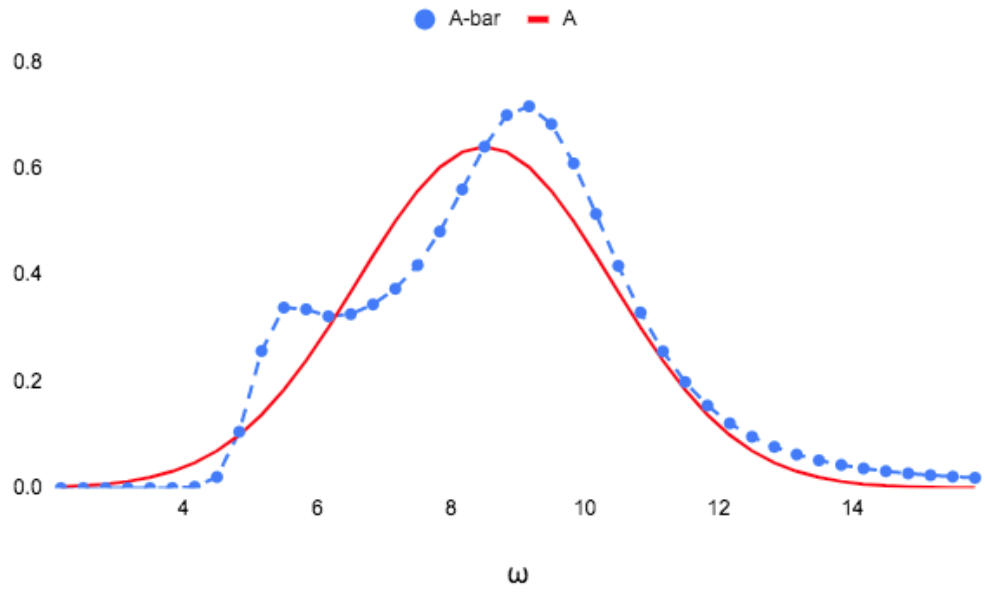

Figure 14: Gaussian spectrum with endpoints from $\omega = 2$ to $\omega = 16$.

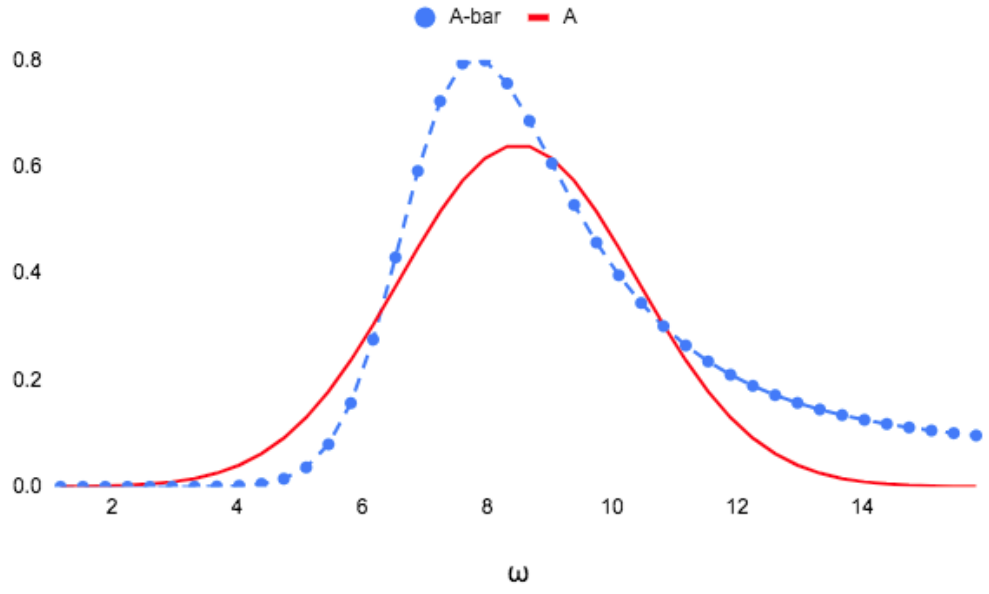

Figure 15: Gaussian spectrum with endpoints from $\omega = 1.5$ to $\omega = 16$.

Figures 14 and 15 show the same Gaussian spectrum and identical spin chain parameters,

but with different endpoint values for the frequency grid. Figure 15 shows a better fit due to the release of weight constraints on the left side of the spectrum.

Grid sampling, or the dynamical adjustment of grid density based on predetermined criteria, has shown promising results in simple cases with small N_ω, but for samples presented in the Results section of this dissertation, fixed ω grids were used extensively [41].

A measured approach to τ discretization can also aid in optimized spectral fitting. It is well-observed that inversion methods risk smearing out fine structure information in the high frequency range.

An approach to combat such loss is to use smaller time increments to regulate the pronounced effect of larger ω values in the kernel stemming from the factor of $e^{-\omega\tau}$.

For most spectra during the course of research, the number of imaginary time points numbered in the tens, in a range of $N_\tau = 30$ to $N_\tau = 100$. However, the distribution of these time points need not be necessarily uniform [5].

For several spectra of complicated shapes, τ grids of exponentially decreasing spacing were used for the advantage of having both large and small $\Delta\tau$ spacing, to various levels of success.

9 PROGRAM IMPLEMENTATION

The algorithm that implements the QF method is a multi-step process.

The first step is to initialize constraints and parameters such a the initial B^z, the discretization mesh of τ and ω, and the endpoints of the calculated spectrum $\overline{A}$. Any necessary fine tuning to the chemical potential and its input rate are also made to aid in the speed of convergence to a possible solution.

```
double transverse = 1949500000; //transverse field//.88749500000
double parallel = 6100000;//-324.5;//-4.545(80) //parallel field
double timehigh = 10; //max time value
double timelow = 0; //min time value
double timewidth = timehigh - timelow; //time interval
const int timepoints = 30; //number of time data points
int mid = timepoints/2;
double timeinterval = (double)timewidth/(double)timepoints;
   //interval of time values
const double timebeta = timehigh - timeinterval/2.0; //period of
   function


int invl = 10; //interval around sign change


double freqhigh = 4.0; //high frequency value
double freqlow = -4.0;
```

In some instances, dynamic adjustment to the transverse field is also specified to make sure n remains in the good information zone. In these cases the range will be $1.17 > n(\omega) > 0.88$.

```
if (nfield[v] > 1.17 || nfield[v] < .88) {
```

```
            xfield[v] = xmhigh*xfield[v];
        }
        else if (nfield[v] < 1.001 && nfield[v] > .999){
            xfield[v] = xmlow*xfield[v];
        }
    }
```

For sites with calculated field values falling outside of this range, it is possible to either increase the overall transverse field of the system until all values fall within that threshold, or to merely adjust the field around the noisy area of the spectrum.

To create simulated QMC noise of the form

$$\overline{G}(\tau) = G(\tau) + \text{statistical noise.} \tag{9.1}$$

an initial spectrum is taken and converted to $G(\tau)$ using the forward model $K(\tau,\omega)A(\omega)$. Taking $G(0)$, Gaussian noise is created with maximum σ_{max} = noise level $*$ $G(0)$.

```
gnoise[gg] = pow(-1,(rand() %
   2))*rand_normal(.0005*corrarray[0],.34*.0005*corrarray[0]);
        noisycorrarray[gg] = sqrt(timeinterval)*(corrarray[gg]
           + gnoise[gg])/((abs(gnoise[gg])));
```

Using $\overline{G}$ and K, tensors V and γ are encoded and prepared for MPS conversion.

Itensor takes the defined parameters for the number of sweeps, the maximum bond dimension each sweep, and the cutoff, before taking V and γ, converting them to a MPS representation, and finding the ground state configuration and associated energy.

```
auto H = toMPO(ampo,{"Exact=",false}); //converts ampo to MPO
   that can be used in DMRG algo

   auto sweeps = Sweeps(5); //number of sweeps is 5
   sweeps.maxdim() = 10,20,100,1400,2600,3400, 5600,10800,350000;
```

```
sweeps.mindim() = 10;
sweeps.cutoff() = 1E-6;
```

The program then loops, updating the amplitudes $\overline{A}_i$ as it does so. Each time, Itensor finds the ground state of the QF Hamiltonian and calculates $\overline{A}$. This $\overline{A}$ then be used as a new D for the next loop. Each new D is encoded with learned information about the true spectral function from the prior iteration.

Because of the transverse term B^x, normalization of the Heisenberg wavefunction is not preserved from loop to loop. To enforce $m = \sum_i A_i\omega_i = \sum_i D_i\omega_i$, each spectral amplitude $\overline{A}_i$ is scaled by m before being reassigned as D_i.

```
dftratio = dftsum0/dftsum;

   double dftdvg = abs(1.0 - dftratio);
   if(intcount%10==0){

   while (dftdvg > .0001){

      for (int j = 0; j < freqpoints; ++j){
         smootharray[j] = dftratio*smootharray[j];//

      }
      dftsum = 0.0;
      for (int v = 0; v < freqpoints; ++v){
         dftsum += freqinterval * smootharray[v];
         xsumarray[v] = dftsum;
         //cout << xsumarray[v] << endl;
      }

      dftratio = dftsum0/dftsum;
      dftdvg = abs(1.0 - dftratio);
```

```
        // cout << " dftsum " << dftsum << endl;
    }}
```

In the Bayesian sense, in order to maximize $\Pr[\overline{G}|A]$, each $\overline{A}$ is used as a prior information to revise $\Pr[A|\overline{G}]$. As such, each new loop is a self consistency check.

Because of the risk of error propagation with each iteration, $\overline{A}$ should be found in as few updates as possible, which means setting B^x to an immediate initial value, and turning it off for successive loops so the fluctuations will maximize itself within the good information range.

10 RESULTS

10.1 Methodology

With a system of parameters and constraints in place to better optimize the process of continuation, we can now move on to testing the Quantum Fluctuation method with different models and verifying its ability to replicate spectra.

The following section showcases various categories of synthetic spectra that cover a representative range of Quantum Monte Carlo sampling of $G(\tau)$.

With each category of spectra comes its own challenges to modeling and continuing the noisy or incomplete correlation data that represents it. As such, the application of previously defined constraints is used when appropriate, to best optimize the spectral fit. However, a consistent systemic approach to applying the QF method is maintained throughout.

The different categories of spectra investigated are

1. Artificial geometric, without and with gap
2. BCS
3. Multiple peak Gaussian
4. Edge divergence with power-law decay
5. Gaussian with power-law decay

For each model, the spectral information is encoded onto a Heisenberg spin chain of N_ω sites using the zeta mapping as outlined in section 7.3.

An initial transverse field in the z-direction is applied at a high enough magnitude to ensure the positivity of n and maintain its normalization, yet not enough to lose important information acquired through the fluctuation of spin vectors while in the the noisy end of possible Δn values.

A few test runs are done to visually inspect the fluctuation values, making sure field operator expectation values are in the good information range, and that the spin chain is firmly entrenched between its noisy glass phase and a quenched paramagnetic phase.

After this pre-processing stage, the sequence is to first optimize β and then to optimize B^z through successive annealing processes. Except for the most trivial of cases, such as the purely contrived simple geometric spectra used as a proof of concept, each one of the samples are modeled by moving through the phase space of beta-values until one offers the lowest internal energy value.

Each step in the annealing process verifies the n values with each amplitude update, and each update results in a $\Delta\beta$ change of ± 0.5. Any step that does not maintain the positivity and normalization of n is rejected, necessary parameters are adjusted, and the step is repeated until either acceptance or the algorithm reaches a TERMINATION criteria.

The high inverse temperature value is chosen to be $\beta = 60$ for the first thermal annealing process, the change in β for each step to be .5, and the low inverse temperature to be .5, offering the opportunity to inspect the system's internal energy for a wide swath of inverse temperatures.

Because of the periodic nature of $G(\tau)$ and the connection of τ and β through the kernel K, this β range allows multiple minima that can be investigated and a series of possible slow and fast convergence rates.

In cases where there are several minima with the same approximate value, visual inspection is used to pick a best fit. The best fit occurs after a series of amplitude updates, where the absolute minimum of these updates is recorded along with its iteration number.

Once this initial thermal annealing process has completed, the process moves to the second, *quantum* annealing stage. This time, a range of inverse temperatures is taken around the initial low β value, and the $\Delta\beta$ value is set to 0.1. The annealing process is repeated, until an absolute lowest beta value is chosen with a resolution of $\delta\beta = 0.1$. This final low β value is then to be used as the optimized β.

With this optimized β, the transverse field is increased until the spin chain enters a polarized phase, at which point all spins are roughly aligned along the x-axis and the system gains no additional information.

A final optimization step is then initiated, slowly decreasing the transverse field until an optimal transverse value is obtained that minimizes the system's internal energy. The final optimal transverse field value is that which minimizes the Hamiltonian in this final step, amounting to finding the best in a family of solutions between the lowest eigenenergies of two portions of the QF Hamiltonian, which corresponds to the equivalent pure χ^2/Heisenberg part

$$H = \sum_{ij} V_{ij} \hat{n}_i^z \hat{n}_j^z - \sum_i \gamma_i^z \hat{n}_i^z + G(\tau)^2, \tag{10.1}$$

and that which corresponds to a Heisenberg system in a presence of a very strong magnetic field [37].

Note that for $E_{\min}$ values, the $G(\tau)^2$ constant is reintroduced post-DMRG to bring the ground state energy of the system as close as possible to $E = 0$.

All $E_{\min}$ values in the results are taken to be absolute values.

10.2 Semi-circle spectrum with no gap

As a proof-of-concept, a circular spectral function of radius $\omega = 1.0$, centered around $\omega = 0$, was encoded onto a system of $N_\omega = 200$ spin sites, as shown in Figure 16.

The frequency grid ran from $\omega_i = -1.0$ to $\omega_f = 1.0$, a constraint eliminating any spectral weight outside the frequency range of the true spectrum.

For this somewhat trivial test, no thermal annealing process was used. Instead, a more intuitive approach to choosing the parameters was taken to test the efficacy of the algorithm in its early stages. Most parametric magnitudes are those in the range of typical sampling of similar studies of MEM and SAC methodologies [59].

The initial primary parameters were set to $\beta = 60$ to begin the sampling process, with an applied transverse field of magnitude 7.0×10^3. A chemical potential $\mu_i^z = 80$ at each site was set to ensure an initial magnetization $M \approx 0$. The correlation function noise was set at $\sigma = 10^{-3}$, on the high side but still within the range of what would be expected with typical QMC data.

For DMRG parametrization, the maximum number of sweeps per update was 5, with the

maximum bond dimension for each sweep specified to be 10, 20, 100, 100, 400.

While completely artificial, this circular spectra proved to be an adequate test due to its actual lack of distinguishing characteristics of which to fit, beyond its inherent arc.

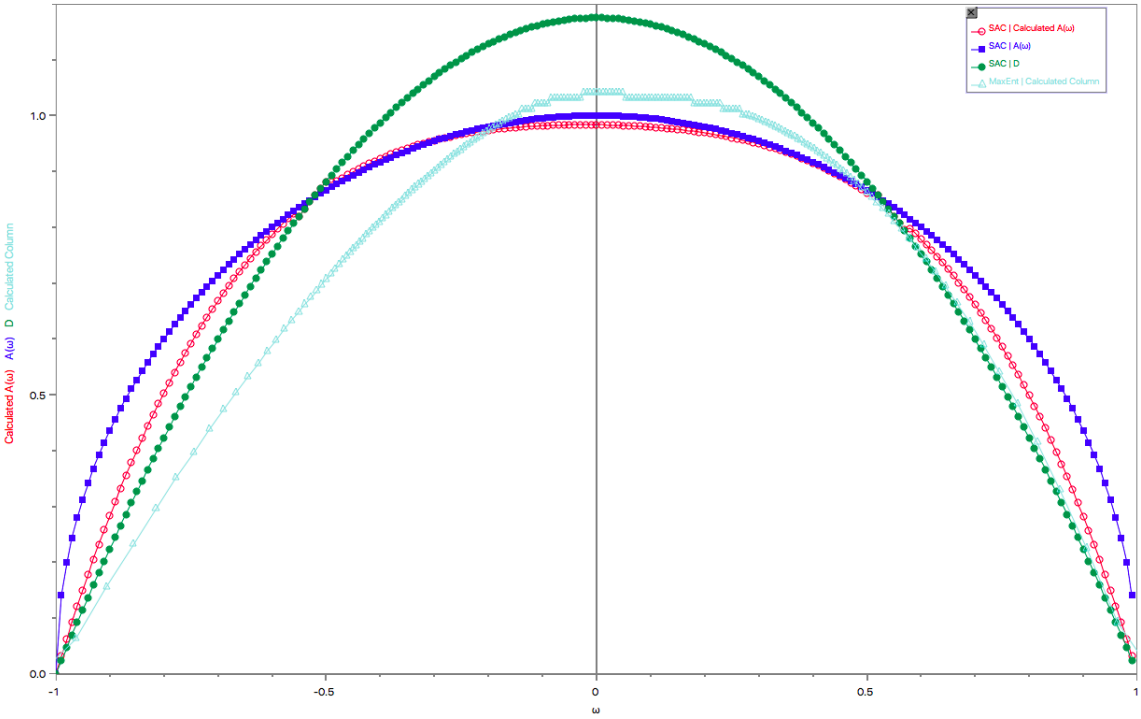

Figure 16: Semi-circle sampling without optimized parameters and narrow endpoints, with $\overline{A}$, D, and MaxEnt spectra. ($\beta = 20$, $N = 200$).

The spectrum converged to its lowest energy configuration within 12 updates of its amplitude, with $E_{\text{min}} = 7.0 \times 10^5$. The average fluctuation about $n = 1.0$ is $\Delta n = .08$, with a magnetization of -1.07. Using an parabolic default model encoded with prior information about the true spectrum's maximum amplitude, the curvature of the measured spectrum $\overline{A}$ range of frequencies around $\omega = 0$ is captured extremely well. As $\omega \rightarrow 1.0$, however, there is a divergence from the true spectrum A due to lack of sufficient fluctuation.

For this naive attempt, a number of factors was found to contribute to this behavior around the edges, first of which was the wave function's inability to maintain normalization due to the non-commuting nature of S^x. The choice of boundaries and the choice of a default model were also shown to be a limiting factors. The prior information of $D(\omega)$ in many ways worked too well for the interior of the spectrum, resulting in a overly rapid convergence in the center and a slower expansion around the outer regions.

In addition, while the choice of endpoints did restrict the leakage of spectral weight outside the boundaries $\omega = \pm 1.0$. Such behavior point to the need for less restrictive constraints with respect to the fixed ω mesh.

As observed by Sandvik, such constrained boundaries work extremely well for straight edge features, as will be seen with edge-divergent spectra, but not as well with boundaries within the vicinity of spectra without sharp characteristics [26].

When the maximum boundaries of the grid were increased slightly by .4 along each side, and the default model changed to a featureless horizontal line with integral matching that of $A(\omega)$, convergence around the outer edges of the circle greatly improved.

Learning from this naive initial test, another attempt was made, this time optimizing parameters β and B^x and reducing N_ω to 40 and subsequently increasing the discretization size to $\Delta\omega = .14$. This was done for the purpose of preventing the over-fitting of noise.

Because of the reduction of spin sites, however, it took more iterations to reach convergence, finally settling to a best solution at 21 amplitude updates.

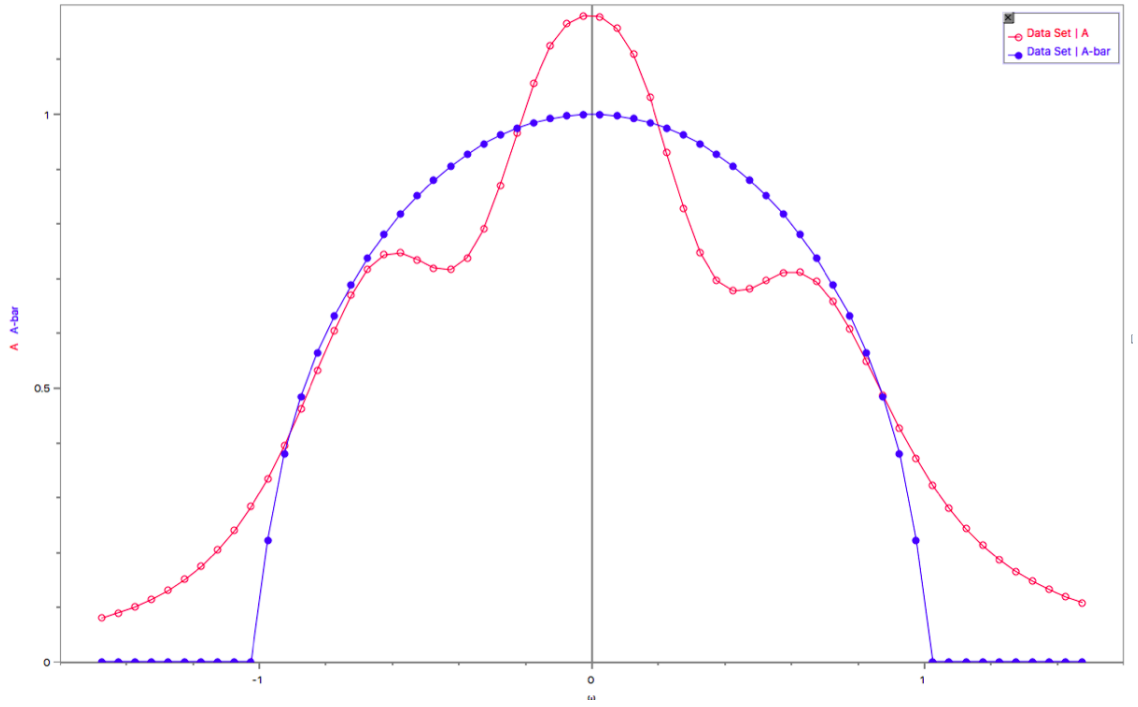

Figure 17: Semi-circle spectrum with no gap.

The spectrum shows fluctuations significantly deforming the spectrum around the edges, as needed, unlike the previous attempt. However, the spectral weight leakage comes at a price, as

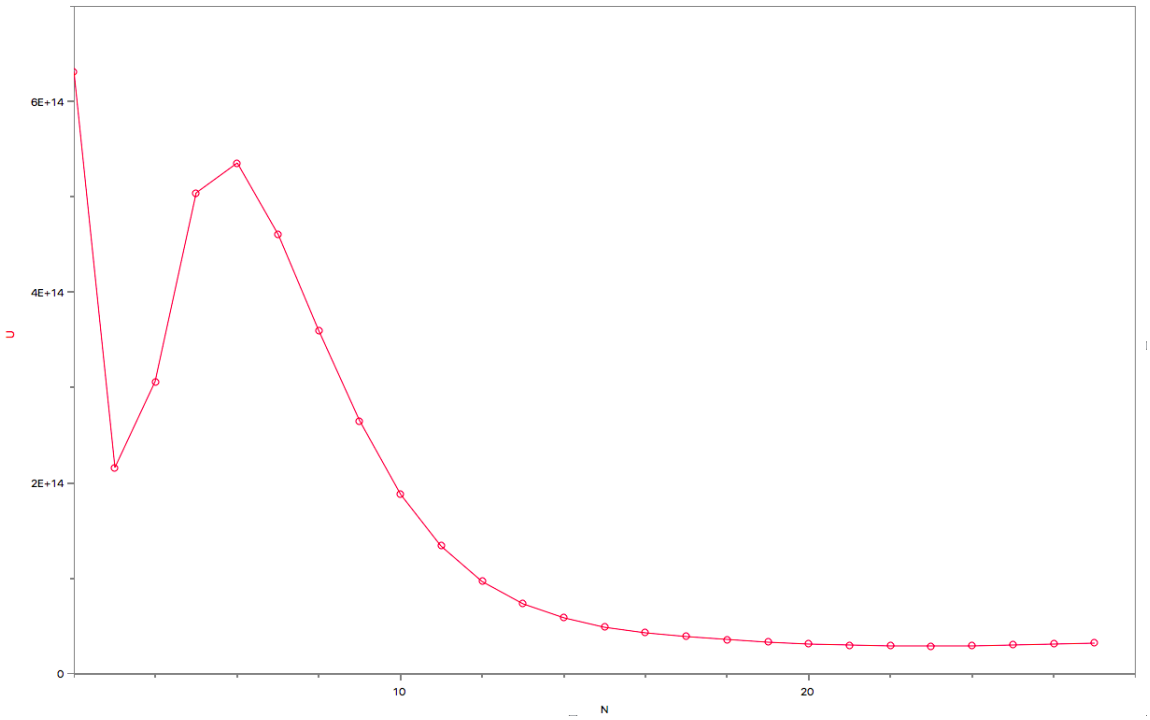

Figure 18: Energy vs update number for semi-circle spectrum showing location of optimal $\overline{A}$.

the spectrum attempts to compensate by wavering around the interior of the spectrum.

Reducing the noise to $\sigma = 10^{-5}$ improves the fit around the interior, although there is still a wavering effect surrounding the spectrum about the center due to compensation for spectral leakage on the edges.

In Figure 21, a final sample has the endpoints reduced to $\omega = \pm 1.2$. This was found to be the optimized boundaries for this inversion, resulting in a wave function with $E_{\min} = 2.2 \times 10^{13}$. Spectral leakage on the exterior of $\overline{A}$ is minimized, while also allowing enough room for fluctuations large enough to show the direction of convergence for that portion of the spectrum. The interior wavering still exists, but is minimal, and the entire spectrum takes a circular as expected.

The same $\overline{G}$ data was taken and inserted into an MEM algorithm. The QF method shows superior convergence of the interior of the spectrum and matches the MEM on the edges leading to the endpoints. For the endpoints, the MEM required the use of a larger portion of the ω grid to reach its best convergence, compared to the optimized cut-off points of the QF method.

In all, this series of tests proved successful, showing the quantum fluctuation method capable

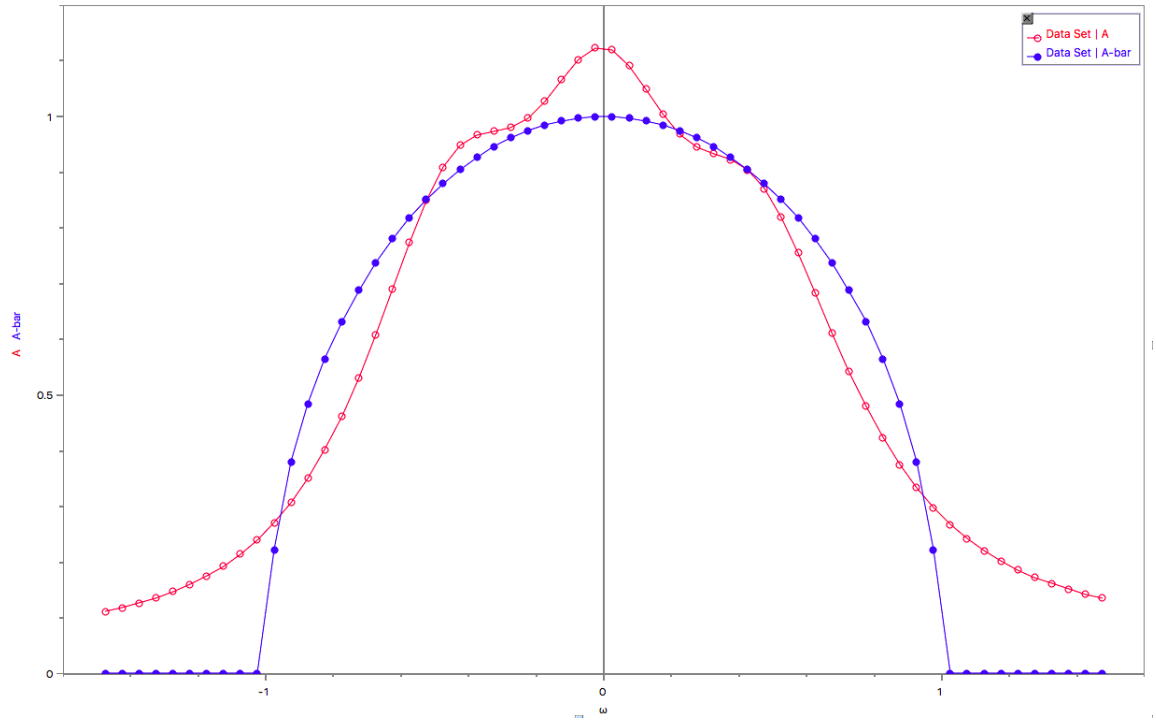

Figure 19: Semi-circle spectrum with reduced noise.

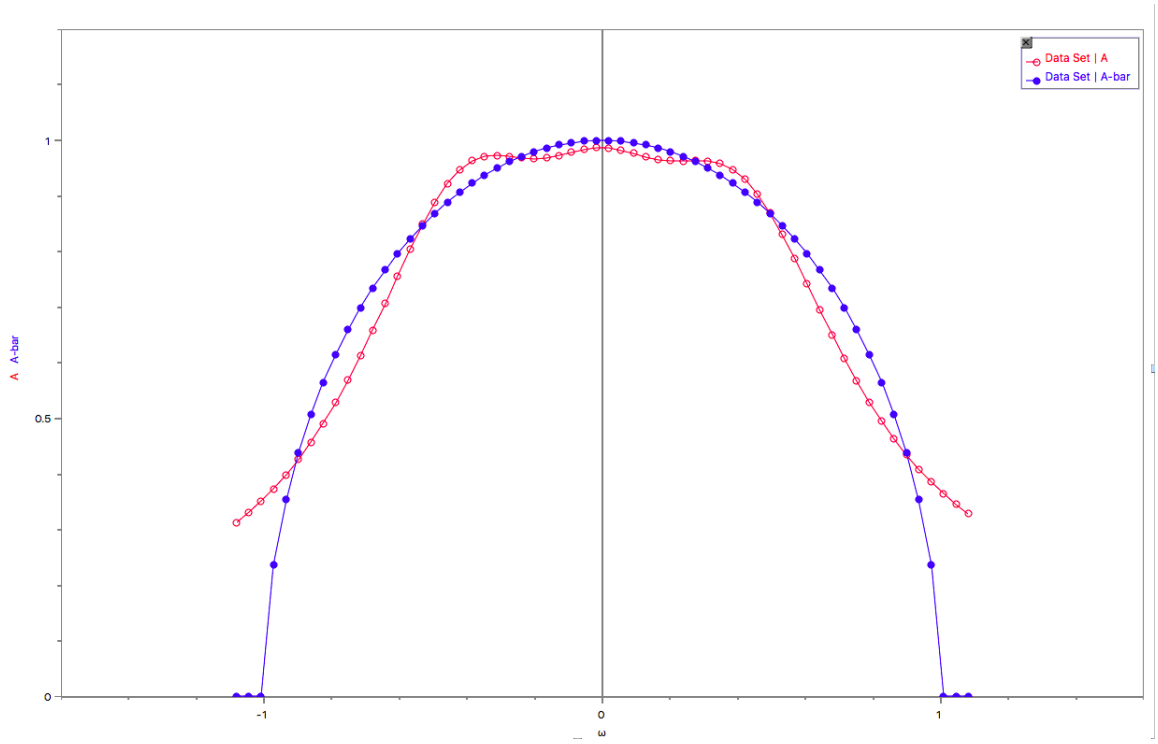

Figure 20: Semi-circle spectrum with endpoint optimization at ±1.2.

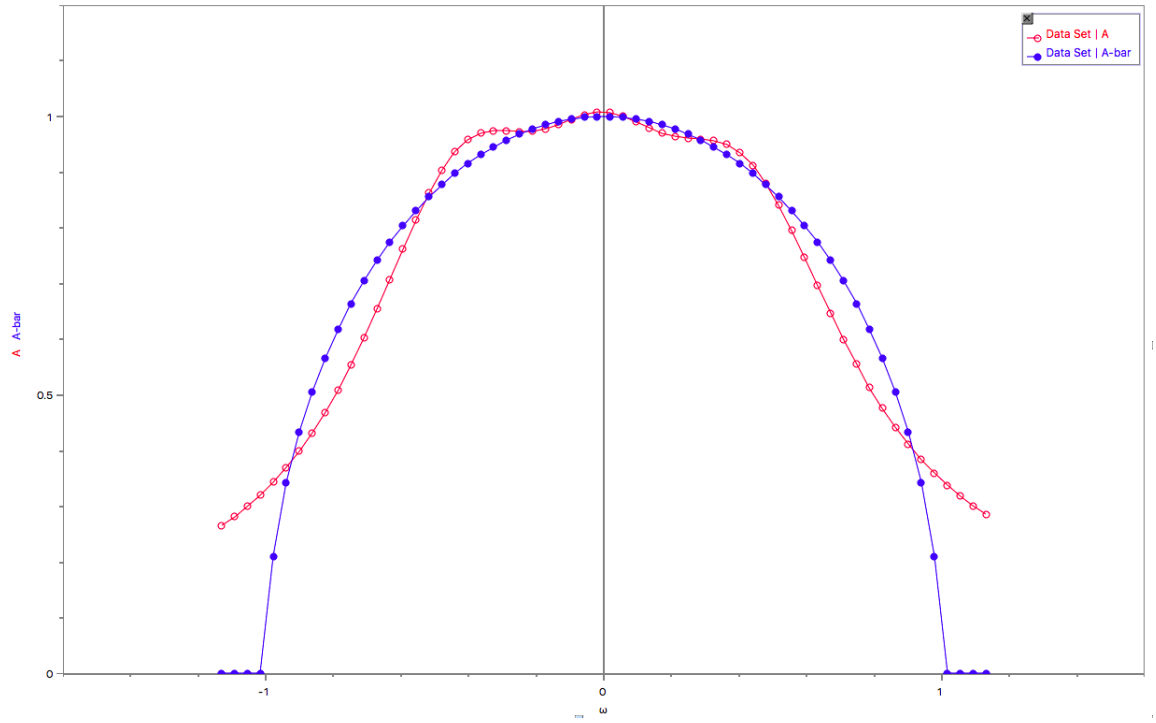

Figure 21: Semi-circle spectrum with endpoint and transverse field optimization. $\overline{A}$ shows minor wavering near the center of the spectrum but good convergence.

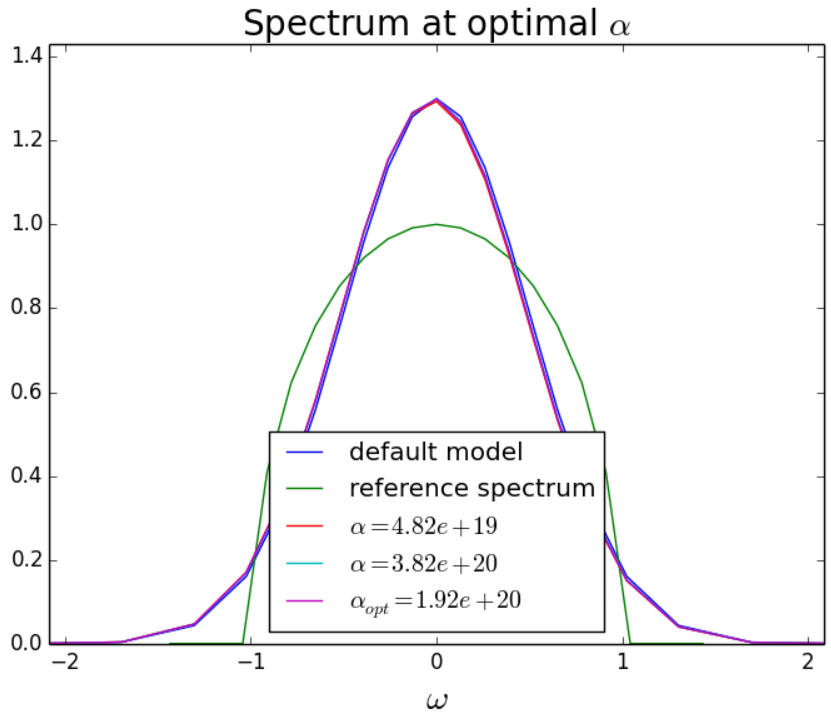

Figure 22: MEM fit with $N_\omega = 200$ for semi circle with radius $\omega = 1.0$ [25].

of sampling noisy imaginary data and extracting real spectral information. Possible weaknesses discovered were endpoint fidelity in the absence of an optimized ω mesh and the necessity of an increased number of amplitude updates to reach a convergence when N_ω is decreased.

Further circular tests were performed, showing the QF capable of faithfully reproducing spectrum with increasing $m = A(\omega)d\omega$, although there appears to be a limit around $m = 7$ before efficiency decreased.

10.3 Semi-circle spectrum with a gap

The second synthetic spectra to be sampled was another circular geometric model with features similar to the first. But in addition, a gap was added of width of $\Delta\omega = .5$.

This feature serves as a precursor to other important spectra which give information about gapped energy states. Just as with the initial synthetic circular spectrum, a naive test was first performed without B^x and β optimization, shown in Figure 23.

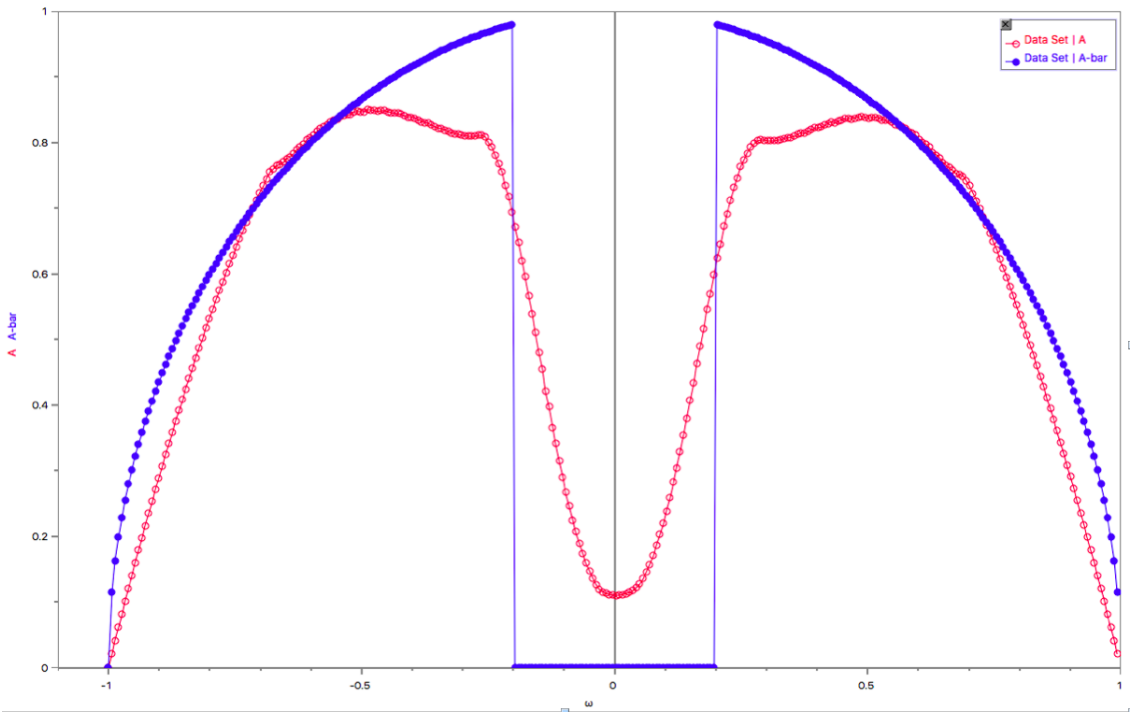

Figure 23: Gapped semi circle spectrum without optimization, and gap of width $\Delta\omega = .5$ and a circular radius of $\omega = 1.0$.

With this first test, the gapped spectrum was created by a circular arc of radius $\omega = 1.0$ centered at $\omega = 0$. Its fixed frequency grid extends through $\omega = \pm 1.0$, preventing any spectral

leakage outside of the semi-circle's boundaries.

The gap of the true spectrum is pronounced, in effect a steep drop at its frequency limits with no additional features to model. It is a completely artificial scenario, but one that serves as a proper test for the handling of such a feature by the QF algorithm.

The correlation function $G(\tau)$ is composed of 20 imaginary time points. Using the correlator's initial value $G(0)$, the noise is set to be at a level $\sigma = 10^{-5} * G(0)$. With $N_\omega = 301$ spin sites, the model sufficiently captures the width of the gap, although there is distortion of the width and the depth of the gap is not completely captured.

The edges of the gap are rounded to a height of approximately .8 for the gap, a result of the loss of spectral weight around the edges of the circle and the inadequate fluctuations of n near the outer edges of the frequency grid. It took 102 amplitude updates of the model to find the lowest energy match $E_{\min} = 4.4 \times 10^{13}$, with an average fluctuation per site of $\Delta n = 0.11$.

The test showed successful fidelity to the original spectrum $A(\omega)$, but clearly with room for further optimization.

For the next step, a similar approach was taken as with the original no-gap circular spectrum. Reducing $N(\omega)$ to 63 and optimizing β and B^x served to improve the fit between A and $\overline{A}$.

For the first stage of thermal annealing, a field value of $B^x = 9.0{\times}10^{15}$ was held constant until an optimal inverse temperature of $\beta = 44.5$ was reached. From there, the transverse field was optimized to $B^x = 1.6 \times 10^{16}$, with the state settling to a minimum energy of $E_{\min} = 4.4 \times 10^6$.

The $\Delta\omega$ gap is evident, although there is deviation about the maximum of the gap in comparison to the true value of $A = 1.0$. Capturing the curvature of the semi-circle proves difficult, although the variation is limited and is clearly effected by $\overline{A}$ tapering off with positive spectral weight outside the semi-circle's boundaries. Further optimizing the grid endpoints improved the fit, especially around the right side of the curvature.

As an additional test, the gap was then decreased by half to $\Delta\omega = 0.25$, as seen in Figure 31. The reduced gap width proved to be a more difficult problem, requiring more regularization by an increased transverse field in order to capture the distinguishing characteristics in such a small spacing without over-fitting the noise in that region.

Setting the transverse field to an initial $B^x = 5.0 \times 10^{19}$ to ensure the positivity of $n(\omega)$, the

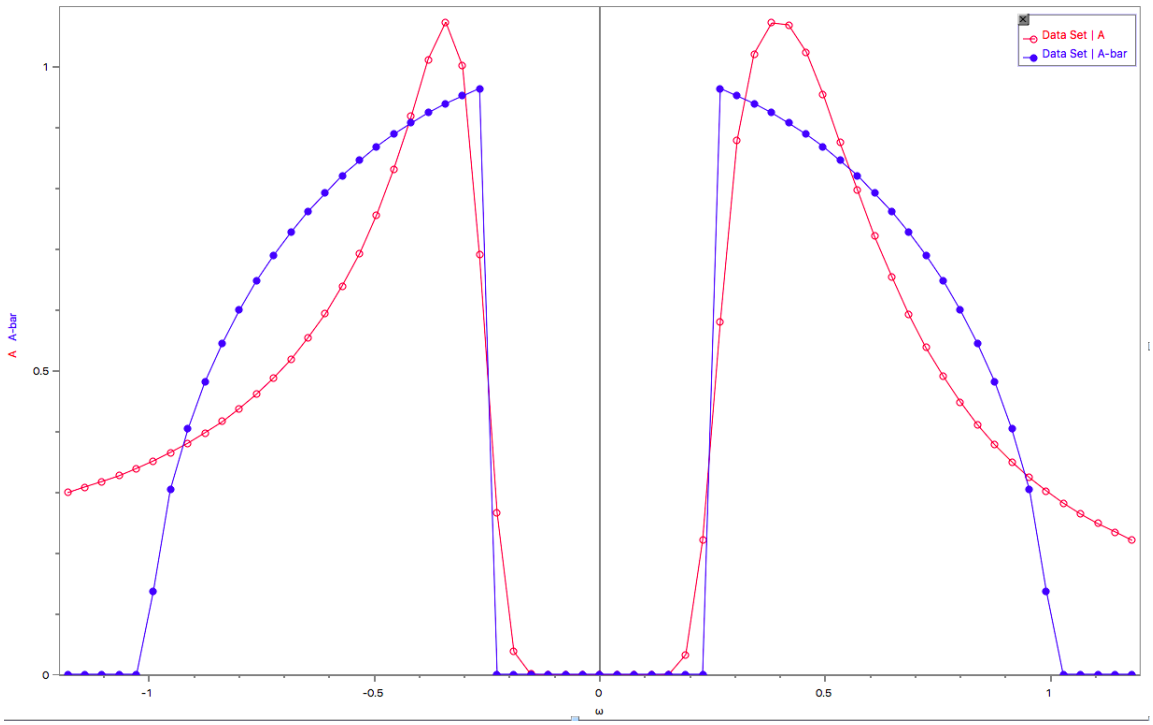

Figure 24: Gapped semi-circle spectrum with 10^{-5} noise, a gap width of $\omega = 0.5$, and a spectrum width of $\omega = 1.0$.

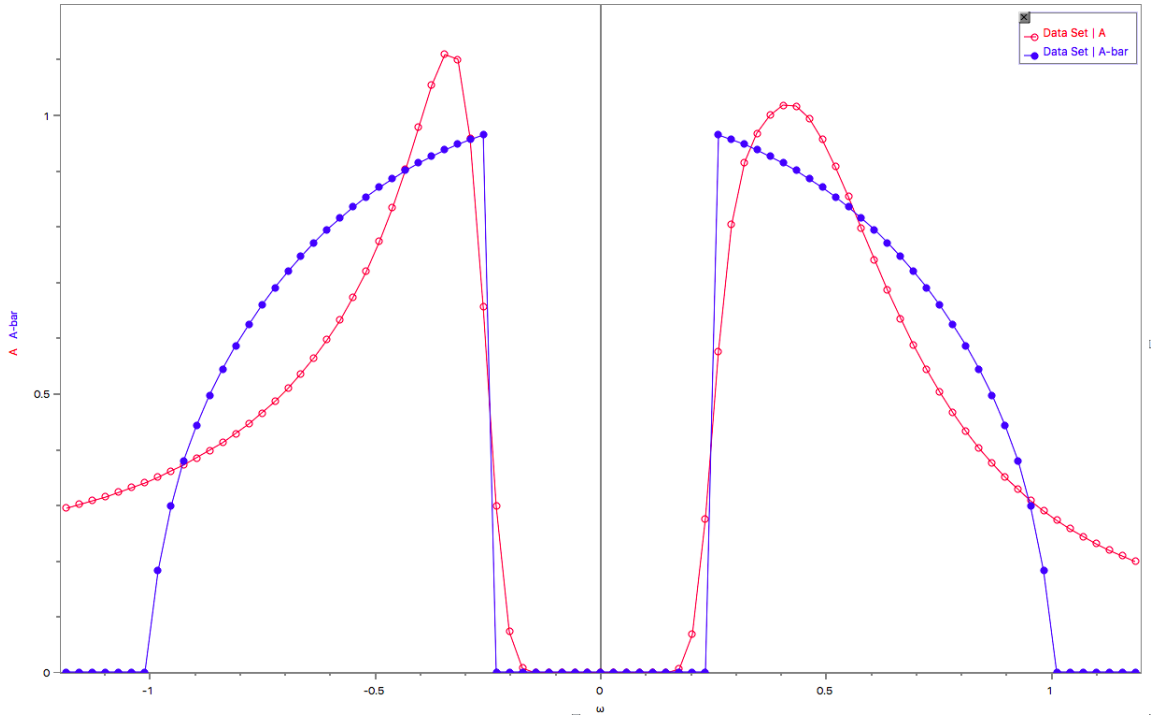

Figure 25: Gapped semi-circle spectrum with optimized endpoints at approximately ±1.6 compared to the previous values of ±1.4, allowing the release of spectral weight around the edges.

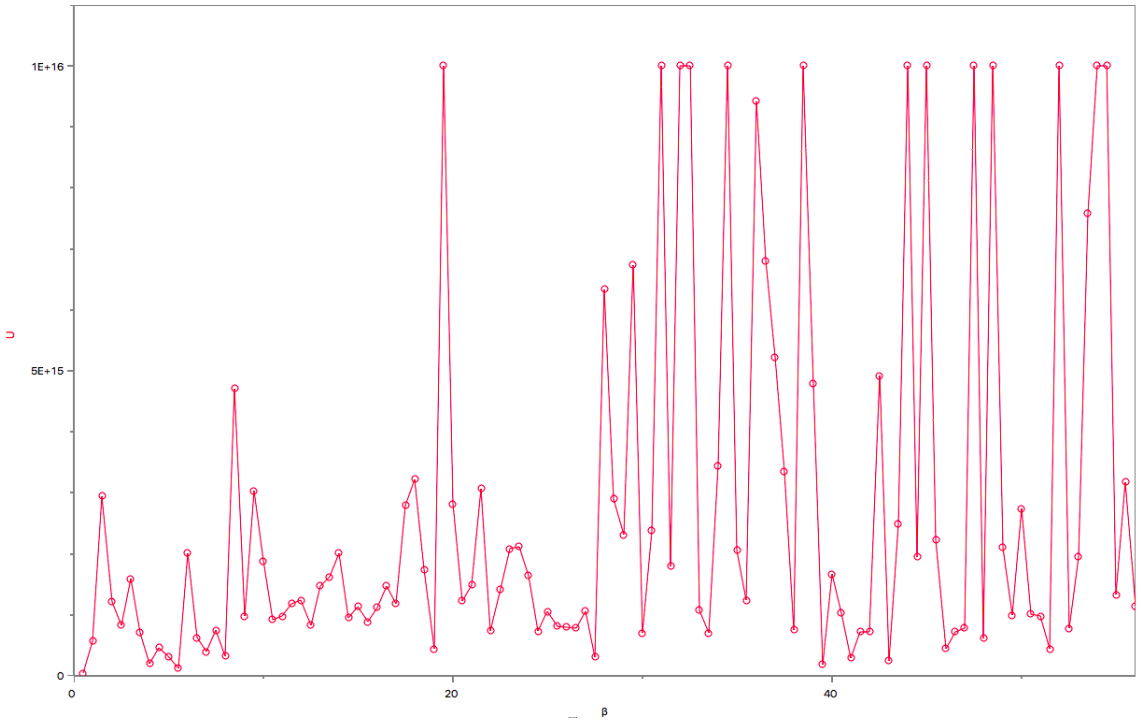

Figure 26: Thermal annealing of gapped semi-circle spectrum. Vertical axes is internal energy U and horizontal axis is inverse temperature β. Energy values of 1×10^{16} values denote inverse temperatures samples with early terminations due to negative spectral weight.

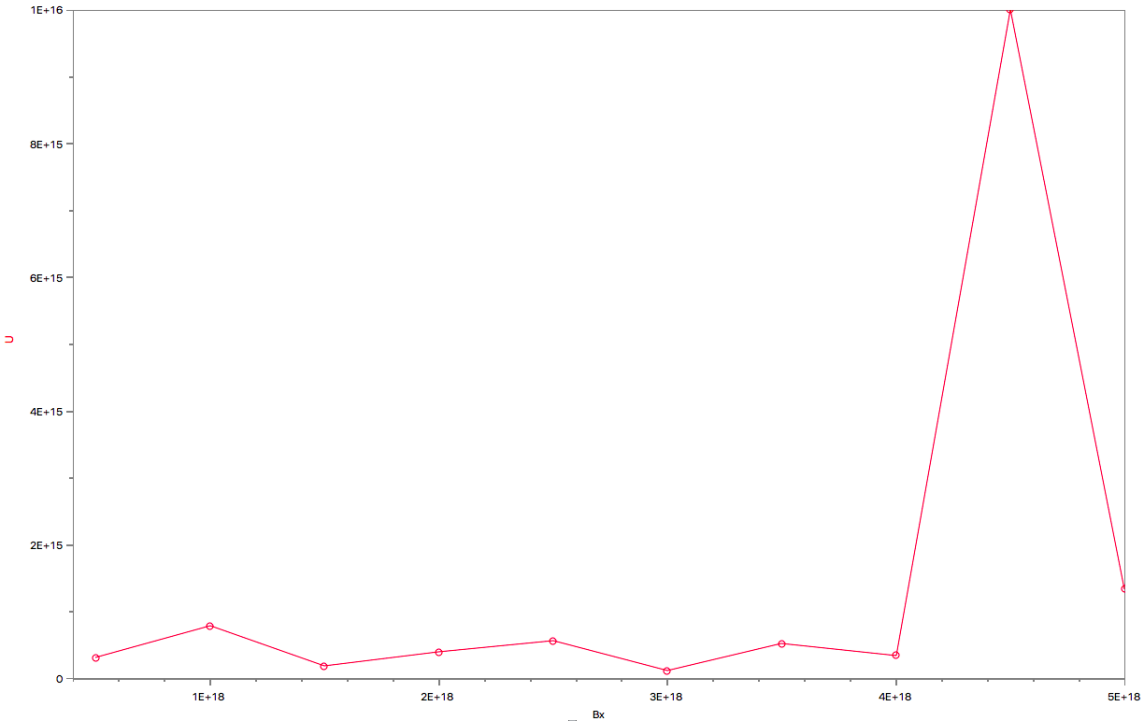

Figure 27: Quantum annealing of gapped semi-circle spectrum. Vertical axis is internal energy U and horizontal axis is B^x.

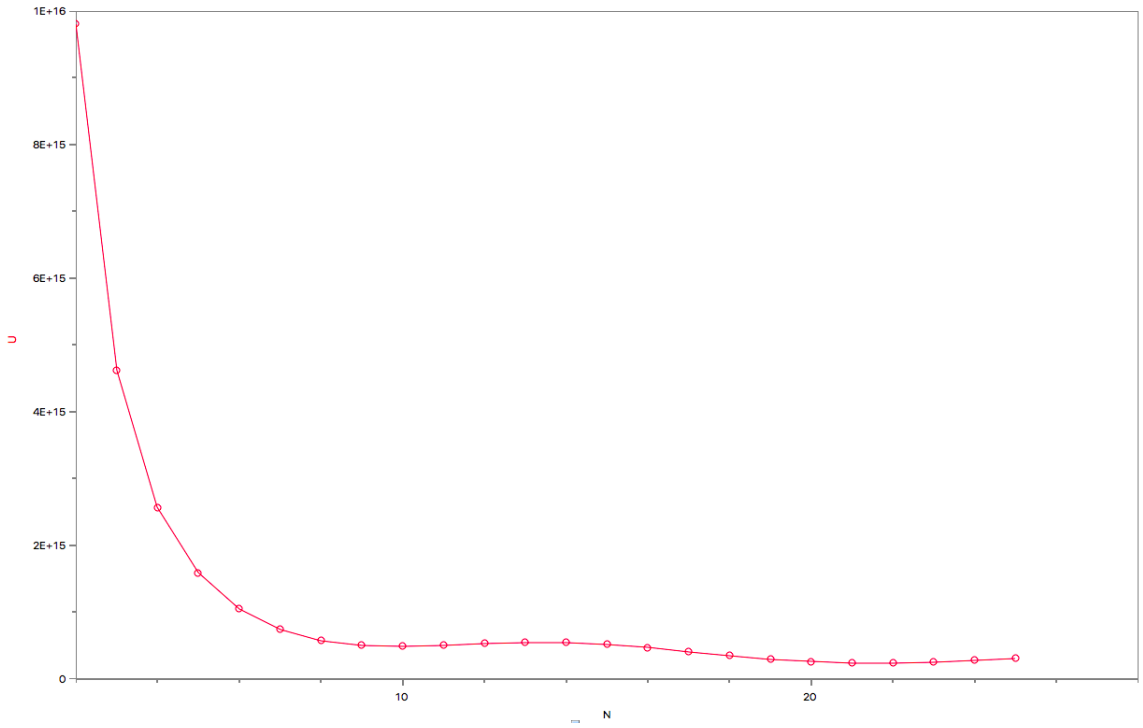

Figure 28: Internal energy vs update number profile used to identify the best fit spectrum at optimized β and transverse field values.

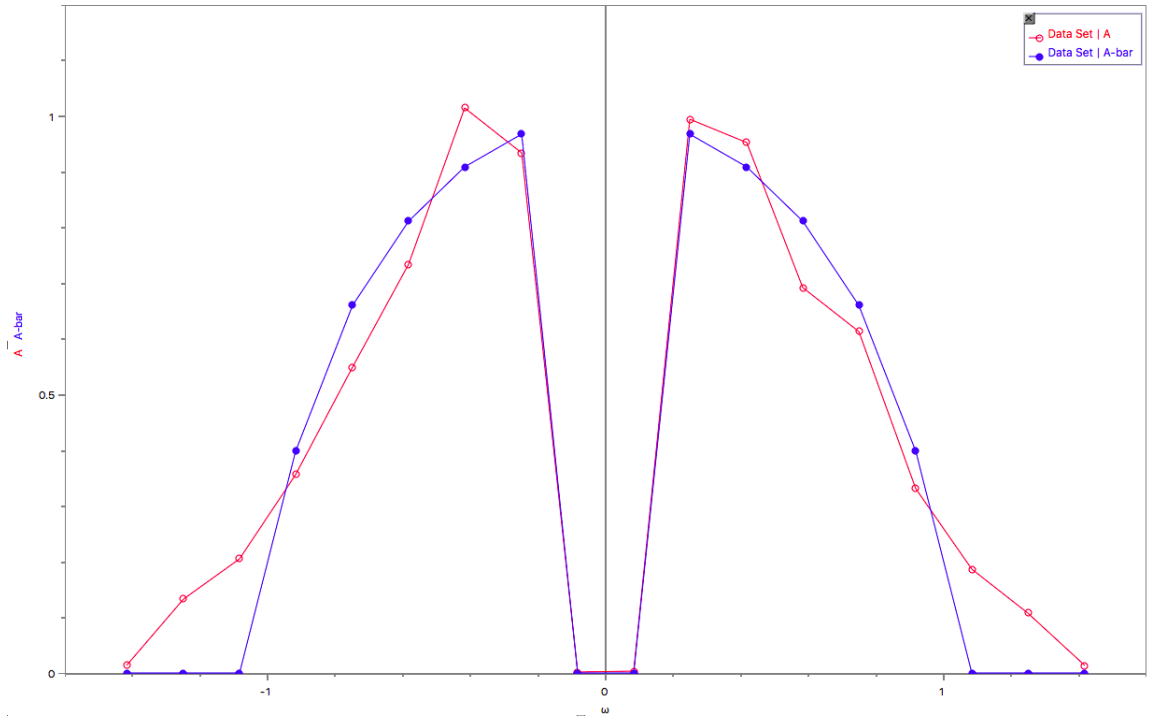

Figure 29: Reduced gap semi-circle spectrum with width $\Delta\omega = .25$.

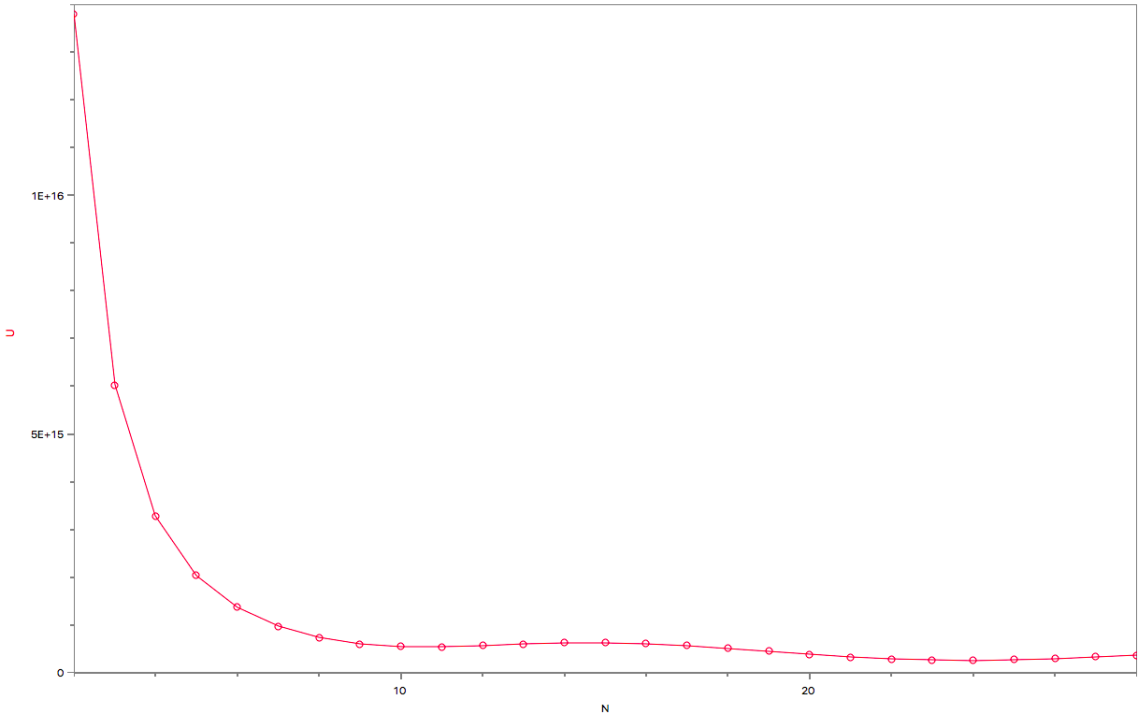

Figure 30: Internal energy vs update number profile for reduced gap semi-circle spectrum.

thermal and quantum annealing processes were repeated, resulting in optimized β value of 24.4 and final transverse field of 6.2×10^{19}.

Once again, the gap is easily distinguished, showing its proper width. The fitting is narrower around the edges, tapering off around the spectral boundaries with an approximate $\Delta\omega = 0.3$ gap along both sides of the true spectrum.

The overall height of $\overline{A}$ at the gap's edges ends up being 0.9 and 1.02, for left and right sides of the gap respectively, compared to the true height of 1.0 of A, but overall the spectrum is recognizable and its distinguishing features remain intact.

10.4 BCS spectrum

The BCS theory tackles superconductivity at a microscopic level by describing superconductivity as an effect caused by the condensation of Cooper pairs of electrons near the Fermi level due to a slight attraction stemming from a potential difference.

This electron pairing results in a small energy gap of the order of $\Delta\omega = 0.001\,\text{eV}$, which inhibits the type of collision behavior that is seen in ordinary resistors [12].

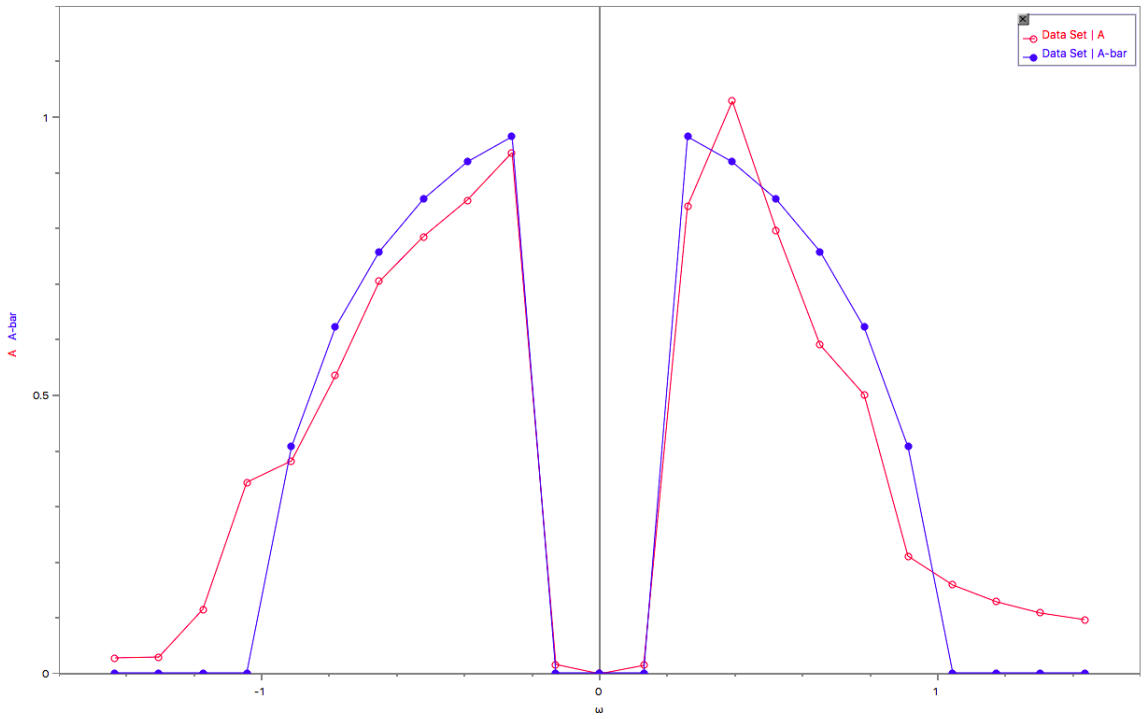

Figure 31: Reduced gap semi-circle spectrum with width $\Delta\omega = 0.25$ and reduced noise

The experimental verification of such a gap is one of the key pieces to the veracity of the BCS theory. A typical BCS spectral problem involves the extraction of fitting parameters in eV from tunneling spectra acquired on Nb- and N-doped Nb, using such techniques such as tunneling microscopy (STM), tunneling spectroscopy (STS), and x-ray photoelectron spectroscopy (XPS) [43, 49].

Information about the effects of this doping on the conductivity, pairing interaction strength of Cooper pairs, and surface resistance of material can aid in the design of more efficient electronic components and superconducting RF cavities for next-generation particle accelerators [13].

An example of the type of spectra one can expect to see with with such a model is shown below. Note the gap of width $\Delta\omega = 0.5$, along with the sharp edge of the gap and the tapering until it reaches a plateau of approximate height $A = 1.7$ and width $\omega = 1.5$, at which point there is a steep drop.

This synthetic spectrum was produced by

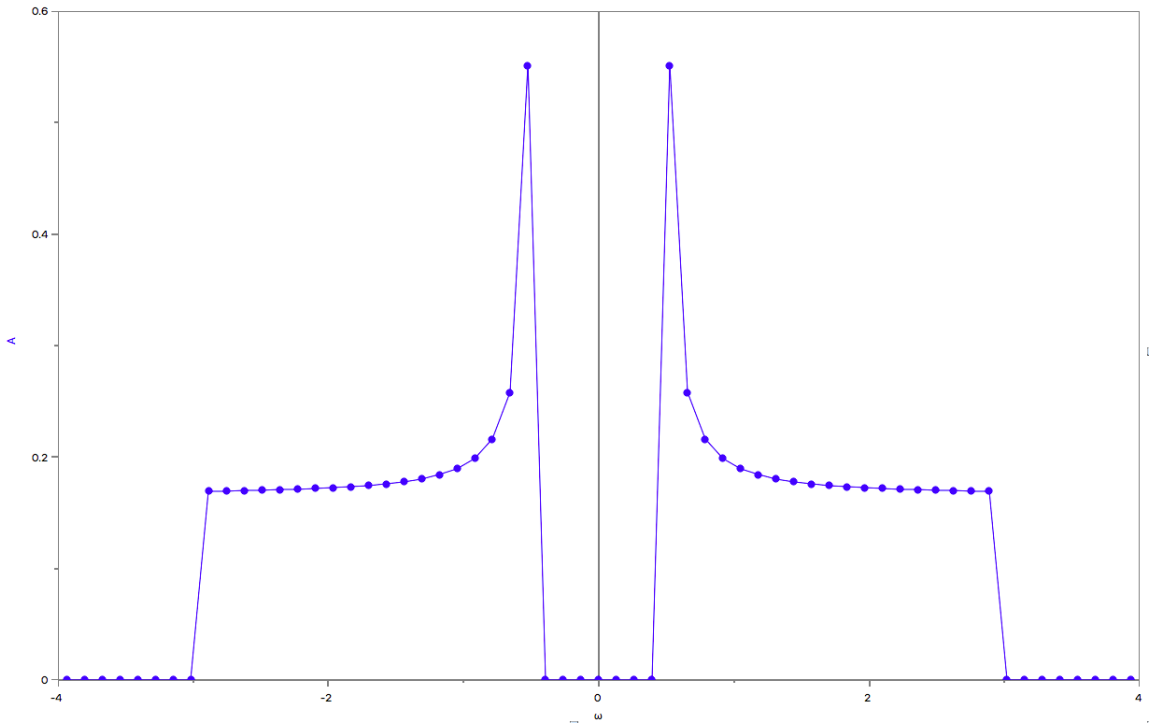

Figure 32: Example BCS spectrum.

$$A(\omega) = \frac{1}{W} \frac{|\omega|}{|\omega^2 - \Delta^2|} \tag{10.2}$$

for $\Delta < |\omega| < W/2$ and zero everywhere else, where W is the spectral width and Δ the gap width.

Such a spectrum requires a good deal of regularization of data to capture not only the gap width, but to obtain as much information as possible about the adjacent peak and to adequately capture the leveling arc.

An early attempt proved somewhat successful, showing the QF method's ability to properly capture the edges of the gap and to distinguish the sharp edges around it, unlike the MEM trial which smoothed the peak. However, the outside edges were unable to properly replicate the true model's outer edge, instead decaying in a manner similar to the MEM.

Subsequent tests proved more successful. Utilizing ITensor's native parameters, the maximum bond dimension of the DMRG calculation was increased to 10, 20, 400, 800, 1200, 1500, 1600, the cutoff noise to 10^{-10}, and the number of sweeps from 5 to 7.

An annealing process resulted in a optimized inverse temperature of $\beta = 20.1$ with $N_\tau = 30$,

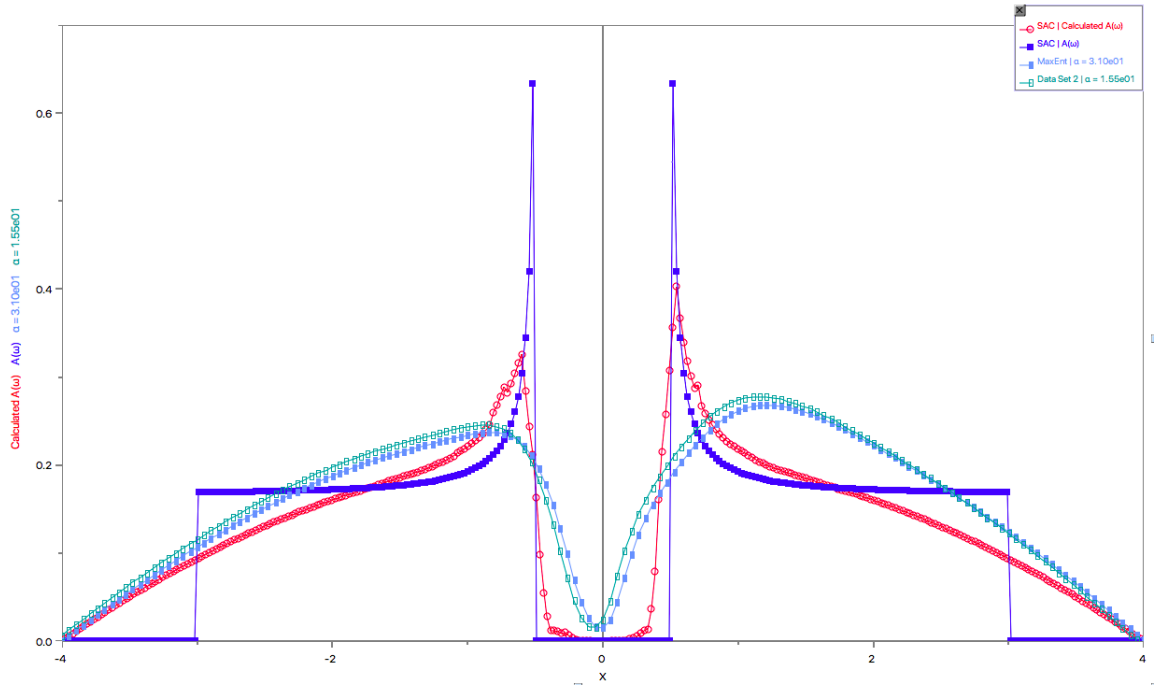

Figure 33: BCS naive attempt with $\overline{A}$, MaxEnt, and true spectrum ($\beta = 20$, $N = 300$).

and transverse field of $B^x = 8.0 \times 10^5$. The minimized energy for the best fit was 3.6×10^5.

Once again $\overline{A}$ properly conveys the gap between $\omega = \pm 0.25$. In addition, the peaks at the edges clearly pronounced, showing maximum amplitudes of approximately 0.45 and 0.40 compared to the true spectrum's 0.55 maximum.

This time, however, the decay from the max levels off to better match that of the true spectrum's plateau, although there is slight divergence along the right edge. The outer edge of the spectrum is also better defined, with $\overline{A}$ tapering off near $\omega = 2.0$ on both sides, although the true spectrum experiences a drop off at approximately $\omega = 3.0$. The number of amplitude updates to reach $\overline{A}$ was 155, with $N_\omega = 61$ spin sites and $N_\tau = 30$ time points. The amount of noise added to $G(\tau)$ was $\sigma = 10^{-5}$.

Keeping β constant, but increasing the noise by a factor of 10, resulted in another satisfactory fit, although there is a noticeable wavering effect along the left plateau.

Keeping β constant, but decreasing the number of ω points to $N_\omega = 26$, is shown in Figure 37. With the reduction of spin sites came the necessity to increase the transverse field to $B^x = 8.0 \times 10^6$ to compensate for the increased level of fluctuations at each site. The plateau adjacent to each peak is better matched, and so is the overall width of the spectrum.

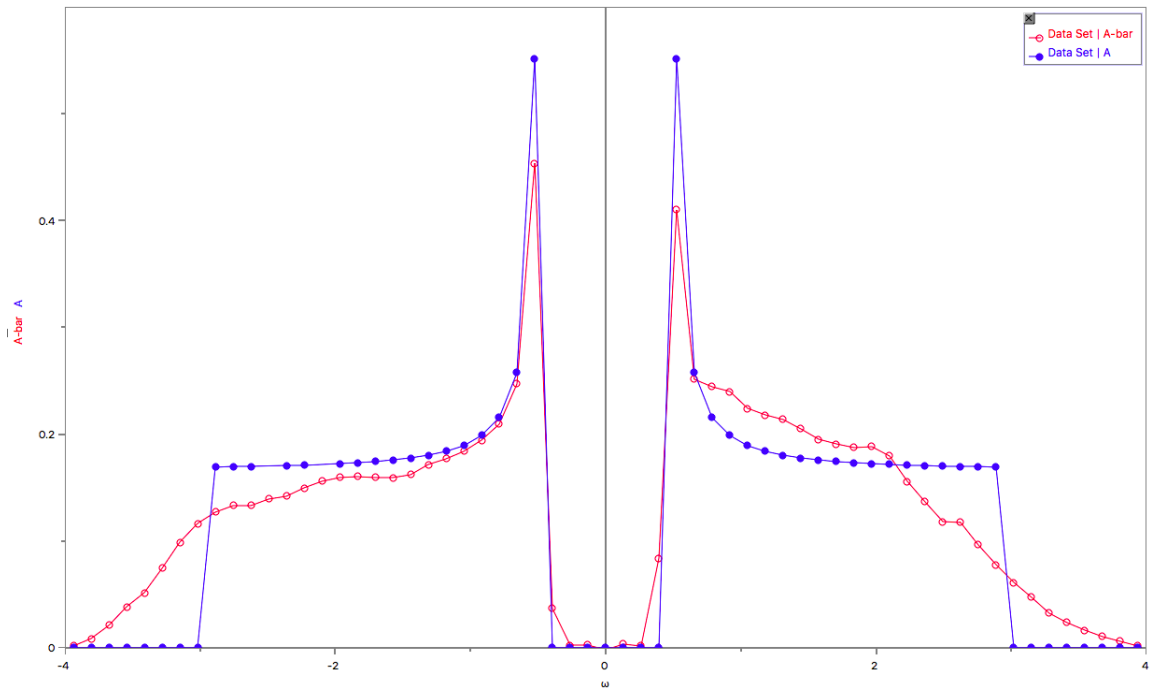

Figure 34: BCS spectrum on a fixed ω grid of $N_\omega = 62$, with a transverse field $B^x = 8.0 \times 10^5$. Gap and width features of the BCS are captured and $\overline{A}$ shows fidelity with the true spectrum.

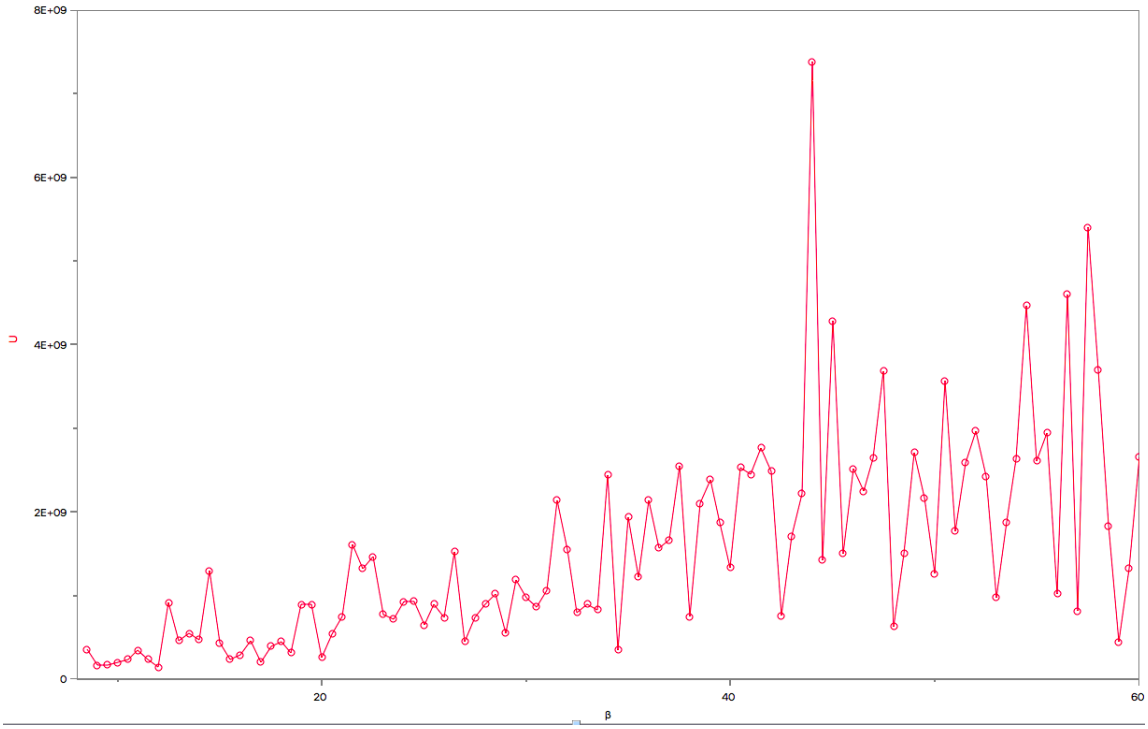

Figure 35: BCS thermal annealing profile, showing a minimized energy of the Heisenberg chain occurring at $\beta = 20.1$.

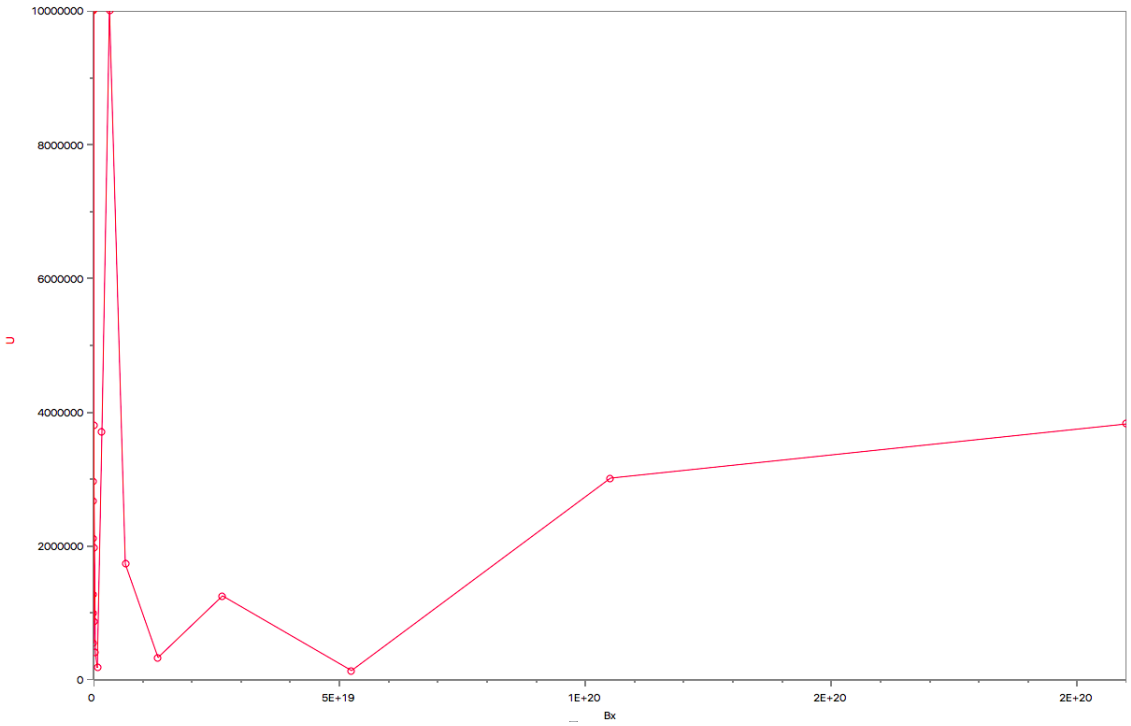

Figure 36: BCS quantum annealing profile, showing a minimized energy of the Heisenberg chain occurring at $B^x = 8.0 \times 10^5$.

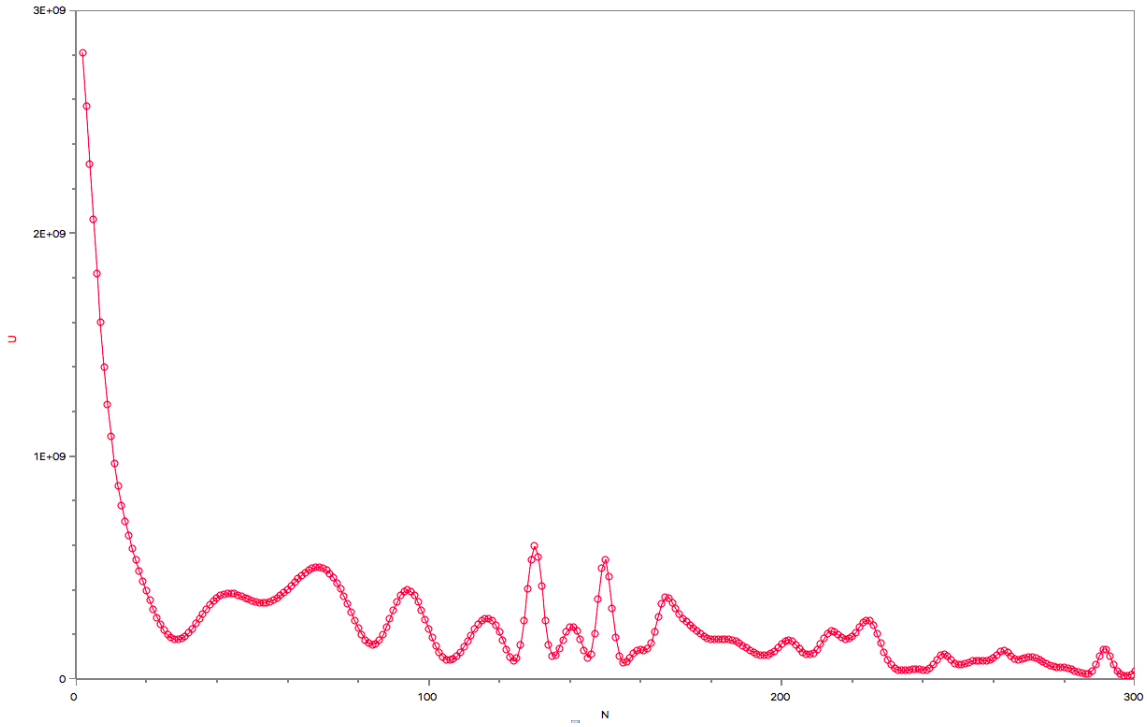

Figure 37: Internal energy vs update number profile for BCS spectrum.

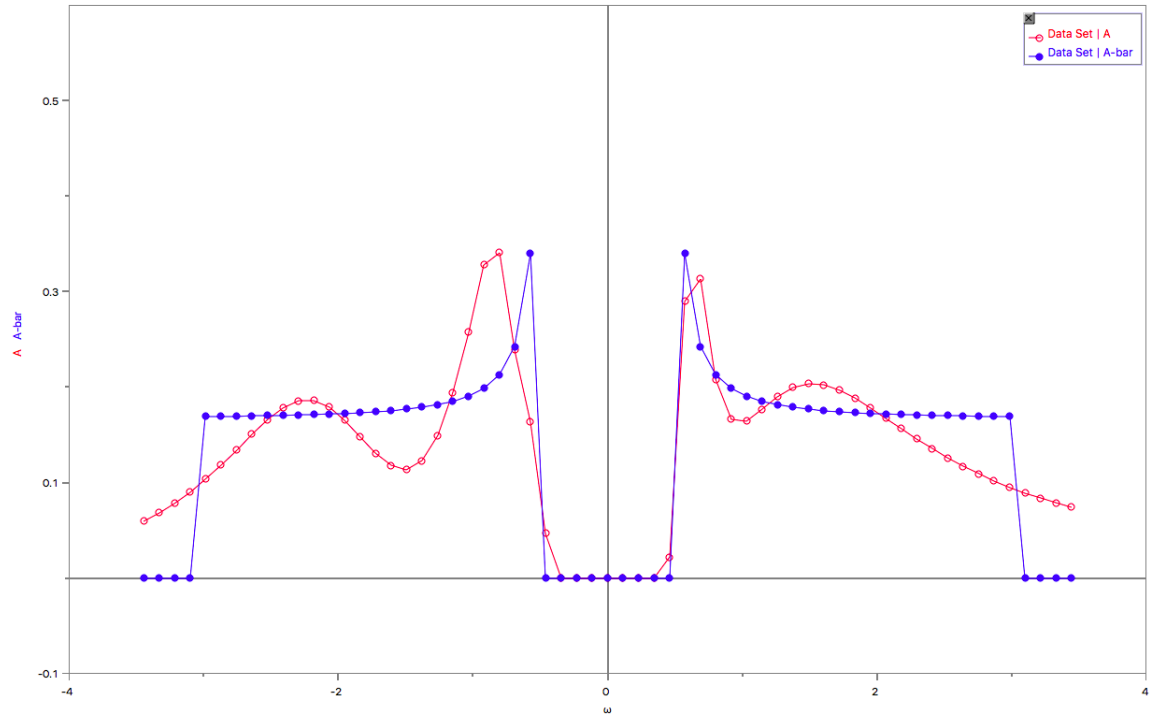

Figure 38: BCS spectrum with $N_\omega = 60$ and increased noise level of 10^{-4}, resulting in captured peaks but distortion along left side of spectrum.

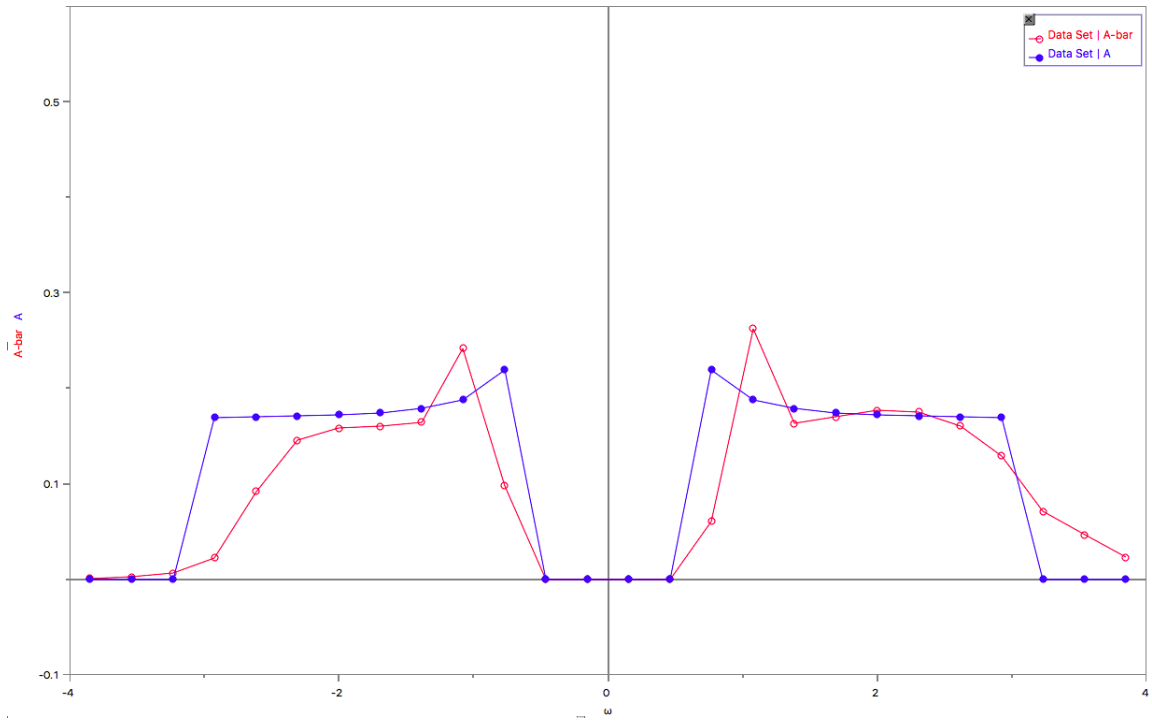

Figure 39: BCS spectral function with $N_\omega = 26$ spin sites. There is good capture of the plateau and the overall spectrum width, although the peak width is slightly distorted.

A more challenging problem occurs with the reduction of the gap by half.

Keeping the number of spin sites at $N_\omega = 61$, the optimized beta and transverse field parameters were 34.5 and 5.0×10^{10}, respectively. The increase in B^x proved necessary to regularize the increased noise of the system and variance of the fit.

The minimized energy of the system is $E_{\text{min}} = 6.1 \times 10^6$.

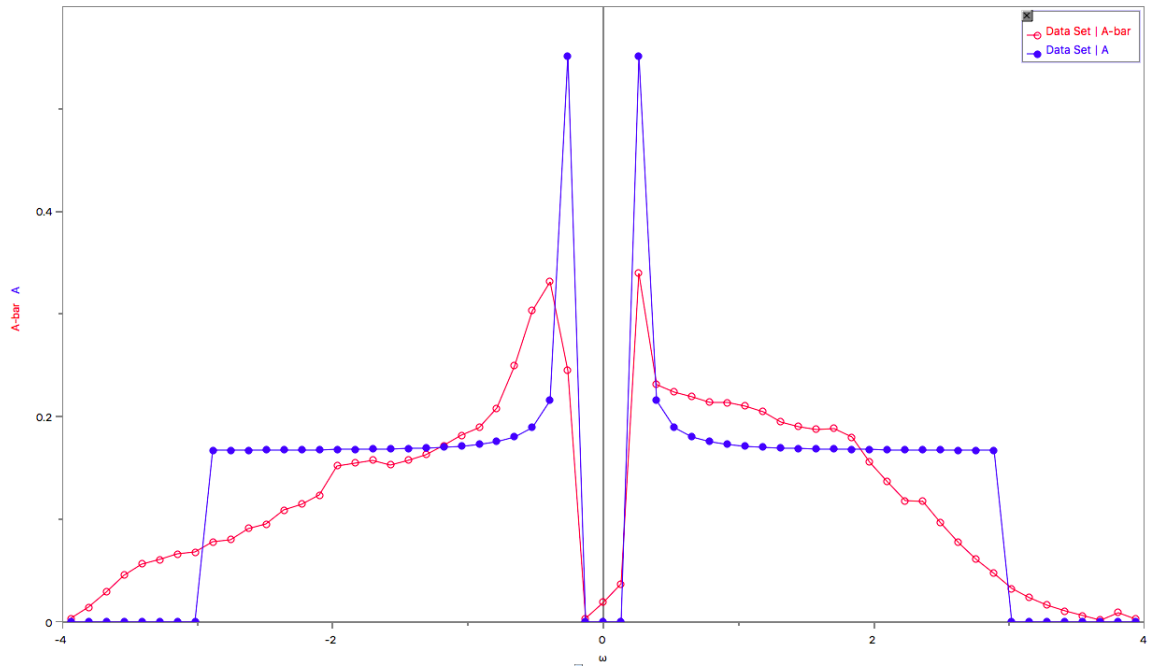

Figure 40: BCS spectrum with $N_\omega = 60$ and a reduced gap.

As seen in the semi-circle case, the reduced gap introduces error around the gap edges. While the width of the gap is still accurate, there is the depth of it is only partially captured on its positive frequency side.

Similarly, an slight asymmetry can be seen along the gap peaks. While the true spectrum peaks at 0.55, $\overline{A}$ peaks at 0.33 on the left side and 0.34 on the right, a minor variance but a noticeable one.

The more pronounced effect of noise is even ore observable as one moves away from $\overline{A}$'s peaks. The left peak of the spectrum is shifted to the left, and the curvature along its plateau is jagged and uneven. Along the right side, the peak's location is much more accurate, but the plateau misses slightly from above. Both endpoints taper to zero, but the left side is much steeper along the spectrum's most outer edge. Further increasing the number of time points did

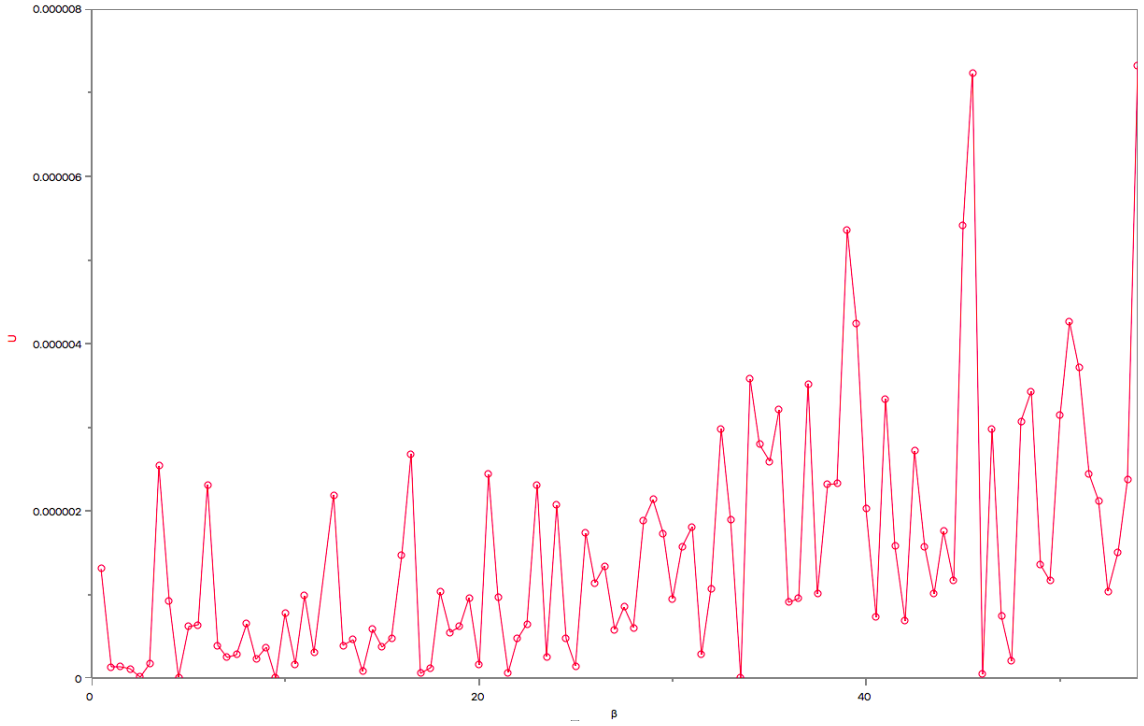

Figure 41: Thermal annealing profile of BCS spectrum with reduced gap, resulting in $\beta = 21.5$.

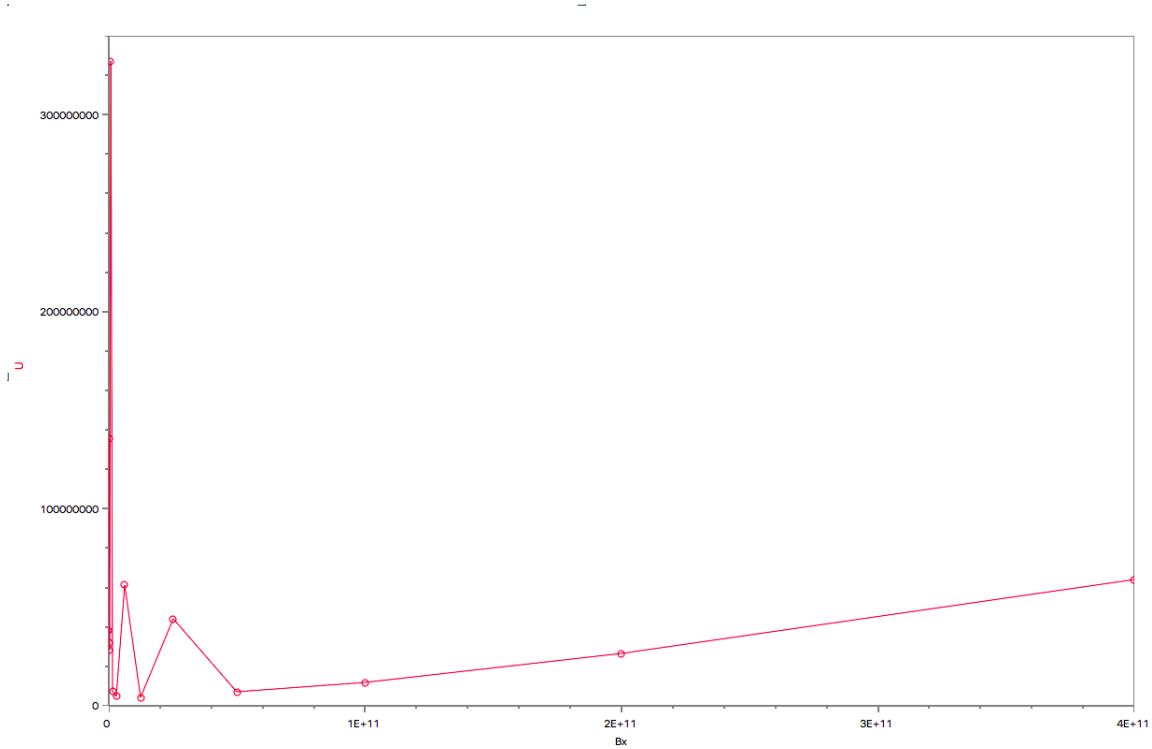

Figure 42: Quantum annealing profile of BCS spectrum with reduced gap, resulting in $B^x = 4.0 \times 10^{10}$.

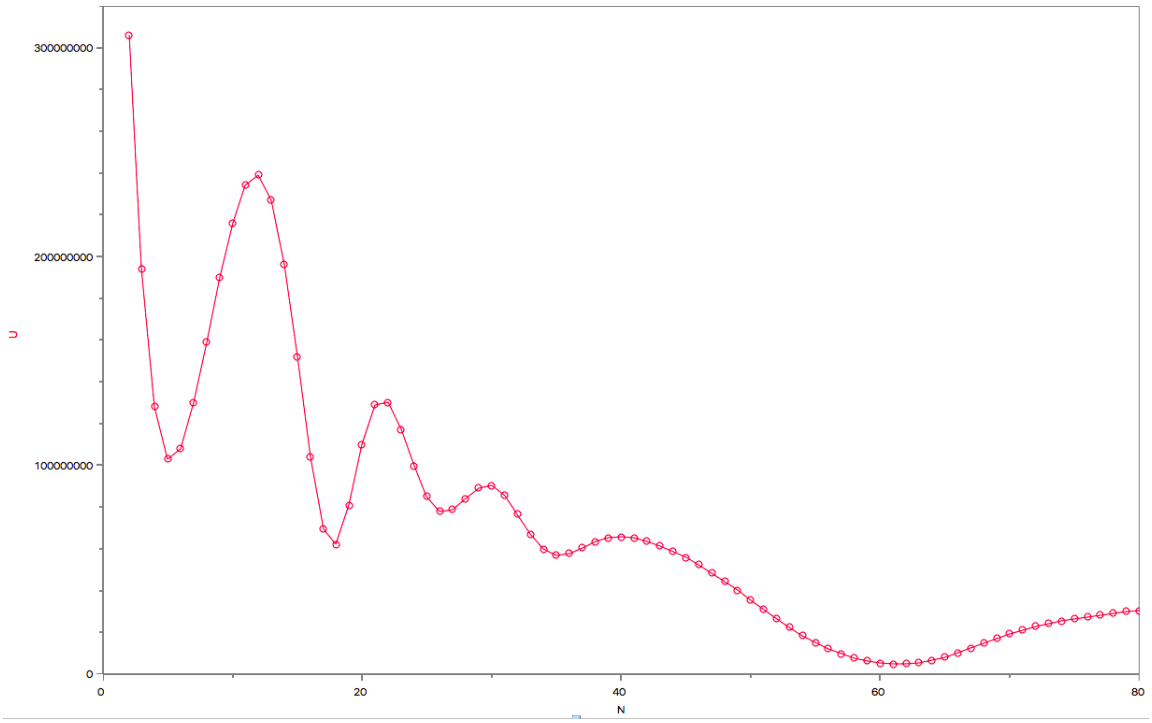

Figure 43: Internal energy vs iteration number profile for BCS spectrum with reduced gap. After 61 updates, the system reaches its lowest energy.

not significantly improve $\overline{A}$, nor did increasing the transverse field beyond the optimized range of B^x.

Figure 44 shows the effect of increasing the transverse field past the quantum critical region, in addition to decreasing the noise level by a factor of 10 to $\omega = 10^{-4}$ and increasing the maximum bond dimension per sweep to aid in convergence.

In this case, the minimum energy of the system was $E_{\text{min}} = 8.5 \times 10^5$, with the average spin fluctuation of approximately $\Delta n = 0.13$. Once again, the dimensions of the gap are clear, but the increased field smooths much of the desired features from the positive frequency side of $\overline{A}$.

This proved to be a common occurrence when trying to improve optimized spectra by increasing the field. Once the quantum critical region is found, further increasing the field smears out distinguishable features of the spectra due to the decreased fluctuations of the spin, decreased gapping of energy levels, and subsequent loss of information.

A third test exhibited what I believe to be the most interesting results for further study, even with the presence of wavering effects around the perimeter. In this case, the number of spin sites was decreased to $N_\omega = 27$. Such a small number of spin sites runs the risk of under-fitting,

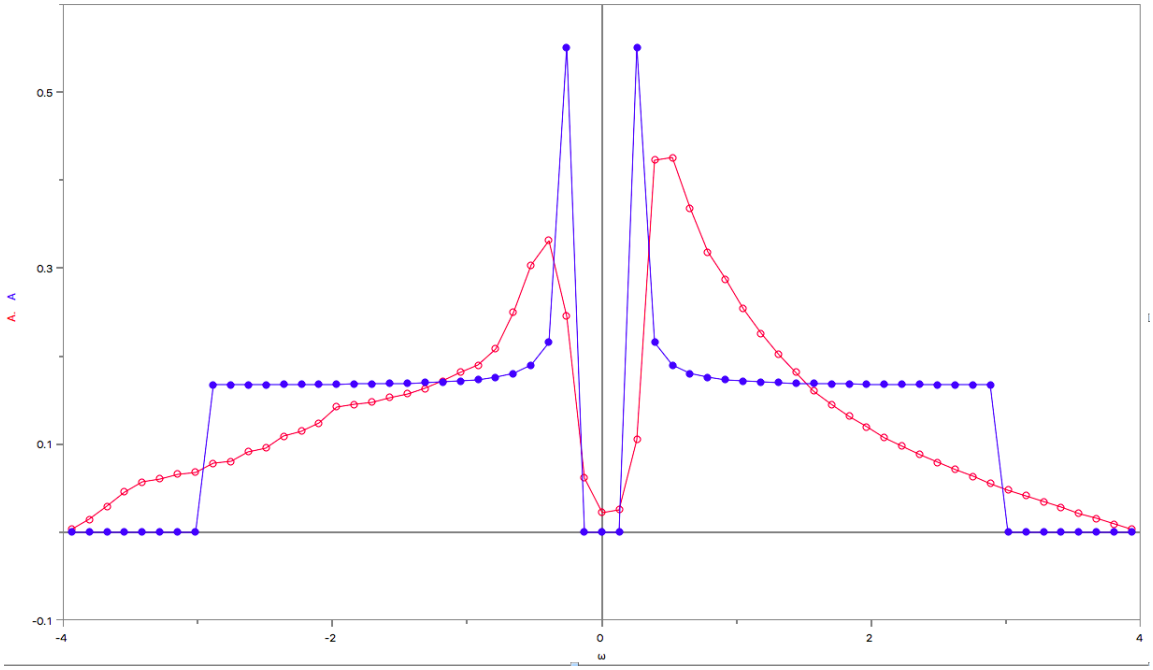

Figure 44: BCS spectrum with $N_\omega = 60$ and increased transverse field past the lower end of the quantum critical region. Features of the spectrum are smoothed out as a result, and this is a less than optimal fit.

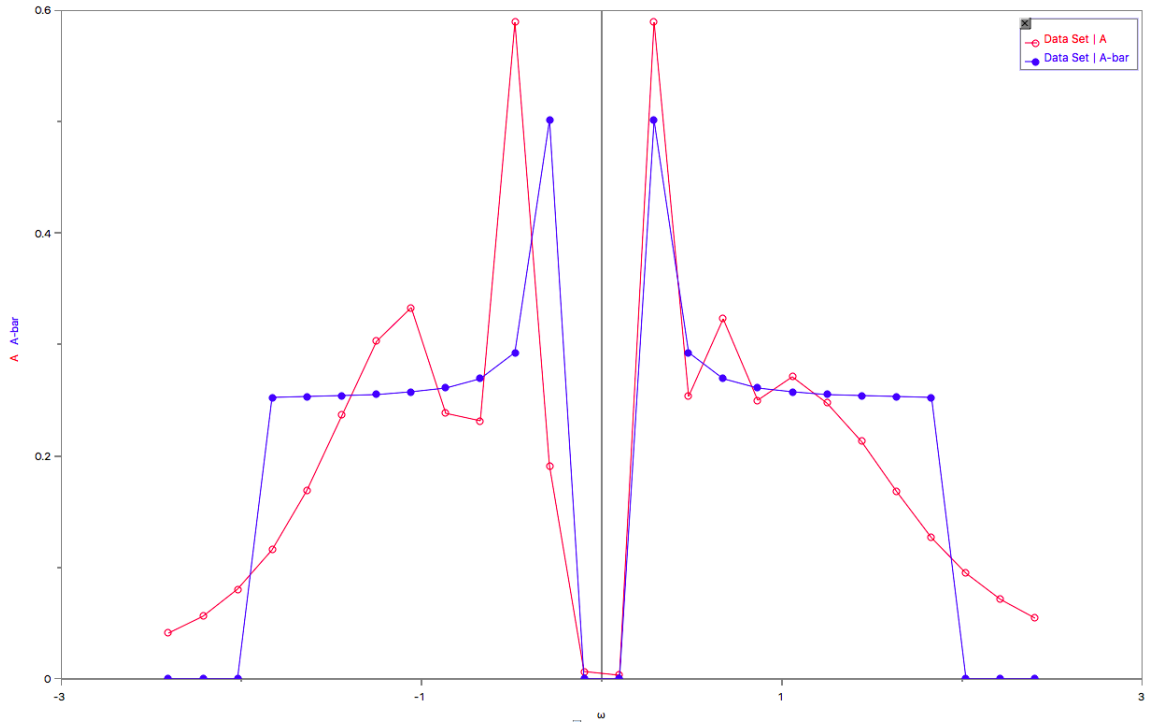

Figure 45: Reduced gap BCS spectrum with $N_\omega = 27$.

but the resulting $\overline{A}$ resulted in good agreement with the true spectrum with respect to the gap and adjacent peaks.

10.5 Double peak spectrum

Double peaks can be found in many types of many body spectra, ranging from photo absorption cross-sections of He^3 or He^4 clusters, line splitting arising from distinct sub-lattice susceptibilities induced in opposing directions along an Ising chain in the presence of a magnetic field, or the spectral density of a resonant Fermi polaron [2, 10, 28, 46].

While appearing simple, modeling this type of data can prove difficult, especially in the case of close Gaussian peaks with varying widths. The first synthetic spectra A to be tested was one withe double peaks at $\omega = -2.3$ and $\omega = 3.0$, with respective maximums of $A = 4.8$ and $A = 2.9$.

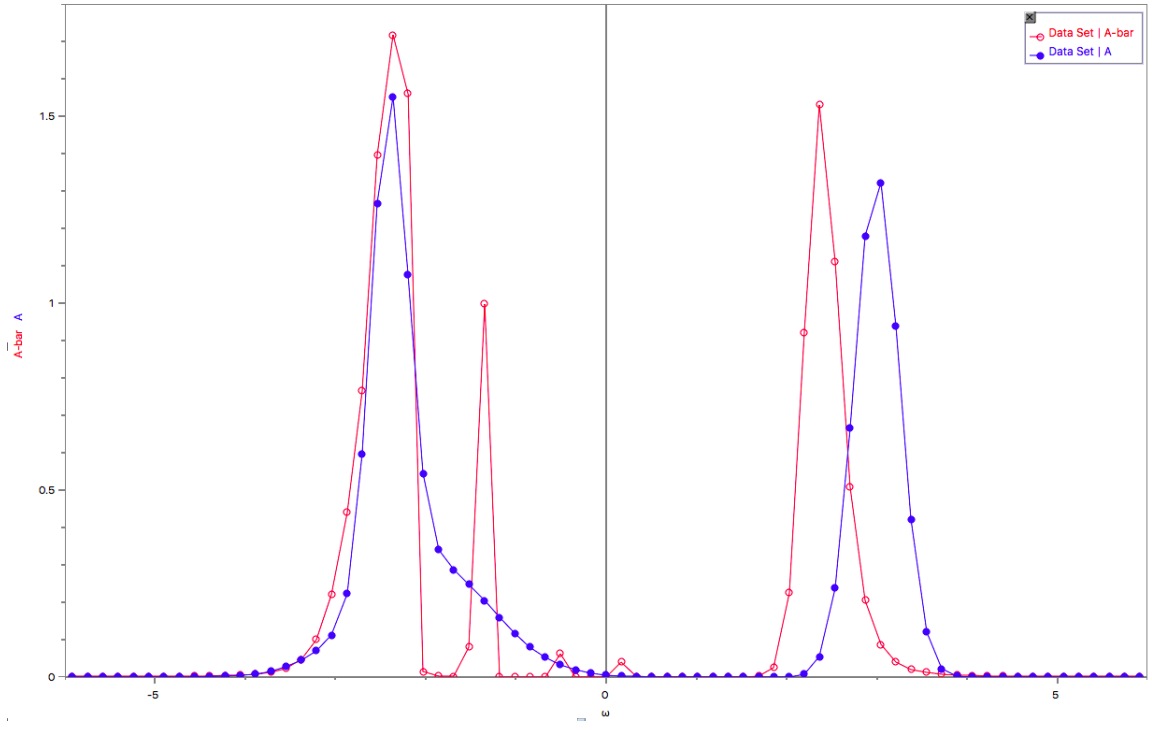

Figure 46: Double Gaussian spectrum with a spurious peak and shift of second Gaussian.

The optimized beta and transverse values are $\beta = 11$ and $B^x = 7.0 \times 10^{10}$, with $N_\tau = 30$ and $N_\omega = 65$. In addition, an exponential transverse field bias was applied to B^x with a polynomial $\alpha = 0.55$, in order to aid with regularization in the outer edges of the spectrum.

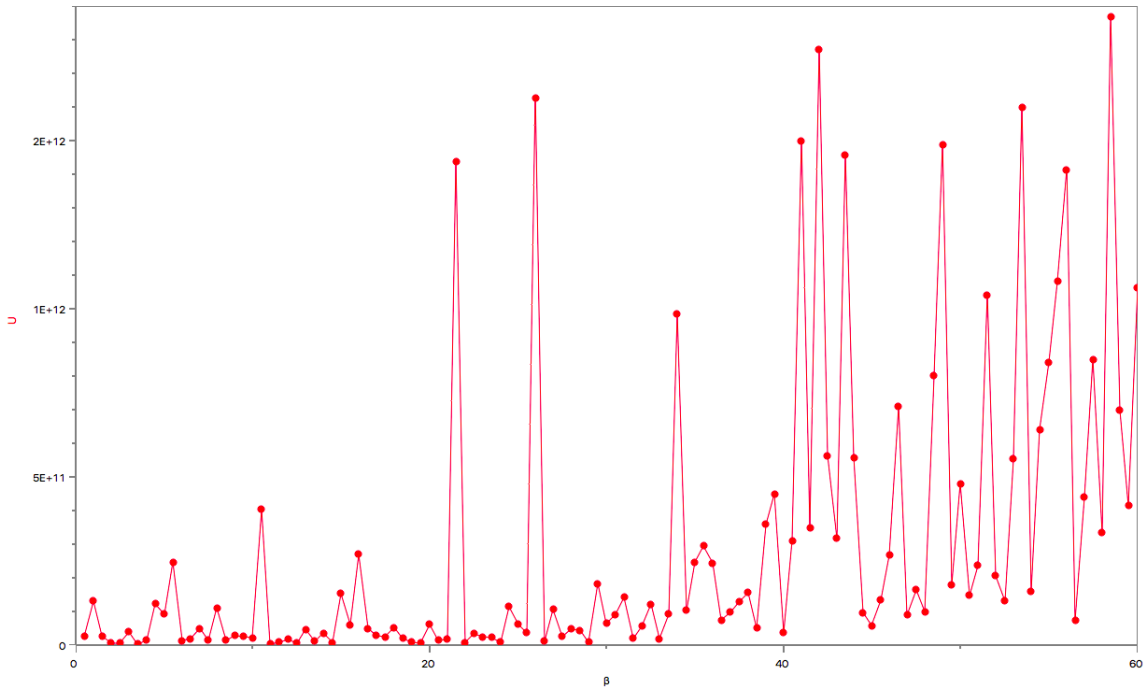

Figure 47: Thermal annealing profile for double Gaussian spectrum, resulting in $\beta = 11$.

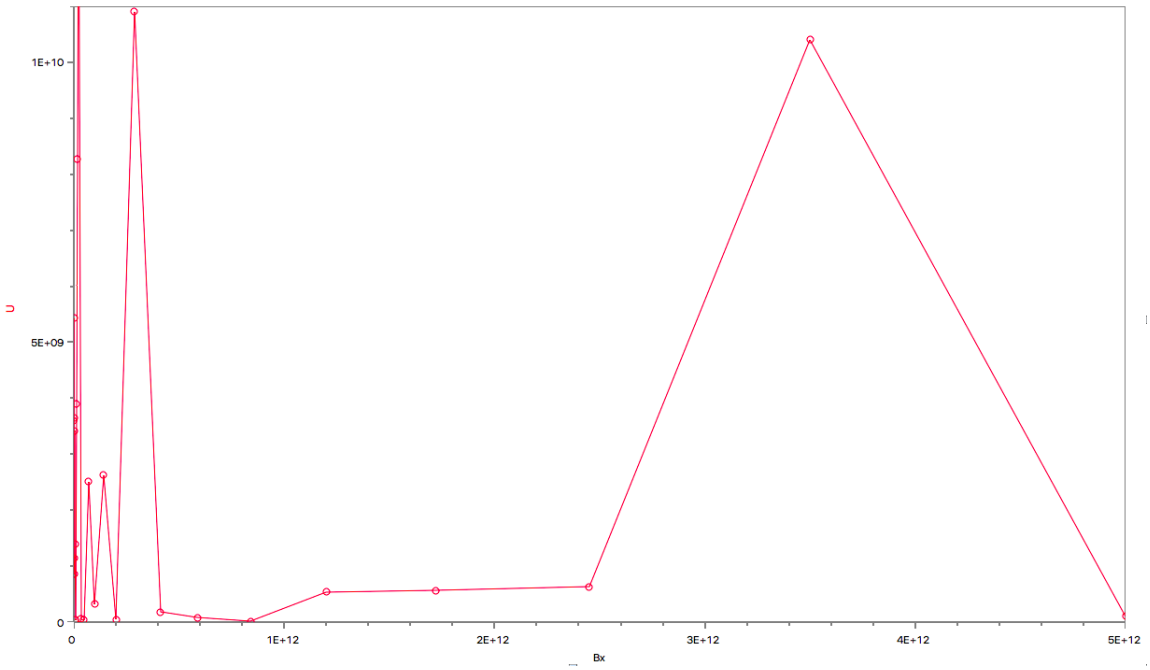

Figure 48: Quantum annealing profile for double Gaussian spectrum.

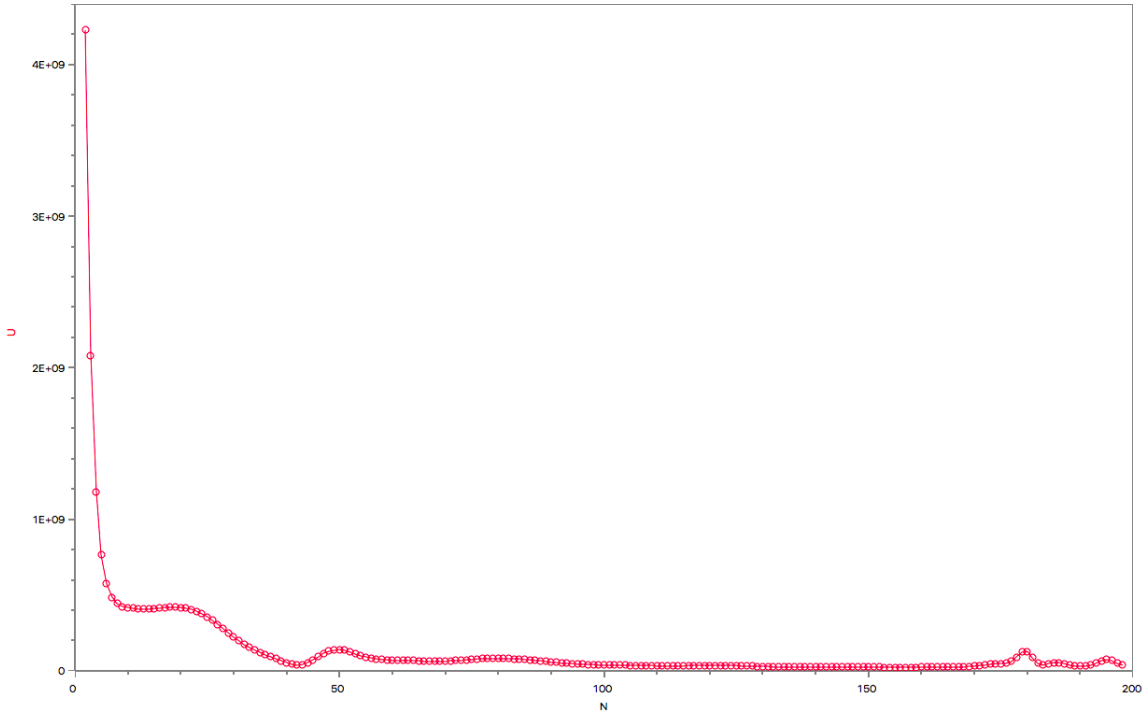

Figure 49: Internal energy vs iteration number profile for double Gaussian.

At an initial noise level $\sigma = 10^{-5}$, both peaks are present, with the $\overline{A}$ peak corresponding to $\omega = 2.7$ overlapping that of the true spectrum.

However, the maximum is overshot to close to a value of $\overline{A} = 10$. This shift in spectral weight from the true spectrum results in consequences in other parts of the spectrum.

The $\omega = 3.0$ peak is present, but shifted to to the left to $\omega = 2.0$, and although the width is close to the true spectrum's, the height is reduced from $\overline{A} = 2.9$ to approximately $\overline{A} = 2.0$.

The leftward shift and sharpness of the right peak is also effected by the exponential bias of the field. While using an exponential bias can aid in convergence along the outer edges of a spectrum, it can have a noticeable shifting effect on $\overline{A}$ as the overall transverse field increases.

A sharp, errant peak at $\omega = -1.3$ is also present, an indication of the need to reduce the configurational pressure by further optimizing endpoints.

Reducing the noise to $\sigma = 10^{-6}$, increasing the field to 1.0×10^{11}, and adjusting the endpoints improved the quality of the match. The $\overline{A} = -2.7$ peak matches the height and width of the original peak, with only the lower right edge diverge away from the original spectrum's curvature. The right peak is also a better match, nearly overlapping the original spectrum with

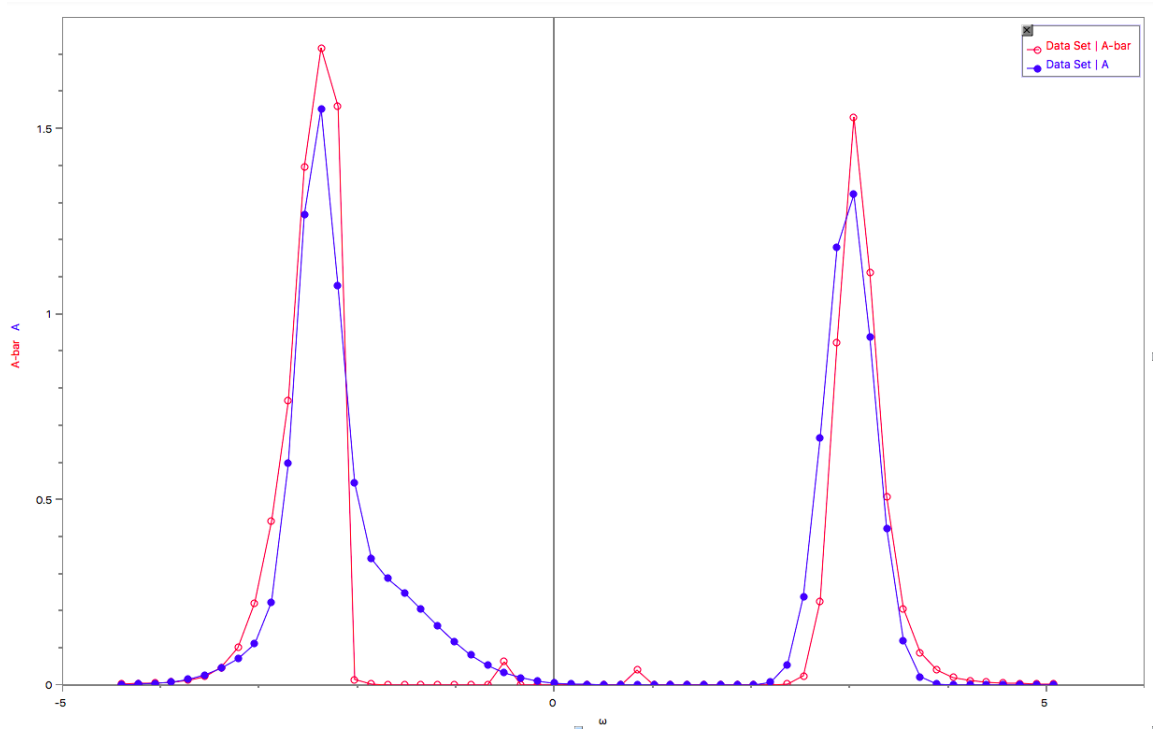

Figure 50: Improved double Gaussian spectrum by way of increased time points and decreased noise.

only a minor divergence of approximately $\Delta\omega = 0.2$.

Because of the shift in spectral weight from the left edge, a small bump at approximately $\omega = 0.2$ can be seen.

Figure 51 shows an attempt at a triple peak spectrum with noise $\sigma = 10^{-5}$ with $N_\tau = 60$. The increased complexity of the spectrum results in difficult in obtaining convergence with all three peaks, although the two peaks show fidelity to the original spectrum, and the third retains the shape of A, if slightly shifted along the ω grid to the left. This shows the QF is capable of displaying complicated Gaussian spectra even with imaginary time points numbering in the $10s$.

10.6 Edge-divergent spectrum with power law decay

The spectra associated with a dynamic structure factor can be characterized by an edge divergence and a power law decay as ω approaches a positive maximum [17, 32, 48, 51].

The equation used to create synthetic spectra of this type is

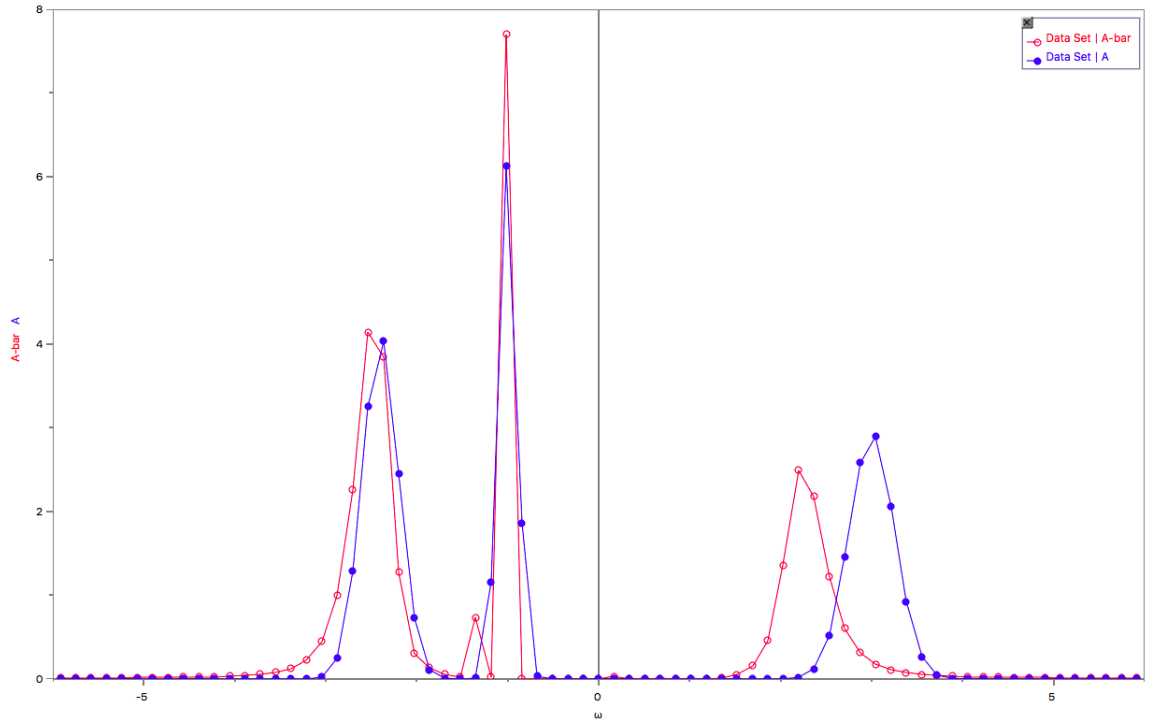

Figure 51: Triple Gaussian spectrum with optimized parameters.

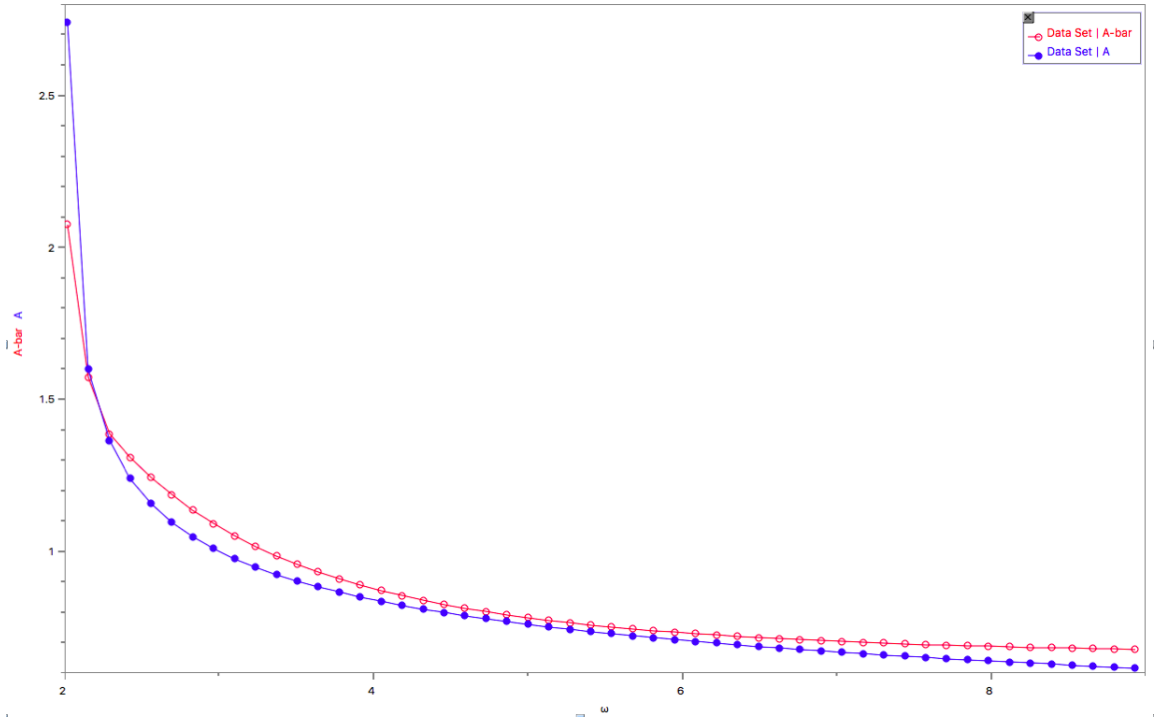

Figure 52: Edge-divergent decaying spectrum with exponent $d = 0.25$ and divergence at $\omega = 1.95$.

$$A(\omega) = \frac{1}{(\omega - \omega_0)^d} \tag{10.3}$$

where d is the exponential rate of decay.

Several edge-divergent spectra were created with varying magnitudes of d and studied. In each case it was found that using an edge constraint led to the best result for $\overline{A}$, minimizing the amount of spectral weight allowed past the edge divergence during each successive amplitude update due to the subsequent release of entropic pressure around the edge of divergence [26].

For each of the spectra in this series, the divergence edge ω_0 was set to $\omega = 2.0$, with the left endpoint to the spectrum set to $\omega = 1.95$ for constraint optimization.

Setting parameters $N_\omega = 52$ and $N_\tau = 60$, the optimized beta and transverse fields are $\beta = 9.1$ and $B^x = 6.0 \times 10^9$. The chemical potential of the system was set to $\mu = 1.0 \times 10^7$. At a noise level of $\sigma = 10^{-5}$, with a maximum bond dimension of 3.6×10^3, the minimum energy of the system is 5.1×10^4 at 177 updates. The average fluctuation per spin at its E_{min} was .12.

$\overline{A}$ shows a good fit to A, overlapping the exponential decay along the positive ω limit. Along the divergent edge, $\overline{A}$ shows a maximum of 2.1 compared to A's true maximum of 2.7. $\overline{A}$ attempts to match the curvature of the true spectrum, but narrowly misses at approximately $\omega = 2.1$, leveling off slightly before its overlap for the duration of the decay.

An increase for the exponential decay can be found in Figure 53 with $d = 0.45$. The number of spin sited and time points were kept the same, although annealing processes resulted in optimized parameter of $\beta = 48.9$ and $B^x = 6.0 \times 10^9$.

As with the $d = .25$ case, the left endpoint at $\omega = 1.95$ was used as a optimization constraint, limiting weight leakage beyond the edge.

The decaying limit once again shows strong overlap. The max at $\omega = 2.0$ reaches $\overline{A} = 5.1$ compared to A's true maximum of 6.1. The immediate drop off diverges slightly at 2.1, exhibiting a pattern initially noticeable with the $d = 0.25$ case. As with before, this minor shift corrects itself at approximately $\omega = 3.5$ and beyond. This divergence could not be resolved even with an increase of time points or reduction of noise.

For the best-fit $\overline{A}$, the system has an internal energy of 1.3×10^5 and an average fluctuation of $\Delta n = 0.11$ after 56 updates.

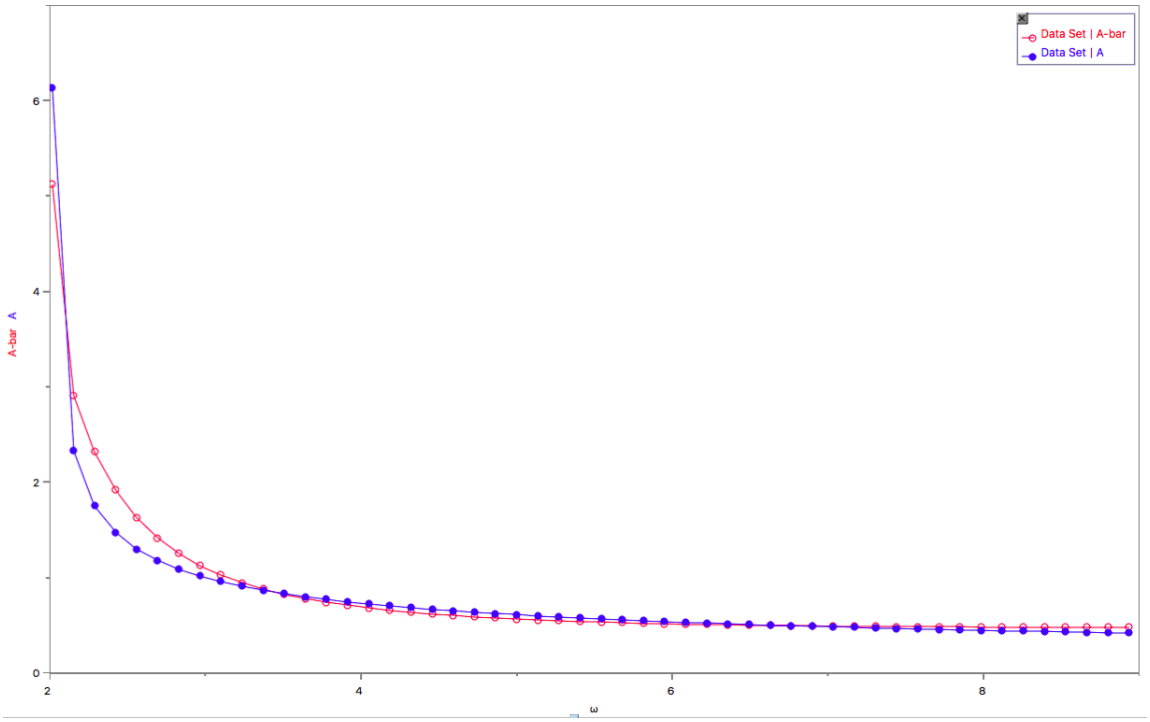

Figure 53: Edge-divergent decaying spectrum with exponent $d = 0.45$ and divergence at $\omega = 1.95$.

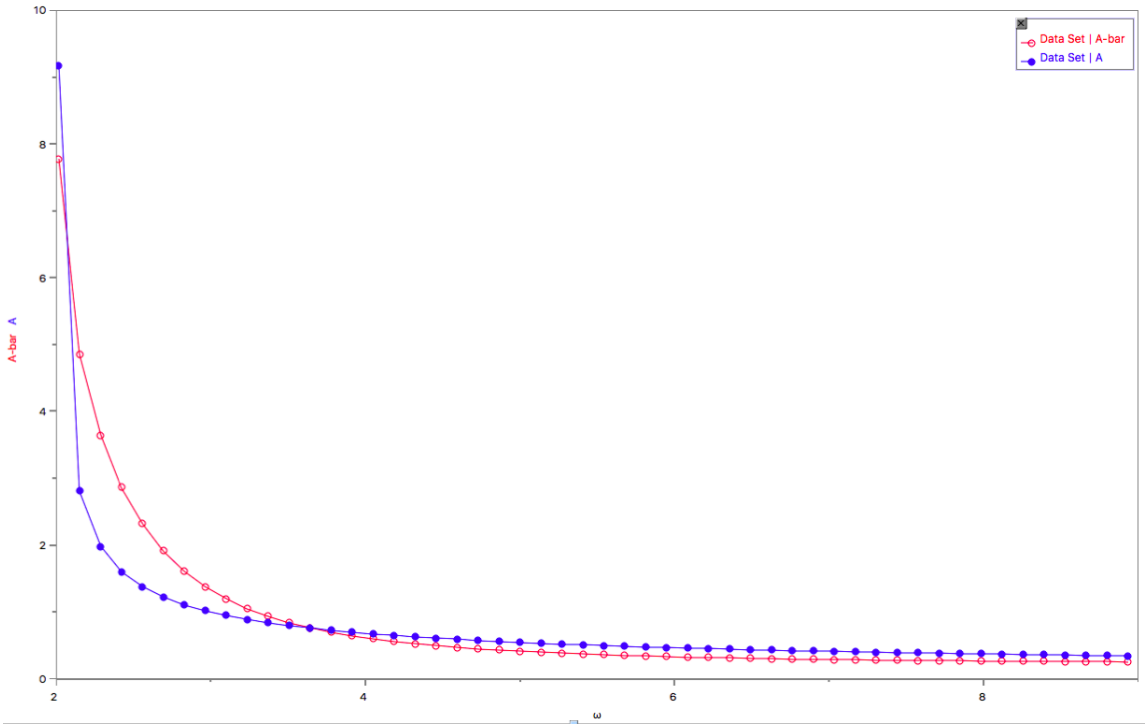

Figure 54: Edge-divergent decaying spectrum with exponent $d = 0.55$ and divergence at $\omega = 1.95$.

A third case in Figure 54 involved increasing the exponential decay to $d = 0.65$, leaving the frequency discretization unchanged and adjusting the amount of time points to $N_\tau = 130$.

The amount of noise present in $G(\tau)$ was set to be $\sigma = 10^{-5}$, with the max bond dimension set to be 5.6×10^3.

The chemical potential of the system was initially set at $\mu = 5000$, with the initial default model once again a horizontal line that matches the normalization integral of $A(\omega)$.

Optimized β and B^x parameters were 30.2 and 5.0×10^9, showing that the physical system required a higher temperature, and lower β, to reach convergence. This combination of parameters resulted in a faster fit than the two prior cases, taking 36 updates.

The endpoint constraint once again greatly aids in converge, resulting in an edge maximum of $\overline{A} = 7.7$, compared to a true maximum of $A = 9.1$.

While there is overlap between A and $\overline{A}$ at approximately $\omega = 3.5$, a slight vertical shift is noticeable towards the positive omega limit, despite the overall curvature matching.

The steep initial decay from the maximum proves difficult to match, resulting in an even more pronounced divergence between A and $\overline{A}$ as it tapers towards its asymptotic limit. Despite this, it remains a solid result, retaining the original spectrum's shape and not exhibiting any oscillatory behavior.

For the physical system, this best fit occurs at a minimum energy of 5.3×10^5, with an average fluctuation of 0.11 per spin site.

It's interesting to note that additional constraints to correct the maximum height at $\omega = 2.0$ were attempted, such as fixing the amplitude at the edge to the true value [26]. However, such attempts resulted in an immediate collapse of $\overline{A}$ at adjacent sites around the edge, contributing to other spurious peaks appearing further along the spectra.

Further tests with grid sampling around the curvature range of frequencies, combined with amplitude fixing of the maximum, show promise and should be studied further [41, 42, 52]

Extending the edge-divergence model a bit further, it's possible to synthesize spectra similar to what can be found with optical conductivity, luminescence decay, or emission spectra, by imposing an additional Gaussian along its decaying tail. [27, 38, 40]

As shown in Figure 55, the first of these synthetic spectra modeled and tested had the fol-

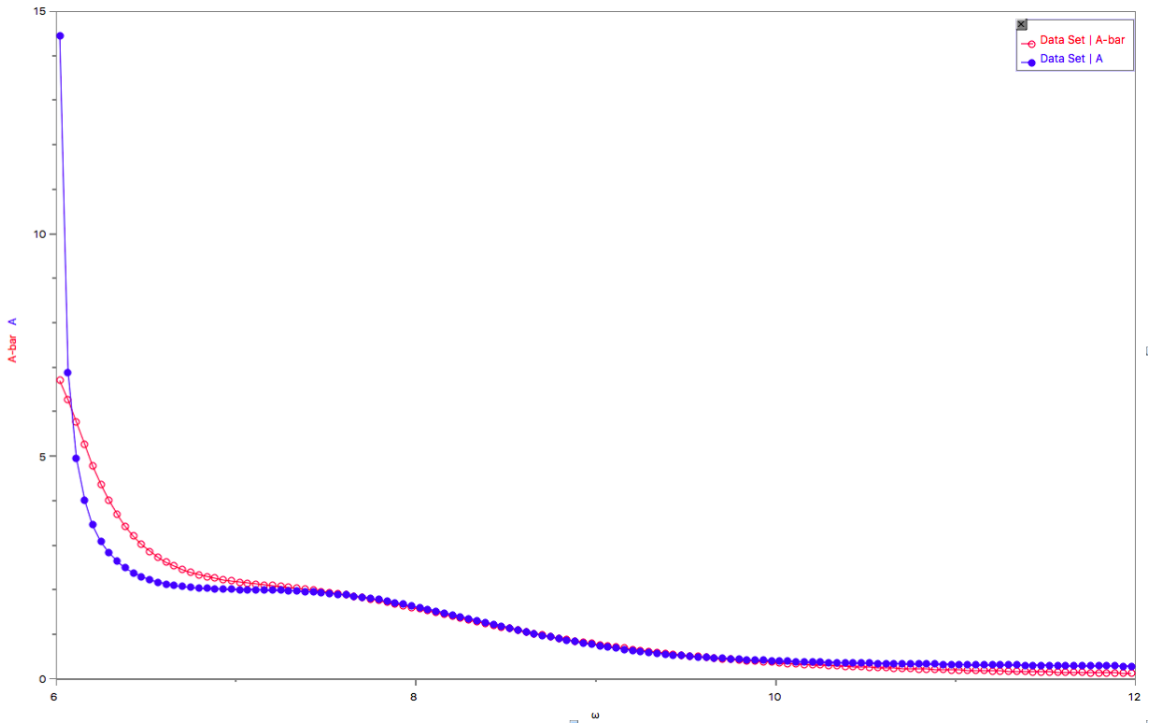

Figure 55: Optical decay spectrum with Gaussian at $\omega = 7.5$.

lowing characteristics: a divergence edge at $\omega = 6.0$ with captured maximum of approximately $\omega = 14.0$, an underlying decay with exponent $a = 0.55$, and a additional Gaussian centered at $\omega = 7.5$, with an underlying max of 1.0 and standard deviation of 0.8.

The Heisenberg spin chain consisted of $N_\omega = 132$ sites with a discretization size of $\Delta\omega = .045$, extending from $\omega = 6.0$ to $\omega = 12.0$. 10^{-5} of Gaussian noise was added to $G(\tau)$ for $N_\tau = 30$ time points. Simulated annealing process found optimized parameters $\beta = 28$ and $B^x = 6.0 \times 10^8$.

The best fit for $\overline{A}$ had a $E_{\min} = 2.3 \times 10^{13}$ after 23 amplitude updates. $\overline{A}$ exhibits good overlap with A after the divergent edge, capturing both the decay and the small bump due to the second Gaussian.

The true amplitude maximum of A at $\omega = 6.0$ is reflected by a reduced max of $\overline{A} = 4.0$, the only noticeable divergence from the true spectrum. Although sampled with a fixed frequency grid, a combined approach of amplitude fixing along with grid sampling could prove to be effective in further attempts with this type of spectra.

A more complicated case is shown in Figure 56. Once again the original spectrum's shape and characteristics are recognizable, although there is a shift in the Gaussian bump from

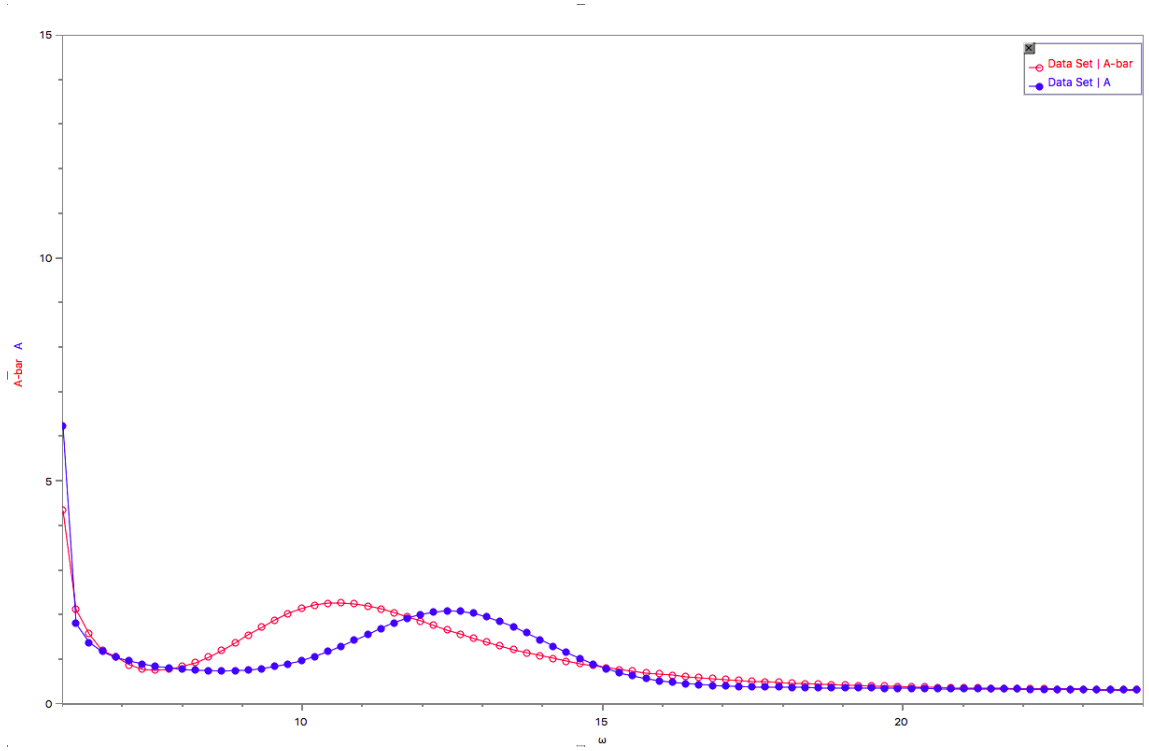

Figure 56: Optical decay spectrum with Gaussian at $\omega = 12.5$.

$\omega = 12.5$ to $\omega = 10.5$.

The physical system used to model the spectrum consisted of $N_\tau = 80$ spin sites representing a frequency discretization of $\Delta\omega = .225$ from $\omega = 6.0$ to $\omega = 24$.

The optimized parameters are $\beta = 18.2$ and $B^x = 5.0 \times 10^{17}$. To maintain normalization a chemical potential of $\mu = 6.0 \times 10^3$ was pumped into the system with each update, resulting in average fluctuations of $\Delta n = 0.10$. The minimum energy for convergence was $E_{\min} = 4.5 \times 10^8$.

$\overline{A}$ shows a peak of an approximate height 2.2 compared to the true spectrum's maximum of 6.2, but the Gaussian peak is apparent, if slightly shifted.

Despite the shift, $\overline{A}$'s Gaussian shares the true spectrum's Gaussian's height and width, and $\overline{A}$ overlaps the true spectrum in the positive limit of the ω grid.

10.7 Boson decay spectum

The final model proved to be the most difficult, although it does capture the shape and characteristics of the spectrum without smearing out the defining features.Boson decay spectra can be characterized by a Gaussian in addition to a divergent peak with a power decay tail [44].

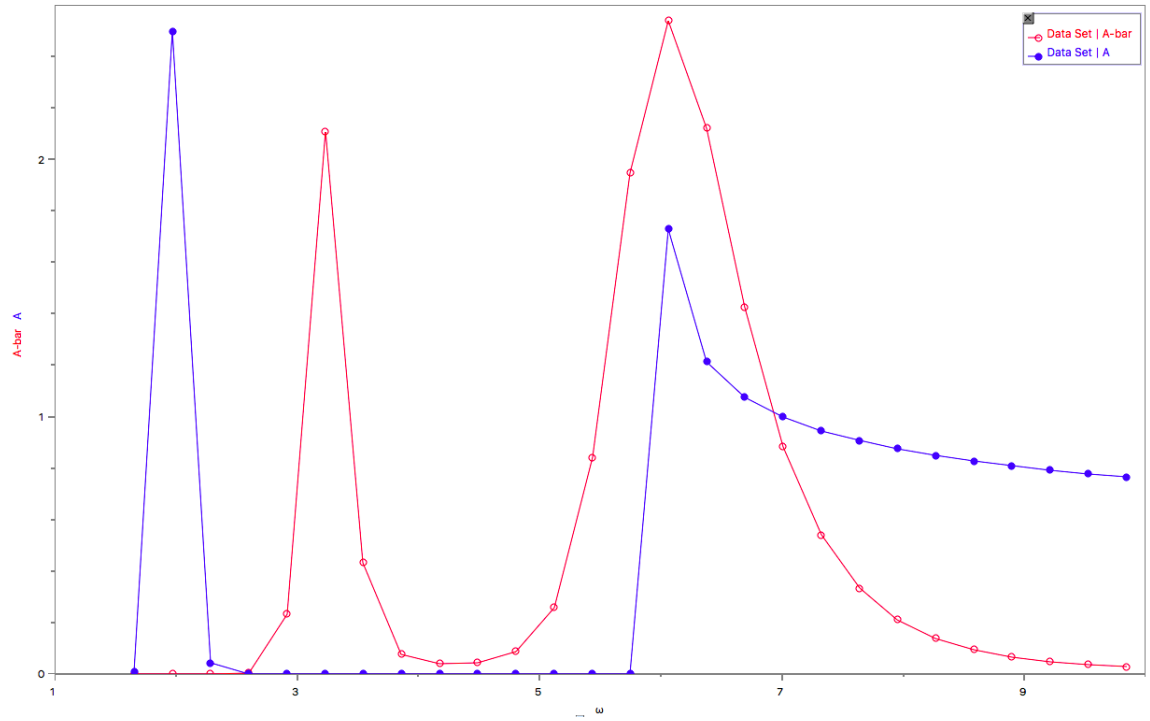

Figure 57: Bosonic decay spectrum.

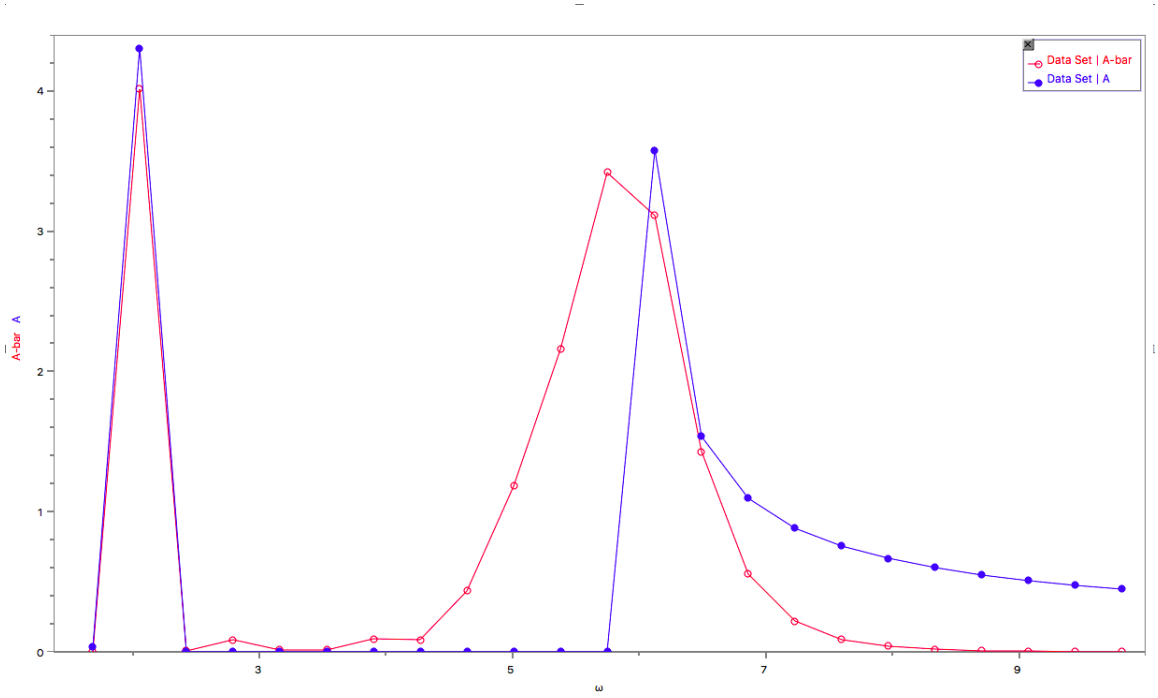

Figure 58: Bosonic decay spectrum with left endpoint adjustment from $\omega = 1.3$ to $\omega = 1.5$.

The spectrum in Figure 57 has a Gaussian of height 2.5 at $\omega = 2.0$ and an decaying exponential with a sharp edge at $\omega = 6.0$.

Optimized parameters were $\beta = 32$ with a transverse field of 2.0×10^6. The minimum energy of the spin system was $E_{\min} = 3.2 \times 10^8$ with an average fluctuation of $\Delta n = 0.11$ after240 updates. $\overline{A}$ retains the shape of the true spectrum, capturing the Gaussian's shape and height, although shifted from the right. The peak of the decaying exponential is present, although the overall shape is distorted.

Optimizing the endpoints led to a better result, as seen in Figure 58. All parameters were kept the same, resulting in 246 updates to converge, with an average fluctuation per field of approximately $\Delta n = 0.11$. The minimum energy was approximately the same as with the previous attempt.

By restricting the leakage of spectral weight from the left side of the spectrum, the Gaussian is captured. The straight edge of the divergent peak is clearly present and so is its decay.

Although unable to replicate A perfectly, the QF method shows promise despite the complexity of the underlying spectrum. Further optimization techniques are currently being researched that might aid in better matching.

11 CONCLUSIONS AND PROSPECTS

As microprocessor advancement/size reduction keeps pace with Moore's Law, racing towards a theoretical quantum threshold, and attempts at efficient quantum computing become more ubiquitous, there is an increasing need to find ways to solve problems using the tools and mathematical literature of quantum mechanics.

The Quantum Fluctuation method intersects the fields of condensed matter physics, computer science, and quantum information processing to solve the analytic continuation inversion.

Results thus far have supported theory. Spectral functions with simple geometric shapes such as a semi-circle, and those models with an added gap, have been been captured with success.

The same can be said about BCS, Gaussian peak, and divergent-edge power law spectra. Distinguishing characteristics of the more complicated, gapped BCS model have also been captured. Gap width matches that of the true spectral function, and peaks are prevalent.

Quantified errors include the variance of each time measurement of G. Other potential sources of error stem from the sensitivity of any variance between the respective m measurements of A and D, the error threshold within the MPS architecture, and machine error.

Although there has been research on and using the stochastic analytic approach [5, 55], attempts to further refine it [15, 24], and comparison between it and other optimization methods including MEM, numerical MPS-based [33], and using data from Heisenberg models to sample, this appears to be the first to use actual quantum fluctuations to solve an analytic continuation problem.

The presented research is robust enough to admit further investigations along several branches. Recent research has used techniques such as machine learning to train models to sample and generate its own spectral data [35, 53, 54]. Such exploration is in its early stages, and offers opportunities beyond merely single families of spectra [45].

Another possible avenue is to formalize the relationship between the transverse field limits

of the QF model and that of quantum phase transitions, in a generalized manner and also specific to different quantum models beyond that of the 1D Heisenberg.

While this research strictly deals with a 1D chain because of the DMRG's ability to explore its ground state properties in a reduced dimensional manner, it is possible that research could expand into higher dimensional models.

In addition, research in areas such as grid optimization, density averaging, and default model selection are primed to be explored [42]. The design of a quantum algorithm to implement the QF is a further possibility.

The QF algorithm, as currently written, can still be improved. While adequate at resolving the spectra with a single defining characteristic, the QF model can be improved to resolve spectra with multiple, competing characteristics such as that with simultaneous Gaussian peaks and exponential decay.

Given time and additional numerical and computational tools, there is plenty of room for continued refinement.

LIST OF REFERENCES

[1] E. Schrödinger. “Quantisierung als Eigenwertproblem”. In: *Annalen der Physik* 384.4 (1926), pp. 361–376. DOI: 10.1002/andp.19263840404.

[2] O. A. Starykh, A. W. Sandvik, and R. R. P. Singh. “Dynamics of the spin- Heisenberg chain at intermediate temperatures”. In: *Phys. Rev. B* 55 (22 June 1997), pp. 14953–14967. DOI: 10.1103/PhysRevB.55.14953. URL: https://link.aps.org/doi/10.1103/PhysRevB.55.14953.

[3] Gregg Jaeger. “The Ehrenfest Classification of Phase Transitions: Introduction and Evolution”. In: *Archive for History of Exact Sciences* 53.1 (1998), pp. 51–81. DOI: 10.1007/s004070050021.

[4] Michael Karbach and Gerhard Muller. “Introduction to the Bethe ansatz I”. In: (1998). DOI: 10.48550/ARXIV.COND-MAT/9809162. URL: https://arxiv.org/abs/cond-mat/9809162.

[5] Anders W. Sandvik. “Stochastic Method for Analytic Continuation of Quantum Monte Carlo Data”. In: *Physical Review B* 57.17 (1998), pp. 10287–10290.

[6] Anders W. Sandvik et al. “Numerical calculations of the Raman spectrum of the two-dimensional Heisenberg model”. In: *Physical Review B* 57.14 (Apr. 1998), pp. 8478–8493. DOI: 10.1103/physrevb.57.8478. URL: https://doi.org/10.1103%2Fphysrevb.57.8478.

[7] E.B. Manoukian. “Quantum Physics of spin 1/2 and two-level systems; quantum predictions using such systems”. In: *Quantum Theory* 1 (2000), pp. 419–546. DOI: 10.1007/978-1-4020-4190-7_8.

[8] Subir Sachdev. “Quantum Criticality: Competing Ground States in Low Dimensions”. In: *Science* 288.5465 (Apr. 2000), pp. 475–480. DOI: 10.1126/science.288.5465.475. URL: https://doi.org/10.1126%2Fscience.288.5465.475.

[9] Matthias Vojta. “Quantum phase transitions”. In: *Reports on Progress in Physics* 66.12 (Nov. 2003), pp. 2069–2110. DOI: 10.1088/0034-4885/66/12/r01. URL: https://doi.org/10.1088%2F0034-4885%2F66%2F12%2Fr01.

[10] Sofia Quaglioni and Petr Navrátil. “The 4He total photo-absorption cross section with two- plus three-nucleon interactions from chiral effective field theory”. In: *Physics Letters B* 652.5-6 (Sept. 2007), pp. 370–375. DOI: 10.1016/j.physletb.2007.06.082. URL: https://doi.org/10.1016%2Fj.physletb.2007.06.082.

[11] G. Vidal. “Classical Simulation of Infinite-Size Quantum Lattice Systems in One Spatial Dimension”. In: *Physical Review Letters* 98.7 (Feb. 2007). DOI: 10.1103/physrevlett.98.070201. URL: https://doi.org/10.1103%2Fphysrevlett.98.070201.

[12] Antonio M. Garcı a-Garcıa et al. “Bardeen-Cooper-Schrieffer Theory of Finite-Size Superconducting Metallic Grains”. In: *Physical Review Letters* 100.18 (May 2008). DOI: 10.1103/physrevlett.100.187001. URL: https://doi.org/10.1103%2Fphysrevlett.100.187001.

[13] N. B. Kopnin and E. B. Sonin. “BCS Superconductivity of Dirac Electrons in Graphene Layers”. In: *Physical Review Letters* 100.24 (June 2008). DOI: 10.1103/physrevlett.100.246808. URL: https://doi.org/10.1103%2Fphysrevlett.100.246808.

[14] R. Coldea et al. “Quantum Criticality in an Ising Chain: Experimental Evidence for Emergent E sub8/sub Symmetry”. In: *Science* 327.5962 (Jan. 2010), pp. 177–180. DOI: 10.1126/science.1180085. URL: https://doi.org/10.1126%2Fscience.1180085.

[15] S Fuchs, M Jarrell, and T Pruschke. “Application of Bayesian Inference to Stochastic Analytic Continuation”. In: *Journal of Physics: Conference Series* 200 (Feb. 2010), p. 012041. DOI: 10.1088/1742-6596/200/1/012041.

[16] Norbert Schuch and J. Ignacio Cirac. “Matrix product state and mean-field solutions for one-dimensional systems can be found efficiently”. In: *Physical Review A* 82.1 (July 2010). DOI: 10.1103/physreva.82.012314. URL: https://doi.org/10.1103%2Fphysreva.82.012314.

[17] B. Xie et al. “Inelastic x-ray scattering study of the state-resolved differential cross section of Compton excitations in helium atoms”. In: *Phys. Rev. A* 82 (Sept. 2010), p. 032501. DOI: 10.1103/PhysRevA.82.032501.

[18] Pasquale Calabrese, Fabian H. L. Essler, and Maurizio Fagotti. “Quantum Quench in the Transverse-Field Ising Chain”. In: *Physical Review Letters* 106.22 (June 2011). DOI: 10.1103/physrevlett.106.227203. URL: https://doi.org/10.1103%2Fphysrevlett.106.227203.

[19] Hamed Saberi. “Matrix-product states for strongly correlated systems and quantum information processing”. In: *Physical Review A* 85.5 (2012), p. 052323.

[20] A. W. Kinross et al. “Evolution of Quantum Fluctuations Near the Quantum Critical Point of the Transverse Field Ising Chain System”. In: *Physical Review X* 4.3 (July 2014). DOI: 10.1103/physrevx.4.031008. URL: https://doi.org/10.1103%2Fphysrevx.4.031008.

[21] Neil J. Robinson et al. “Quasiparticle breakdown in the quasi-one-dimensional Ising ferromagnet $CoNb_2O_6$”. In: *Phys. Rev. B* 90 (17 Nov. 2014), p. 174406. DOI: 10.1103/PhysRevB.90.174406. URL: https://link.aps.org/doi/10.1103/PhysRevB.90.174406.

[22] Mason Swanson et al. “Dynamical Conductivity across the Disorder-Tuned Superconductor-Insulator Transition”. In: *Phys. Rev. X* 4 (2 Apr. 2014), p. 021007. DOI: 10.1103/PhysRevX.4.021007. URL: https://link.aps.org/doi/10.1103/PhysRevX.4.021007.

[23] Piers Coleman. *Introduction to many-body physics*. Cambridge University Press, 2015.

[24] F. Bao et al. “Fast and efficient stochastic optimization for analytic continuation”. In: *Physical Review B* 94.12 (Sept. 2016). DOI: 10.1103/physrevb.94.125149. URL: https://doi.org/10.1103%2Fphysrevb.94.125149.

[25] Dominic Bergeron and A.-M. S. Tremblay. “Algorithms for optimized maximum entropy and diagnostic tools for analytic continuation”. In: *Phys. Rev. E* 94 (2 Aug. 2016), p. 023303. DOI: 10.1103/PhysRevE.94.023303. URL: http://link.aps.org/doi/10.1103/PhysRevE.94.023303.

[26] Anders W. Sandvik. “Constrained sampling method for analytic continuation”. In: *Physical Review E* 94.6 (Dec. 2016). DOI: 10.1103/physreve.94.063308. URL: https://doi.org/10.1103%2Fphysreve.94.063308.

[27] Xin Wen et al. “Highly Tm3+ doped germanate glass and its single mode fiber for 2.0 m laser”. In: *Scientific Reports* 6 (Feb. 2016), p. 20344. DOI: 10.1038/srep20344.

[28] Olga Goulko et al. “Numerical analytic continuation: Answers to well-posed questions”. In: *Physical Review B* 95.1 (Jan. 2017). DOI: 10.1103/physrevb.95.014102. URL: https://doi.org/10.1103%2Fphysrevb.95.014102.

[29] Xing-Jie Han et al. “Analytic Continuation with Padé Decomposition”. In: *Chinese Physics Letters* 34.7 (July 2017), p. 077102. DOI: 10.1088/0256-307x/34/7/077102. URL: https://doi.org/10.1088%2F0256-307x%2F34%2F7%2F077102.

[30] Steen Hannestad and Thomas Tram. *Optimal prior for Bayesian inference in a constrained parameter space*. 2017. DOI: 10.48550/ARXIV.1710.08899. URL: https://arxiv.org/abs/1710.08899.

[31] Ryan Levy, J.P.F. LeBlanc, and Emanuel Gull. “Implementation of the maximum entropy method for analytic continuation”. In: *Computer Physics Communications* 215 (June 2017), pp. 149–155. DOI: 10.1016/j.cpc.2017.01.018. URL: https://doi.org/10.1016%2Fj.cpc.2017.01.018.

[32] Youssef Kora and Massimo Boninsegni. “Dynamic structure factor of superfluid from quantum Monte Carlo: Maximum entropy revisited”. In: *Physical Review B* 98.13 (Oct. 2018). DOI: 10.1103/physrevb.98.134509. URL: https://doi.org/10.1103%2Fphysrevb.98.134509.

[33] et al Yu-Rong Shu Maxime Dupont. “Dynamical properties of the S=1/2 random Heisenberg chain”. In: *Physical Review B: Condensed Matter and Materials Physics* 97.10 (2018), p. 104424.

[34] Hal Tasaki. *Introduction to the "second quantization" formalism for non-relativistic quantum mechanics: A possible substitution for Sections 6.7 and 6.8 of Feynman's "Statistical Mechanics"*. 2018. DOI: 10.48550/ARXIV.1812.10732. URL: https://arxiv.org/abs/1812.10732.

[35] Hongkee Yoon, Jae-Hoon Sim, and Myung Joon Han. “Analytic continuation via domain knowledge free machine learning”. In: *Phys. Rev. B* 98 (24 Dec. 2018), p. 245101. DOI: 10.1103/PhysRevB.98.245101. URL: https://link.aps.org/doi/10.1103/PhysRevB.98.245101.

[36] William Huggins et al. “Towards quantum machine learning with tensor networks”. In: *Quantum Science and Technology* 4.2 (Jan. 2019), p. 024001. DOI: 10.1088/2058-9565/aaea94. URL: https://doi.org/10.1088%2F2058-9565%2Faaea94.

[37] Pranay Patil et al. “Obstacles to quantum annealing in a planar embedding of XORSAT”. In: *Phys. Rev. B* 100 (5 Aug. 2019), p. 054435. DOI: 10.1103/PhysRevB.100.054435. URL: https://link.aps.org/doi/10.1103/PhysRevB.100.054435.

[38] Honge wu et al. “LaF3: Pr3+ hollow hexagon nanostructures via green and eco-friendly synthesis and their photoluminescence properties”. In: *Journal of Materials Science* 54 (Feb. 2019). DOI: 10.1007/s10853-018-3042-5.

[39] Matthew Fishman, Steven R. White, and E. Miles Stoudenmire. *The ITensor Software Library for Tensor Network Calculations*. 2020. arXiv: 2007.14822.

[40] Dangli Gao et al. “Enhancing the red upconversion luminescence of hybrid porous microtubes: Via an in situ O -substituted reaction through heat treatment”. In: *Journal of Materials Chemistry C* 8 (Oct. 2020). DOI: 10.1039/D0TC04153J.

[41] Khaldoon Ghanem and Erik Koch. “Average spectrum method for analytic continuation: Efficient blocked-mode sampling and dependence on the discretization grid”. In: *Physical Review B* 101.8 (Feb. 2020). DOI: 10.1103/physrevb.101.085111. URL: https://doi.org/10.1103%2Fphysrevb.101.085111.

[42] Khaldoon Ghanem and Erik Koch. “Extending the average spectrum method: Grid point sampling and density averaging”. In: *Phys. Rev. B* 102 (3 July 2020), p. 035114. DOI: 10.1103/PhysRevB.102.035114. URL: https://link.aps.org/doi/10.1103/PhysRevB.102.035114.

[43] Eric Lechner et al. “Electron Tunneling and X-Ray Photoelectron Spectroscopy Studies of the Superconducting Properties of Nitrogen-Doped Niobium Resonator Cavities”. In: *Physical Review Applied* 13 (Apr. 2020). DOI: 10.1103/PhysRevApplied.13.044044.

[44] Jeffrey Roskes. “Higgs Boson Data Analysis”. In: *A Boson Learned from its Context, and a Boson Learned from its End*. Cham: Springer International Publishing, 2020, pp. 73–118. ISBN: 978-3-030-58011-7. DOI: 10.1007/978-3-030-58011-7_5. URL: https://doi.org/10.1007/978-3-030-58011-7_5.

[45] Taegeun Song, Roser Valenti, and Hunpyo Lee. *Analytic continuation of the self-energy via Machine Learning techniques*. 2020. DOI: 10.48550/ARXIV.2007.13610. URL: https://arxiv.org/abs/2007.13610.

[46] Seung-Ho Baek et al. “Persistence of Ising-like easy-axis spin correlations in the paramagnetic state of the spin-1 chain compound”. In: *Physical Review B* 104.21 (Dec. 2021). DOI: 10.1103/physrevb.104.214431. URL: https://doi.org/10.1103%2Fphysrevb.104.214431.

[47] Narek Hovsepyan. *On the optimal analytic continuation from discrete data*. 2021. DOI: 10.48550/ARXIV.2106.01471. URL: https://arxiv.org/abs/2106.01471.

[48] Inderpreet Kaur and Sankalpa Ghosh. *Bogoliubov spectrum and the dynamic structure factor in a quasi-two-dimensional spin-orbit coupled BEC*. 2021. DOI: 10.48550/ARXIV.2112.03505. URL: https://arxiv.org/abs/2112.03505.

[49] Guilherme Semione et al. "Temperature-dependent near-surface interstitial segregation in niobium". In: *Journal of Physics Condensed Matter* 33 (Apr. 2021). DOI: 10.1088/1361-648X/abf9b7.

[50] R. Mondaini, S. Tarat, and R. T. Scalettar. "Quantum critical points and the sign problem". In: *Science* 375.6579 (2022), pp. 418–424. DOI: 10.1126/science.abg9299. eprint: https://www.science.org/doi/pdf/10.1126/science.abg9299. URL: https://www.science.org/doi/abs/10.1126/science.abg9299.

[51] A. Schellenberger, M. Hörmann, and K. P. Schmidt. *Dynamic structure factor of the antiferromagnetic Kitaev model in large magnetic fields*. 2022. DOI: 10.48550/ARXIV.2203.13546. URL: https://arxiv.org/abs/2203.13546.

[52] Hui Shao and Anders W. Sandvik. *Progress on stochastic analytic continuation of quantum Monte Carlo data*. 2022. DOI: 10.48550/ARXIV.2202.09870. URL: https://arxiv.org/abs/2202.09870.

[53] Juan Yao et al. "Noise enhanced neural networks for analytic continuation". In: *Machine Learning: Science and Technology* 3.2 (May 2022), p. 025010. DOI: 10.1088/2632-2153/ac6f44. URL: https://doi.org/10.1088%2F2632-2153%2Fac6f44.

[54] Rong Zhang et al. *Training biases in machine learning for the analytic continuation of quantum many-body Green's functions*. 2022. DOI: 10.48550/ARXIV.2206.07493. URL: https://arxiv.org/abs/2206.07493.

[55] Kevin S D Beach. *Identifying the Maximum Entropy Method as a Special Limit of Stochastic Analytic Continuation*. URL: cond-mat/0403055.

[56] et al Dutta Amit. "Quantum Information Theoretic Measures: Transverse Field and Related Models". In: *Quantum Phase Transitions in Transverse Field Spin Models* (), pp. 122–148. DOI: 10.1017/cbo9781107706057.010.

[57] V. Murg F. Verstraete J.I. Cirac. *Matrix Product States, Projected Entangled Pair States, and variational normalization group methods for quantum spin systems*. URL: arxiv:0907.2796v1.

[58] Ghanem and E Koch. *Analytic Continuation of Quantum Monte Carlo Data*. URL: https://www.cond-mat.de/events/correl18/talks/.

[59] Mark Jarrell. *The Maximum Entropy Method: Analytic Continuation of QMC Data*. URL: www.cond-mat.de/events/correl12/manuscripts/jarrell.

[60] A. S. Mishchenko. *Stochastic optimization method for analytic continuation*. URL: https://www.cond-mat.de/events/correl12/manuscripts/mishchenko.

[61] Chetan Nayak. *Many-Body Physics, Jan. 1999*. URL: inis.jinr.ru/sl/vol2/Physics/QuantumMechanics/Nayak,_Many-Body_Physics(lectures),1999.pdf.

VITA

Lucretius Coleman

Education

2022 – Ph.D. in physics at the University of Mississippi

2007 – B.Sc. in physics at the University of Mississippi

Research

2017 - 2022 – Computational condensed matter; research involves the use of quantum fluctuations in a Heisenberg spin chain to solve an analytical continuation problem in many-body physics.

Academic Employment

2014 - 2022 – Teaching assistant, Engineering physics lab, grading, and other duties, Dept. of Physics and Astronomy, University of Mississippi.